Development of a high-pressure xenon gas time projection chamber and evaluation of its performance at around the Q value of ^{136}Xe double-beta decay

Department of Physics, Graduate School of Science,
Kyoto University

Masashi Yoshida

February 6, 2024

Abstract

It is known that neutrinos have small masses, unlike the assumption in the standard model of elementary particle physics. If neutrinos have the Majorana mass terms, the small neutrino mass may be naturally explained. The Majorana nature of neutrino is also a key to understanding the matter-antimatter asymmetry in the universe. The observation of neutrinoless double-beta decay ($0\nu\beta\beta$) will be the evidence for the Majorana nature of the neutrino. The current most stringent limit is the one obtained with ^{136}Xe. The lower limit on the half-life of ^{136}Xe $0\nu\beta\beta$ is 2.3×10^{26} years.

A Xenon ElectroLuminescence detector (AXEL) is a detector under development to search for $0\nu\beta\beta$ with ^{136}Xe. The AXEL detector is a high-pressure xenon gas time projection chamber with a unique readout system for ionization signals called the electroluminescence light collection cell (ELCC). ELCC allows the AXEL detector to achieve good energy resolution and three-dimensional track reconstruction, which are important features to conduct a highly sensitive $0\nu\beta\beta$ search. A demonstration at the energy around the Q value of ^{136}Xe $0\nu\beta\beta$, 2458 keV is a critical step to realize a high sensitivity $0\nu\beta\beta$ search with the AXEL detector. For this purpose, a prototype detector with a vessel of 180 L has been developed.

The drift field cage generates the electric field to drift the ionization electrons toward the ELCC. The requirement for the drift electric field was studied in terms of the energy resolution and track reconstruction ability. Then, the field cage for the 180 L prototype detector was constructed and commissioned.

To evaluate the performance of the 180 L prototype detector, the measurement was conducted with gamma-ray sources, ^{88}Y and thorium series. A clear peak of 2615 keV, from ^{208}Tl gamma rays, was observed in the acquired energy spectrum. The energy resolution was evaluated with other peaks in the energy spectrum. The obtained FWHM energy resolution is (0.73 ± 0.11) % at 1836 keV, which corresponds to the FWHM energy resolution of (0.60 ± 0.03) % or (0.70 ± 0.21) % at the Q value.

The reconstructed track images were also evaluated. The dense energy deposits at the end of the track were observed, corresponding to the number of electrons in the events. This is a clear feature that can be used to discriminate between the $0\nu\beta\beta$ signal and the gamma-ray backgrounds. The diffusion constants were derived from the data. This is an important input for simulated track images, which is the basis of the development of signal background discrimination algorithms.

Possible sources that affect the energy resolution were investigated exhaustively, and the measured energy resolution was fully explained successfully. Improvement of the energy resolution by further development of the detector components is discussed based on the breakdown of the energy resolution. The sensitivity of the future AXEL detector is also discussed.

Acknowledgment

I extend my sincere gratitude to the individuals who supported and guided the completion of this doctoral thesis.

First and foremost, I express my deepest appreciation to Prof. Atsuko Ichikawa, my primary supervisor, for her guidance over the past nine years. Her uncompromising attitude to experiments has taught me deeply. I am truly grateful for her mentorship, which has shaped my fundamental way of confronting research.

I am also thankful to Prof. Tsuyoshi Nakaya for his guidance in thesis writing and document preparation. Also during daily chats, his inclusive perspective, extending beyond individual experiments to encompass the broader scope of high-energy physics, has broadened my understanding.

My sincere thanks go to Prof. Kiseki Nakamura, whose collaboration in experimental work provided a pragmatic experience. I have been greatly helped by his meticulous consideration of various aspects of our work, which has significantly contributed to the quality of our research.

I express my gratitude to Dr. Shuhei Obara, Dr. Sei Ban, and Dr. Kazuhiro Nakamura, my seniors and a peer during the AXEL experiment. The stable operation of the 180 L prototype detector stands on their legacy and expertise.

The initiation of the AXEL experiment was made possible by the pioneering research by Mr. Shinichi Akiyama. I am particularly grateful for him to take over my research on the Cockcroft-Walton voltage multiplier.

I extend my appreciation to Mr. Bungo Sugashima, Mr. Yukimasa Kashino, Mr. Hibiki Shinagawa, Mr. Junya Hikida, and Mr. Soki Urano, my juniors during the AXEL experiment. Their assistance in conducting experiments and valuable insights during daily meetings are crucial to the success of the project. Special mention goes to Mr. B. Sugashima, who uncovered bugs in our analyses, leading to significant improvements in the results.

To all the other AXEL collaborators, I express my gratitude for their support throughout the experiment.

I would like to thank Ms. Harumi Sekiguchi, Ms. Mana Sasaki, and Ms. Chiharu Tsuzuki for their invaluable support in secretary work.

I extend my general appreciation to the members of the High Energy Physics Laboratory for their contribution to the research environment. Especially, I thank Mr. Yuya Mino, Mr. Masaki Kawaue, and Mr. Hironobu Nakata. Daily chats with them during coffee breaks or dinners, which sometimes include physics topics, are healing for my mind.

Finally, I thank my parents, Takashi and Hiroko, for their support in my life during the long-term of doctoral course.

Masashi Yoshida
Kyoto, Japan
2024, February

Contents

1

Introduction

The existence of the neutrino mass is a well-established fact beyond the standard model of elementary particle physics. The smallness of the neutrino mass motivates the existence of a mass-acquisition mechanism different from that of other fermions, which is called the Majorana mass. The observation of the neutrinoless double-beta decay will be the direct evidence of the Majorana mass of neutrinos. This thesis focuses on the development of a high-pressure xenon gas time projection chamber to search for neutrinoless double-beta decay of ^{136}Xe and evaluation of its performance. In this chapter, the theoretical background on neutrinoless double beta decay and examples of experiments to search for neutrinoless double beta decay are described.

1.1 Neutrino in the Standard Model

The standard model of elementary particle physics (SM) is a field theory including fields corresponding to all known elementary particles with Lorentz invariance and local gauge symmetry of $SU(3)\times SU(2)\times U(1)$. The SM successfully describes almost all phenomena regarding elementary particles under the achievable energy: The three (electromagnetic, weak, strong) interactions between the fermions (quarks, leptons) and the existence of gause bosons are described by the gauge symmetries, and the masses of the fermions and gauge bosons are explained by the spontaneous symmetry breaking of the Higgs field (Higgs mechanism). All of the particles included in the SM is already discovered. However, there are some phenomena that cannot be explained in the scope of the SM, for example, the existence of the dark matter and the quantization of the charge. Hence it is considered that there is a yet unknown high-energy theory that embraces the SM. The mass of neutrino is one of the most well-established phenomena beyond the SM. Neutrino can be considered to be the key to understanding the physics beyond the SM.

Neutrino is introduced in the SM as a massless neutral left-handed weyl fermion forming an

$SU(2)$ doublet with a left-handed charged lepton. Corresponding to the three generations of the charged lepton (electron, muon, and tauon), there are three flavors of neutrino (electron neutrino, muon neutrino, and tau neutrino).

The first detection of neutrino was done by F. Reines and C. L. Cowan in 1956 [1], in which electron anti-neutrinos from a nuclear reactor were observed. Subsequently, L. M. Lederman, M. Schwartz, and J. Steinberger detected muon neutrinos from pion decays in 1962 [2], establishing the existence of different flavors of neutrino. Tau neutrino was discovered by the DONUT experiment in 2000 [3]. The number of flavors of neutrino lighter than half of the Z boson mass has been measured to be 2.9840 ± 0.0082 from the decay width of Z boson by collider experiments [4].

1.2 Mass of the neutrino

Though neutrino is massless in the SM, the discovery of neutrino oscillation [5] revealed that neutrinos have masses actually. Neutrino oscillation is a phenomenon in which neutrinos change their flavor during flight. It happens only when neutrinos have masses. Neutrino oscillations among three flavors have been established by experiments using various neutrino sources such as atmospheric, solar, reactors, and accelerators.

1.2.1 Neutrino oscillation

Neutrino oscillation is theoretically described as follows. The flavor eigenstate of a neutrino $|\nu_l\rangle$ $(l = e, \mu, \tau)$ is expressed as a linear superposition of three mass eigenstates $|\nu_i\rangle\rangle$ $(i = 1, 2, 3)$ as

$$|\nu_l\rangle = \sum_i U_{li} \, |\nu_i\rangle \ . \tag{1.1}$$

Here, U is a 3×3 unitary mixing matrix called the Pontecorvo-Maki-Nakagawa-Sakata (PMNS) matrix. It can be parametrized as

$$\begin{aligned} U &= \begin{pmatrix} U_{e1} & U_{e2} & U_{e3} \\ U_{\mu1} & U_{\mu2} & U_{\mu3} \\ U_{\tau1} & U_{\tau2} & U_{\tau3} \end{pmatrix} \\ &= \begin{pmatrix} 1 & 0 & 0 \\ 0 & c_{23} & s_{23} \\ 0 & -s_{23} & c_{23} \end{pmatrix} \begin{pmatrix} c_{13} & 0 & s_{13}e^{-i\delta} \\ 0 & 1 & 0 \\ -s_{13}e^{i\delta} & 0 & c_{13} \end{pmatrix} \begin{pmatrix} c_{12} & s_{12} & 0 \\ -s_{12} & c_{12} & 0 \\ 0 & 0 & 1 \end{pmatrix} , \end{aligned} \tag{1.2}$$

where $s_{ij} = \sin\theta_{ij}$, $c_{ij} = \cos\theta_{ij}$, θ_{ij} are mixing angles, and δ is a CP violating phase called the Dirac CP phase. Considering the time evolution of the mass eigenstate with an energy E as

$$|\nu_i(t)\rangle = e^{-iEt} \, |\nu_i\rangle \ , \tag{1.3}$$

Table1.1: Summary of the current best-fit values of the neutrino oscillation parameters [6, 7].

Parameter	Mass Ordering	Best-fit$\pm 1\sigma$
$\sin^2\theta_{12}$	NO	$0.303^{+0.012}_{-0.012}$
	IO	$0.303^{+0.012}_{-0.011}$
$\sin^2\theta_{23}$	NO	$0.451^{+0.019}_{-0.016}$
	IO	$0.569^{+0.016}_{-0.021}$
$\sin^2\theta_{13}$	NO	$0.02225^{+0.00056}_{-0.00059}$
	IO	$0.02223^{+0.00058}_{-0.00058}$
Δm^2_{21}	–	$7.41^{+0.21}_{-0.20} \times 10^{-5}$ eV^2
Δm^2_{31}	NO	$+2.507^{+0.026}_{-0.027} \times 10^{-3}$ eV^2
Δm^2_{32}	IO	$-2.486^{+0.025}_{-0.028} \times 10^{-3}$ eV^2
δ	NO	$232^\circ{}^{+36^\circ}_{-26^\circ}$
	IO	$276^\circ{}^{+22^\circ}_{-29^\circ}$

the probability of neutrino oscillation from $|\nu_l\rangle$ to $|\nu_{l'}\rangle$ in vacuum with a relativistic energy E and a propagation distance L is calculated as

$$P(\nu_l \to \nu_{l'}) \simeq \delta_{ll'} - 4\sum_{i>j} \mathrm{Re}\left(U^*_{li}U_{l'i}U_{lj}U^*_{l'j}\right)\sin^2\left(\frac{\Delta m^2_{ij}L}{4E}\right) + 2\sum_{i>j} \mathrm{Im}\left(U^*_{li}U_{l'i}U_{lj}U^*_{l'j}\right)\sin^2\left(\frac{\Delta m^2_{ij}L}{2E}\right) , \tag{1.4}$$

where

$$\delta_{ll'} = \begin{cases} 1 & (l = l') \\ 0 & (l \neq l') \end{cases} , \tag{1.5}$$

is Kronecker's delta, $\Delta m^2_{ij} = {m_i}^2 - {m_j}^2$ is a mass-squared difference, and m_i is the mass eigenvalue of $|\nu_i\rangle$. Therefore neutrino oscillation occurs only if neutrinos have tiny masses and the masses are different between the mass eigenstates. Measurement of neutrino oscillations derives θ_{ij} and $|\Delta m^2_{ij}|$.

Currently, there remain two possibilities for mass ordering; $m_1 < m_2 < m_3$ which is called Normal Ordering (NO), and $m_3 < m_1 < m_2$ which is called Inverted Ordering (IO).

Table 1.1 summarizes the current best-fit values of the neutrino oscillation parameters obtained from the global fit [6, 7] of the data of existing neutrino oscillation experiments. The mixing angles and mass-squared differences are precisely measured, while the Dirac CP phase has yet large uncertainty.

1.2.2 Mass ordering

The mass ordering of the neutrinos, NO or IO, is one of the open questions about neutrino mass. Since the absolute mass scale of the neutrinos is different depending on the mass ordering, it is an important input to the search for neutrinoless double-beta decay (Sec. 1.4). Equation 1.4 is the oscillation probability in vacuum and is not sensitive to the sign of Δm^2_{ij}. Through the matter effect, however, neutrino oscillation experiments have sensitivity to the sign of Δm^2_{ij}, or the mass ordering. This is because electron neutrinos feel different potential than the muon and tau neutrinos do in dense matter, and the oscillation probabilities change differently depending on the mass ordering.

The Super-Kamiokande experiment favors the NO [8] with a significance of 93 % confidence level. The T2K accelerator experiment disfavors the IO at more than 1σ for all values of the Dirac CP phase [9]. Considered in conjunction with the cosmological observations that begin to reject the IO phase space (Sec. 1.2.3), the possibility of the NO is becoming more likely. It is expected to be determined with a sensitivity of higher than 3σ after 5 years of observation by Hyper Kamiokande [10]. The JUNO experiment is also expected to resolve the mass ordering at more than 3σ with 6 years of data taking [11].

1.2.3 Constraint on the absolute neutrino mass scale

Since neutrino oscillation experiments are only sensitive to the mass-squared difference, the absolute mass scale of neutrino is yet unknown. There are several ways to constrain the absolute neutrino mass scale. Of those, cosmological observation and direct mass measurement with beta decay are described here.

Constraint from cosmological observation

The mass of neutrinos affects the power spectrum of the cosmic microwave background (CMB), because neutrinos diffuse the density fluctuation of the universe, and the degree of the diffusion depends on the total neutrino mass. The total neutrino mass is constrained to be

$$\sum_i m_i < 0.26\,\mathrm{eV}\ , \tag{1.6}$$

at 95 % confidence level from the measurement of the CMB power spectrum by Planck [12]. A more stringent limit is achieved by combining other data of cosmological survey [13] as

$$\sum_i m_i < 0.082\,\mathrm{eV}\ , \tag{1.7}$$

at 95 % confidence level, though this result depends on the cosmological model. Note that $\sum_i m_i$ is greater than 0.06 eV (0.1 eV) for the NO (IO) considering the oscillation parameters. Therefore the result of cosmological observations begins to reject the IO. The next generation CMB observatories, for example, Simons Observatory, are expected to detect the non-zero total neutrino mass with more than 3.5σ (5.9σ) sensitivity for the case of the NO (IO) [14].

Constraint from direct mass measurement with beta decay

The direct mass measurement is based on the kinematics of beta decay:

$$n \to p + e^- + \bar{\nu}_e \ . \tag{1.8}$$

The higher edge of the beta ray energy spectrum is lowered from the Q value of the beta decay by the effective electron neutrino mass defined as

$$m_{\nu_e}^{\text{eff}} = \sqrt{\sum_i m_i^2 \left|U_{ei}\right|^2} \ . \tag{1.9}$$

There is yet no indication of $m_{\nu_e}^{\text{eff}} \neq 0$, and the most stringent upper limit on $m_{\nu_e}^{\text{eff}}$ is from the KATRIN experiment observing tritium beta decay as

$$m_{\nu_e}^{\text{eff}} < 0.8\,\text{eV} \tag{1.10}$$

at 90 % confidence level [15]. This result roughly corresponds to the constraint on the lightest neutrino mass, $m_{\text{lightest}} < 0.8\,\text{eV}$, which is much less stringent compared to the cosmological constraint. The constraint from the search for the neutrinoless double-beta decay described in Sec. 1.4 is also more sensitive to the lightest neutrino mass than direct mass measurement, assuming the Majorana nature of neutrinos. However, direct mass measurement is the model-independent measurement on the absolute neutrino mass scale and is therefore important.

1.3 Majorana mass

As seen above, the masses of neutrinos are constrained to be at most $\lesssim 1\,\text{eV}$. This is quite lighter than the other fermions in the SM; $\sim 10^{-6}$ lighter than the electron (511 keV), the lightest charged fermion in the SM, for example. This discrepancy is unnatural if the origin of the neutrino mass and that of the other fermions are the same, and it motivates one to consider the special origin of mass for neutrinos.

The mass of the fermion in the SM is generated from the Yukawa coupling to the Higgs field. For example, in the case of charged leptons, it is

$$-\mathcal{L}_{\text{Yukawa}} = y_l \overline{L_{lL}} \phi e_{lR} + h.c. \ (l = e, \mu, \tau), \tag{1.11}$$

where y_l is the Yukawa coupling constant, $L_{lL} = \begin{pmatrix} \nu_{lL} \\ e_{lL} \end{pmatrix}$ is the $SU(2)$ doublet of the left-handed leptons, e_{lR} is the right-handed charged leptons, ϕ is the Higgs field, $SU(2)$ doublet complex scalar field, and $h.c.$ refers to the Hermitian conjugate. The ϕ has a potential of

$$V(\phi) = -m_\phi^2 \phi^\dagger \phi + \lambda \left(\phi^\dagger \phi\right)^2 \ , \tag{1.12}$$

where m_ϕ and λ are real positive coefficients. Then, as a result of a spontaneous symmetry breaking, ϕ has the vacuum expectation value:

$$\langle \phi \rangle = \begin{pmatrix} 0 \\ \frac{v}{\sqrt{2}} \end{pmatrix} \ , \tag{1.13}$$

where $v = m_\phi / \sqrt{\lambda}$. Equation 1.11 turns to

$$-\mathcal{L}_{\text{Yukawa}} = \frac{y_l v}{\sqrt{2}} \left(\overline{e_{lL}} e_{lR} + \overline{e_{lR}} e_{lL}\right) \tag{1.14}$$

This is the mass term, and the fermion gets a mass of $y_l v / \sqrt{2}$. This mechanism is called the Higgs mechanism.

A simple way to give masses to neutrinos is to introduce three right-handed neutrinos ν_{lR} and add the following terms to the Lagrangian:

$$-\mathcal{L}_{\nu,\text{Yukawa}} = y_{\nu_l} \overline{L_{lL}} \tilde{\phi} \nu_{lR} + h.c. \ , \tag{1.15}$$

where $\tilde{\phi} = \begin{pmatrix} 0 & 1 \\ -1 & 0 \end{pmatrix} \phi^*$. Then the mass term is acquired also by the Higgs mechanism. This is, however, assuming more than a 10^6 discrepancy of the Yukawa coupling between neutrinos and other fermions, and it is unnatural.

Since neutrinos are neutral, another type of mass term called the Majorana mass term is allowed. The Majorana mass term consists of only a left-handed or only a right-handed spinor. A closer look at the Majorana mass term is given below. Consider a four-component spinor Ψ. In case Ψ is neutral, it is allowed that the charge conjugate of Ψ is identical to Ψ itself:

$$\Psi^c = \Psi \ . \tag{1.16}$$

Equation 1.16 is called the Majorana condition. Under the chiral representation, the Majorana condition is

$$\Psi = \begin{pmatrix} \psi_L \\ \psi_R \end{pmatrix} = \begin{pmatrix} \psi_R^c \\ \psi_L^c \end{pmatrix} = \Psi^c \ , \tag{1.17}$$

where ψ_L and ψ_R is the left-handed and the right-handed component of Ψ. Hence Ψ can be expressed only by the left-handed or the right-handed component:

$$\Psi = \begin{pmatrix} \psi_L \\ \psi_L^c \end{pmatrix} = \begin{pmatrix} \psi_R^c \\ \psi_R \end{pmatrix} \ . \tag{1.18}$$

Then, the mass term of Ψ also consists of only the left-handed or the right-handed component:

$$-m\bar{\Psi}\Psi = -m\left(\overline{\psi_L}\psi_L^c + \overline{\psi_L^c}\psi_L\right) = -m\left(\overline{\psi_R}\psi_R^c + \overline{\psi_R^c}\psi_R\right) \ . \tag{1.19}$$

Such a mass term is called the Majorana mass term, and neutrinos may have the Majorana mass term.

Including the Majorana mass term, the general mass term for neutrinos is written as follows, introducing N right-handed neutrinos ν_{iR} $(i = 1, 2, \ldots, N)$:

$$-\mathcal{L}_{M_\nu} = M_{Dil}\overline{\nu_{iR}}\nu_{lL} + \frac{1}{2}M_{Nij}\overline{\nu_{iR}}\nu_{jR}^c + h.c. \tag{1.20}$$

$$= \frac{1}{2}(\overline{\nu_{lL}^c}, \overline{\nu_{iR}})\begin{pmatrix} O & \left[M_D^T\right]_{lj} \\ [M_D]_{l'i} & [M_N]_{ij} \end{pmatrix}\begin{pmatrix} \nu_{l'L} \\ \nu_{jR}^c \end{pmatrix} + h.c. \ , \tag{1.21}$$

where the first term of Eq. 1.20 is called the Dirac mass generated by Higgs mechanism from Eq. 1.15, and the second term is the Majorana mass of the right-handed neutrinos. Note that the Majorana mass of the left-handed neutrinos is prohibited by the $SU(2)$ invariance.

1.3.1 See-Saw mechanism

If the mass eigenvalue of M_N is large and $M_N^{-1}M_D$ is small, the mass matrix of Eq. 1.21, $\hat{M} = \begin{pmatrix} O & M_D^T \\ M_D & M_N \end{pmatrix}$ can be diagonalized as follows. First, $\hat{M}$ is block diagonalized:

$$U_1 = \begin{pmatrix} \mathbf{1}_3 & \left(M_N^{-1}M_D\right)^\dagger \\ -M_N^{-1}M_D & \mathbf{1}_N \end{pmatrix} \tag{1.22}$$

$$U_1^\dagger \hat{M} U_1 = \begin{pmatrix} M_\nu & O \\ O & M_N \end{pmatrix} , \tag{1.23}$$

where $M_\nu = -M_D^\dagger M_N^{-1} M_D$. Next, M_ν and M_N are diagonalized.

$$U_\nu^\dagger M_\nu U_\nu = \mathrm{diag}\,(m_1, m_2, m_3) \tag{1.24}$$

$$U_N^\dagger M_N U_N = \mathrm{diag}\,(m_4, m_5, \ldots, m_{3+N}) \tag{1.25}$$

$$U_2 = \begin{pmatrix} U_\nu & O \\ O & U_N \end{pmatrix} \tag{1.26}$$

$$U_2^\dagger U_1^\dagger \hat{M} U_1 U_2 = \mathrm{diag}\,(m_1, m_2, m_3, \ldots, m_{3+N}) \ . \tag{1.27}$$

The relation between the flavor state and mass state $\begin{pmatrix} \nu_i \\ N_I^c \end{pmatrix}(i = 1, 2, 3)$ $(I = 4, 5, \ldots, 3+N)$ is

$$\begin{pmatrix} \nu_{lL} \\ \nu_{iR}^c \end{pmatrix} = U_1 U_2 \begin{pmatrix} \nu_i \\ N_I^c \end{pmatrix} = \begin{pmatrix} U_\nu & \left(M_N^{-1}M_D\right)^\dagger U_N \\ -M_N^{-1}M_D U_\nu & U_N \end{pmatrix}\begin{pmatrix} \nu_i \\ N_I^c \end{pmatrix} , \tag{1.28}$$

$$\text{especially, } \nu_{lL} = U_{\nu li}\nu_i + \left[\left(M_N^{-1}M_D\right)^\dagger U_N\right]_{lI} N_I^c \ . \tag{1.29}$$

Since the contribution of N_I^c is suppressed by small $M_N^{-1}M_D$, ν_{lL} is almost a linear superposition of ν_i. Thus U_ν is the PMNS matrix (Eq. 1.2). However, it is extended by additional CP violating phases ϕ_1, ϕ_2 called the Majorana CP phase:

$$
\begin{aligned}
U &= \begin{pmatrix} U_{e1} & U_{e2} & U_{e3} \\ U_{\mu 1} & U_{\mu 2} & U_{\mu 3} \\ U_{\tau 1} & U_{\tau 2} & U_{\tau 3} \end{pmatrix} \\
&= \begin{pmatrix} 1 & 0 & 0 \\ 0 & c_{23} & s_{23} \\ 0 & -s_{23} & c_{23} \end{pmatrix} \begin{pmatrix} c_{13} & 0 & s_{13}e^{-i\delta} \\ 0 & 1 & 0 \\ -s_{13}e^{i\delta} & 0 & c_{13} \end{pmatrix} \begin{pmatrix} c_{12} & s_{12} & 0 \\ -s_{12} & c_{12} & 0 \\ 0 & 0 & 1 \end{pmatrix} \begin{pmatrix} 1 & & \\ & e^{i\frac{\phi_1}{2}} & \\ & & e^{i\frac{\phi_2}{2}} \end{pmatrix} . \quad (1.30)
\end{aligned}
$$

The suppression of M_ν by $M_N^{-1}M_D$ naturally explains the smallness of the mass eigenstates m_1, m_2, and m_3, even if the Dirac mass M_D is comparable to the mass of the other fermions. This mechanism is called the (Type-I) See-Saw mechanism.

More generally, one can consider that there is a new physics beyond the SM above the energy scale of $\Lambda_{\rm NP}$ and that the SM is a low-energy effective theory. In such a case, the Lagrangian of the effective theory can contain non-renormalizable terms suppressed by $\Lambda_{\rm NP}$. Using only the field contained in the SM and respecting gauge symmetry, the following dimension-5 operator can be constructed:

$$
\mathcal{O}_5 = \frac{f_{ll'}}{\Lambda_{\rm NP}} \left(\overline{L_{lL}}\tilde{\phi}\right)\left(\tilde{\phi}^T L^c_{l'L}\right) + h.c. \ , \quad (1.31)
$$

where $f_{ll'}$ is a coupling constant. After the spontaneous symmetry breaking of $\tilde{\phi}$, Eq. 1.31 generates the effective Majorana mass term of the left-handed neutrinos:

$$
-\mathcal{L}_{M_\nu} = \frac{f_{ll'}}{2}\frac{v^2}{\Lambda_{\rm NP}}\overline{\nu_{lL}}\nu^c_{l'L} + h.c. \ . \quad (1.32)
$$

The Majorana mass is $f_{ll'}v^2/\Lambda_{\rm NP}$ and suppressed by $v/\Lambda_{\rm NP}$. This is the general form of the See-Saw mechanism, and the Type-I See-Saw is a special case of this.

1.3.2 Leptogenesis

It is considered that in the early universe, a small asymmetry between baryons and anti-baryons was created by some mechanism, which should have existed in equal numbers, and that only a part of the baryons remained through pair annihilation and formed the present universe.

The Majorana mass term of neutrinos violates the total lepton number by two units. Leptogenesis is a scenario in which the lepton number is generated via the Majorana nature of neutrinos in the early universe, and the generated lepton number L is converted to the baryon number B through the sphaleron process conserving $B - L$, resulting in the matter-antimatter asymmetry in the universe. Leptogenesis was first proposed by M. Fukugita and

Table1.2: Summary of the double-beta nuclei commonly used in experiments. The nutral abundances are from [18], and the Q values are from [19].

	natural abundance	Q value [keV]	half-life of $2\nu\beta\beta$
^{48}Ca	0.187 %	4268	$\left(6.4^{+0.7+1.2}_{-0.6-0.9}\right) \times 10^{19}$ [20]
^{76}Ge	7.44 %	2039	$(1.926 \pm 0.094) \times 10^{21}$ [21]
^{82}Se	8.73 %	2998	$(9.39 \pm 0.17 \pm 0.58) \times 10^{19}$ [22]
^{96}Zr	2.80 %	3356	$(2.35 \pm 0.14 \pm 0.16) \times 10^{19}$ [23]
^{100}Mo	9.63 %	3034	$(6.90 \pm 0.15 \pm 0.37) \times 10^{18}$ [24]
^{116}Cd	7.49 %	2813	$(2.74 \pm 0.04 \pm 0.18) \times 10^{19}$ [25]
^{130}Te	33.80 %	2528	$\left(7.71^{+0.08+0.12}_{-0.06-0.15}\right) \times 10^{20}$ [26]
^{136}Xe	8.9 %	2458	$(2.38 \pm 0.02 \pm 0.14) \times 10^{21}$ [27]
^{150}Nd	5.64 %	3371	$\left(9.34 \pm 0.22^{+0.62}_{-0.60}\right) \times 10^{18}$ [28]

T. Yanagida [16], and various variations exist today [17] since it can produce sufficient asymmetry to explain the amount of matter in the current universe. Since most of Leptogenesis models assume the Majorana nature of neutrinos, the confirmation of the Majorana nature is highly motivated.

1.4 Neutrinoless double-beta decay

Majorana neutrino is well motivated as described above. However, whether neutrinos have the Majorana mass term is not yet determined. The most plausible way considered so far to confirm the Majorana nature of neutrinos is to search for neutrinoless double-beta decay.

Double-beta decay is a phenomenon in which two beta decays simultaneously occur in a nucleus. It occurs in the nuclei in which single beta decay is prohibited by the mass difference or large spin difference with the daughter nuclei. Table 1.2 is the summary of the double-beta nuclei commonly used in experiments. In these nuclei, ^{136}Xe and ^{76}Ge are used particularly often because they have long half-lives of $2\nu\beta\beta$, which leads to less background in $0\nu\beta\beta$ searches, and also can be enriched. The definitions of $2\nu\beta\beta$ and $0\nu\beta\beta$ are as follows.

The neutrino emitting decay mode that occurs within the SM is called $2\nu\beta\beta$:

$$2n \rightarrow 2p + 2e + 2\bar{\nu}_e \ . \tag{1.33}$$

The Feynman diagram of $2\nu\beta\beta$ is shown in Fig. 1.1a.

If and only if neutrinos have the Majorana mass term, the decay mode without emitting neutrinos is allowed. This decay mode is called neutrinoless double-beta decay ($0\nu\beta\beta$):

$$2n \rightarrow 2p + 2e \ . \tag{1.34}$$

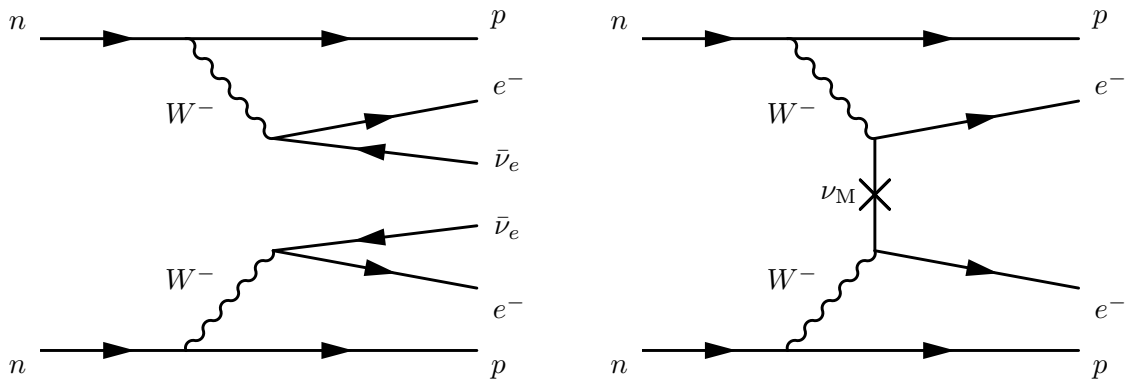

(a) $2\nu\beta\beta$ (b) $0\nu\beta\beta$

Figure1.1: Feynman diagrams of double-beta decays. (a) is for $2\nu\beta\beta$ and (b) is for $0\nu\beta\beta$.

Two neutrinos imaginary annihilate in the nucleus via the Majorana mass term, and hence no neutrino is emitted. The Feynman diagram of $0\nu\beta\beta$ is shown in Fig. 1.1b.

When one observes the double-beta decay, only two electrons can be observed in both $2\nu\beta\beta$ and $0\nu\beta\beta$ since the cross section of the neutrinos is extremely small. Thus the two are distinguished only by their energies. Figure 1.2 shows the schematic spectrum of the sum of the kinetic energies of two electrons emitted in double-beta decays. The $2\nu\beta\beta$ spectrum is continuous below the Q value of the double-beta decay because neutrinos carry away some kinetic energies. On the other hand, the $0\nu\beta\beta$ spectrum is a monochromatic peak at the Q value, though it is broadened by the finite energy resolution of a detector. Therefore good energy resolution is essential to distinguish these two decay modes.

The half-life of $0\nu\beta\beta$ is, even if it happens, considerably longer than that of $2\nu\beta\beta$ due to the lightness of the neutrino Majorana mass. The half-life of $0\nu\beta\beta$ is derived to be

$$\left(T_{1/2}^{0\nu}\right)^{-1} = G^{0\nu}\left|M^{0\nu}\right|^2 m_{\beta\beta}^2 \ , \tag{1.35}$$

where $G^{0\nu}$ is the phase space factor calculated from the initial and final state of the decay, and $M^{0\nu}$ is the nuclear matrix element of $0\nu\beta\beta$. $m_{\beta\beta}$ is the effective Majorana mass of electron neutrino expressed using the PMNS matrix (Eq. 1.30) as

$$\begin{aligned} m_{\beta\beta} &= \left|\sum_i U_{ei}^2 m_i\right| \\ &= \left|\left(m_1 c_{12}^2 + m_2 s_{12}^2 e^{i\phi_1}\right) c_{13}^2 + m_3 s_{13}^2 e^{i(\phi_2 - 2\delta)}\right| \ . \end{aligned} \tag{1.36}$$

Thus the discovery of $0\nu\beta\beta$ not only is the direct evidence of the Majorana nature of neutrinos but also leads to the measurement of the absolute mass scale of neutrinos and the Majorana

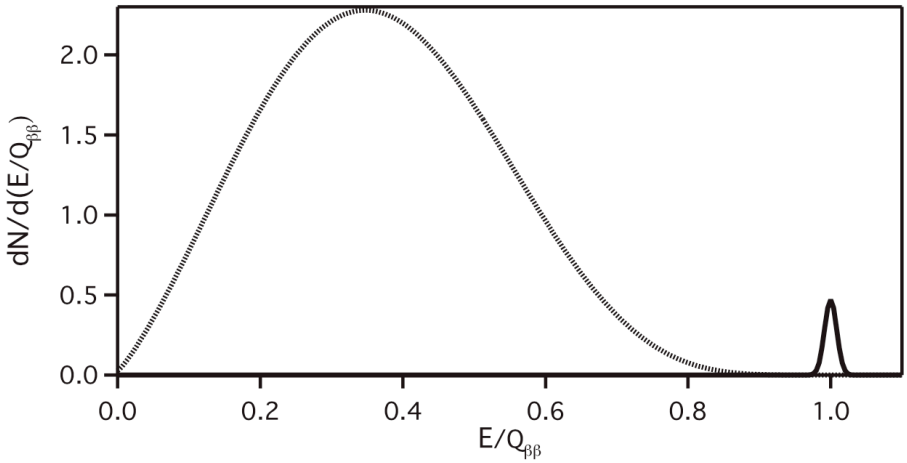

Figure1.2: Schematic spectrum of the sum of the energies of two electrons emitted in double-beta decay. $2\nu\beta\beta$ (dotted curve) and $0\nu\beta\beta$ (solid curve). Figure from [29].

CP phases. However, the nuclear matrix element $M^{0\nu}$ can currently be obtained only by numerical calculations based on nuclear models and has large model dependence by a factor of 2–3 [30]. Hence the translation from $T^{0\nu}_{1/2}$ to $m_{\beta\beta}$ has significant uncertainty. The current best limit on $m_{\beta\beta}$ is set by KamLAND-Zen using ^{136}Xe [31] (Fig. 1.3). The lower limit on the half-life is

$$T^{0\nu}_{1/2} > 2.3 \times 10^{26}\,\text{year} \tag{1.37}$$

at 90 % confidence level, and the coreesponding upper limit on $m_{\beta\beta}$ is

$$m_{\beta\beta} < (36 - 156)\ \text{meV}\ . \tag{1.38}$$

It should be noted that the half-life of 2.3×10^{26} years corresponds to one decay per year with 52 kg of ^{136}Xe. To lower the limit on $m_{\beta\beta}$ by factor 2, four times more target mass is required for a background-free case and 16 times more target mass for a background-dominated case.

1.5 Signal and background for $0\nu\beta\beta$ search

The most important feature of the signal in the $0\nu\beta\beta$ search is that the sum energy of the two beta rays is equal to the Q value, 2458 keV for ^{136}Xe. If the experiment can reconstruct charged particle tracks, two electron tracks emitted from one point are also a powerful feature to distinguish the signal from backgrounds.

In general, sources of the background events are $2\nu\beta\beta$ with energies close to the Q value, environmental radiation, and spallation products due to cosmic muons. The backgrounds induced by cosmic muons can be reduced by conducting experiments at underground facilities, i.e., shielding by rocks. Surrounding the detector with an active or passive shield is

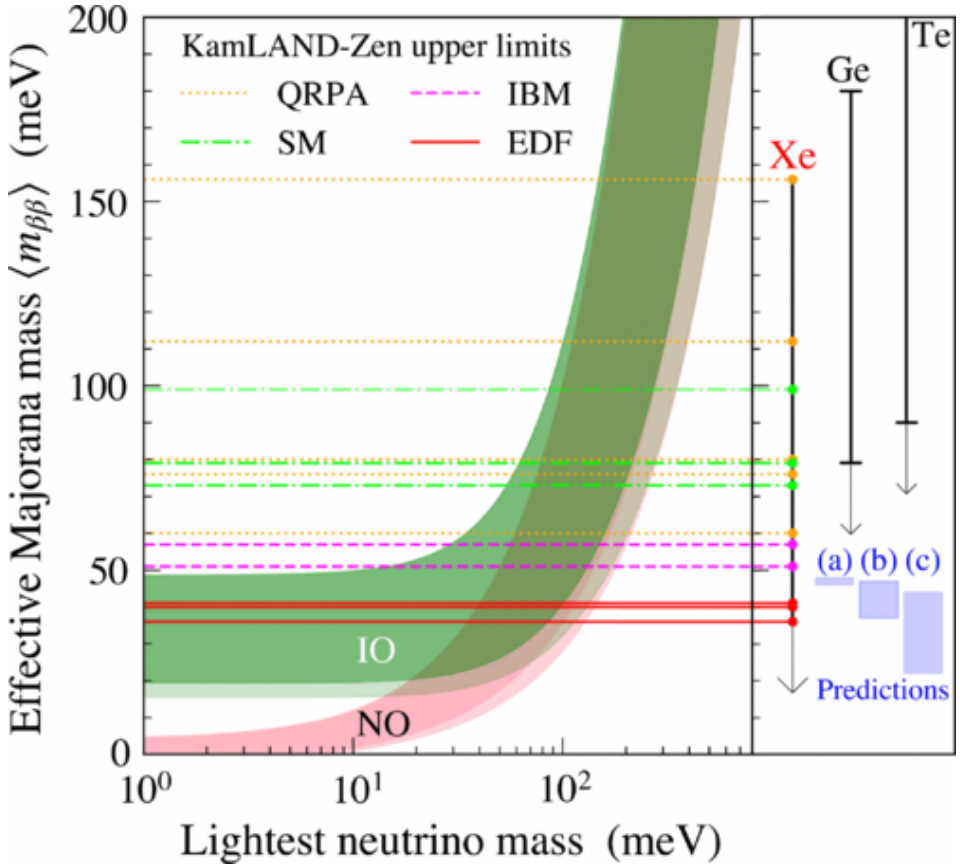

Figure1.3: $m_{\beta\beta}$ as a function of the lightest neutrino mass. The red (green) shaded area is the allowed region from the oscillation parameters in the case of the NO (IO). The horizontal lines show the upper limits on $m_{\beta\beta}$ obtained with the various nuclear matrix elements. The side panel show the best limits for ^{136}Xe, ^{76}Ge, and ^{130}Te, and theoretical predictions on $m_{\beta\beta}$ for IO. Figure from [31].

also effective. The background of environmental radiation is also suppressed by shields. It is also important to use materials with low radioactivity in the detector. The remaining backgrounds should be rejected by good energy resolution and additional separation by the detector. Tracking detectors can easily remove alpha rays and Compton scattering of gamma rays (Sec. 1.5.1).

In the following, the interaction of gamma rays, the major background source, is described, followed by a detailed description of the discrimination between signal and background events.

1.5.1 Interaction of gamma rays

In this energy region, gamma rays interact with matter by photoelectric absorption, Compton scattering, and electron-positron pair creation. Figure 1.4 shows the mass attenuation

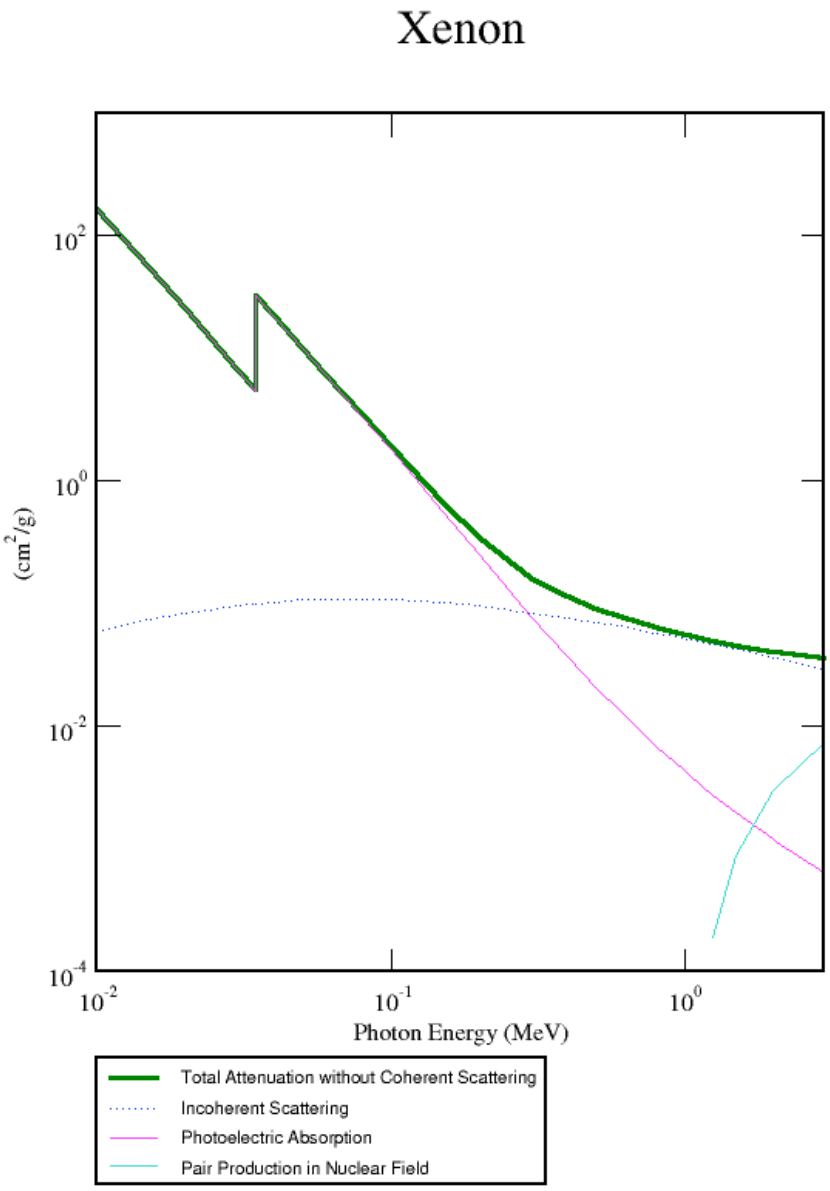

Figure1.4: Total mass attenuation length of gamma rays in xenon. Generated by [32]. Incoherent scattering refers to Compton scattering. $1\,\mathrm{cm}^2/\mathrm{g}$ corresponds to 220 barn.

length of gamma rays in xenon. At lower energies, photoelectric absorption is dominant. Above approximately 500 keV, Compton scattering becomes more frequent. Above a threshold of 1022 keV, electron-positron pair creation occurs.

Table1.3: Energies of characteristic X-rays of xenon [33]

	Energy
$K_{\alpha 1}$	29.78 keV
$K_{\alpha 2}$	29.46 keV
K_{β}	33.62 keV
$L_{\alpha 1}$	4.110 keV

Photoelectric absorption

In this process, a gamma ray is absorbed by an atom, and a single orbital electron is emitted as a photoelectron. The hole created in the orbital is eventually occupied by a higher orbital electron, and a characteristic X-ray or Auger electron is emitted with an energy equal to the difference in the binding energies. The sum of the energies of the photoelectron and X-ray/Auger electron is equal to that of the initial gamma ray. Table 1.3 lists the energies of characteristic X-rays of xenon. Since the energies of $K_{\alpha 1}$ and $K_{\alpha 2}$ are very close, hereafter they are referred to identically as K_{α}, with an energy of 29.68 keV, averaged with their branching ratio.

For a sufficiently large detector, the photoelectron and characteristic X-ray or Auger electron are fully contained in the detector and deposit their full energy. Thus photoelectric absorption events make a full energy peak in the measured energy spectrum.

The spatial pattern of a photoelectric absorption event is a single cluster track with a dense energy deposit at the endpoint. However, in case a K_{α} or K_{β} X-ray is emitted, another cluster may be formed at a short distance from the interaction point, ~ 3 cm for 8 bar of xenon gas. In the case of the emission of an L X-ray, it is usually too close to separate the clusters.

Compton scattering

This is a process in which a gamma ray interacts with the orbital electron, and both the photon and the electron are scattered off. The target electron can almost be regarded as a free electron, and therefore the relation of energies of the incident photon ($h\nu$) and the scattered photon ($h\nu'$) is given as

$$h\nu' = \frac{h\nu}{1 + \frac{h\nu}{m_e c^2}(1 - \cos\theta)} \ , \tag{1.39}$$

where θ is the scattered angle of the photon and $m_e c^2$ is the mass of an electron (511 keV). The scattered electron gets kinetic energy of $h\nu - h\nu'$.

If the scattered photon escapes from the detector, deposited energy is only $h\nu - h\nu'$. Thus, in the energy spectrum, these events make a continuum with the maximum energy of the case

$\theta = 180°$, which is called Compton edge. The spatial pattern of these events is single-clustered.

In case the emitted photon interacts in the detector again, the deposited energy exceeds the Compton edge, and the spatial pattern has multiple clusters. When the last scattered photon is absorbed in the detector via photoelectric absorption, the total deposited energy is the full energy of the initial gamma ray, and the event is contained in the full energy peak in the energy spectrum.

Electron-positron pair creation

In this process, a gamma-ray photon interacts with the electric field of a nucleus and converts to a pair of an electron and a positron.

The created electron and positron deposit their kinetic energy in the detector. After depositing its full kinetic energy, the stopped positron annihilates with one of the surrounding electrons and emits two gamma rays of 511 keV. In case the annihilation gamma rays escape from the detector, the deposited energy is only the kinetic energies of the electron and the positron, which is 1022 keV lower than the full energy of the initial gamma ray. Thus these events make a peak in the energy spectrum, which is called a double escape peak.

The spatial pattern of a pair creation event is a single cluster with two dense energy deposits at the endpoints corresponding to the stopped positions of an electron and a positron.

1.5.2 Signal-background discrimination

Environmental radiations that may be contaminated in the peak region of $0\nu\beta\beta$ of ^{136}Xe are the 2448 keV gamma rays from ^{214}Bi in the uranium series and 2615 keV gamma rays from ^{208}Tl in the thorium series. The difference between the Q value, 2458 keV, and the energy of the gamma rays from ^{214}Bi, 2448 keV, is only 0.4%. A 2615 keV gamma ray from ^{208}Tl can undergo a Compton scattering outside the sensitive volume, and the scattered gamma ray may enter the detector and interact. The energy can be arbitrary under the initial energy, 2615 keV. When the energy is close to the Q value, it becomes a background. Meanwhile, these gamma-ray backgrounds can be separated by their spatial pattern; $0\nu\beta\beta$ has one cluster with two dense endpoints, and these gamma rays have multiple clusters (Compton scattering or photoelectric absorption with a K X-ray) or single cluster but with only one dense endpoint (photoelectric absorption).

The energy of $2\nu\beta\beta$ events is lower than $0\nu\beta\beta$ events by the amount neutrinos carry away. Since neutrinos are not observable, it is impossible to distinguish $2\nu\beta\beta$ from $0\nu\beta\beta$ by information other than their energy. However, due to the finite energy resolution of the detector, $2\nu\beta\beta$ events cannot be completely separated from $0\nu\beta\beta$ events. According to [34], the fraction

F of the $2\nu\beta\beta$ counts in the peak region of $0\nu\beta\beta$ is approximated to be

$$F = \frac{a\left(\delta_E\right) Q {\delta_E}^6}{m_{\mathrm{e}}} \ , \tag{1.40}$$

where δ_E is the FWHM energy resolution expressed as a fraction to the Q value and m_{e} is the electron mass. The coefficient $a\left(\delta_E\right)$ is moderately dependent on the energy resolution, and it is 8.5 for the case of $\delta_E = 1\,\%$. Thus, considering the ^{136}Xe $2\nu\beta\beta$ half-life of 2.38×10^{21} years, the energy resolution better than 3 % (2 %) suppresses the $2\nu\beta\beta$ contamination to less than 1/100 of the $0\nu\beta\beta$ signal for a half-life of 10×10^{27} (10×10^{28}) years of $0\nu\beta\beta$.

In summary, high energy resolution and detection of event patterns are essential for signal-background discrimination. It is also important to reduce the number of background events before the discrimination by shielding and lowering the radiation of the detector components.

1.6 Experiments searching for $0\nu\beta\beta$

The following conditions are required to conduct a sensitive search for $0\nu\beta\beta$.

- Large amount of double-beta decay nuclei
- Good energy resolution
- Low background environment and/or background rejection capability

Hereafter, the experiments that set the most stringent limit on the $0\nu\beta\beta$ half-life of ^{136}Xe and ^{76}Ge are summarized.

KamLAND-Zen [31]

The KamLAND-Zen experiment is an experiment using a liquid scintillator as a detector medium. The xenon-loaded liquid scintillator is contained in the inner balloon surrounded by 1 kiloton of liquid scintillator contained in the outer balloon. The detector is located in Kamioka mine in Japan, under 2700 meter water equivalent (m.w.e.) rock, to reduce background events induced by cosmic muons. With a thorough survey of the detector material and purification of the liquid scintillator, they have achieved extremely low radioactive impurities.

As the first phase (referred to as KamLAND-Zen 400), they used 380 kg of 91 % enriched ^{136}Xe. In the second phase (referred to as KamLAND-Zen 800), they increased the mass of enriched xenon to 745 kg. The exposure reported so far is 504 kg year for KamLAND-Zen 400 [35] and 970 kg year for KamLAND-Zen 800. Combining the data of KamLAND-Zen 400 and KamLAND-Zen 800, they set a current most stringent limit as shown in Eqs. 1.37 and 1.38.

The largest background is $2\nu\beta\beta$ because of the moderate energy resolution of roughly 10 %

(FWHM) at the Q value (2458 keV). Xenon spallation products induced by cosmic muons are also major backgrounds. The successor experiment KamLAND2-Zen is planned, increasing xenon mass and improving the energy resolution. The light yield will be increased by 5 times by introducing high quantum efficiency photomultiplier tubes, a new liquid scintillator with high light intensity, and mirrors to efficiently collect the scintillation light.

GERDA [36]

The GERDA experiment used high-purity germanium both as a source and a detector. The germanium detector was surrounded by liquid argon which acts as a shield and cooling material. The experiment was located at Laboratori Nazionali del Gran Sasso in Italy, 3500 m.w.e.

They finally used 45.2 kg of germanium detector enriched in ^{76}Ge to 87 %. The total exposure is 127.2 kg year. The excellent energy resolution of 0.12 %–0.24 % (FWHM) at the Q value (2039 keV) allowed a background-free search, and the obtained lower limit on the half-life of ^{76}Ge $0\nu\beta\beta$ is

$$T^{0\nu}_{1/2}\left(^{76}\mathrm{Ge}\right) > 1.8 \times 10^{26}\,\mathrm{year} \tag{1.41}$$

at 90 % confidence level. This is the current best limit on ^{76}Ge. This corresponds to the upper limit on the $m_{\beta\beta}$ of

$$m_{\beta\beta} < (79 - 180)\ \mathrm{meV}\ . \tag{1.42}$$

The GERDA group and another germanium experiment, the Majorana Demonstrator experiment, have joined and started the LEGEND-200 experiment, planning to use 200 kg of germanium detectors to improve the sensitivity. The data taking of LEGEND-200 is ongoing, first with 142 kg of germanium detectors.

1.7 $0\nu\beta\beta$ search experiments using high-pressure xenon gas time projection chamber

A high-pressure xenon gas time projection chamber (TPC) is a detector that has the potential to achieve a highly sensitive search for $0\nu\beta\beta$ of ^{136}Xe. The principle of a high-pressure xenon gas TPC is as follows.

Charged particles, for example, beta-rays generated in $0\nu\beta\beta$ or other background events, deposit their energies by exciting and ionizing the xenon atoms along the tracks. Excited atoms emit the primary scintillation photons following the process of

$$\mathrm{Xe}^* + 2\mathrm{Xe} \rightarrow \mathrm{Xe}^*_2 + \mathrm{Xe} \tag{1.43}$$

$$\mathrm{Xe}^*_2 \rightarrow 2\mathrm{Xe} + \gamma\ , \tag{1.44}$$

where Xe^* represents the excited xenon atom, Xe_2^* represents the dimer, and γ represents the emitted scintillation photon. This emission happens in a timescale of several tens of nanoseconds [37]. The emitted primary scintillation has a wavelength of around 175 nm which is in the vacuum ultraviolet (VUV) region. A uniform electric field is applied in the TPC, and ionization electrons drift toward the anode plane with a constant drift velocity under the electric field. Its timescale is from microseconds to several hundreds of microseconds. At the anode, ionization electrons are detected by a two-dimensional detector. From the hit pattern in the two-dimensional detector and the drift time measured from the primary scintillation, the three-dimensional track is reconstructed.

For the detection of the ionization electrons, secondary scintillation emission by the electroluminescence process (EL process) can be utilized. The EL process is a phenomenon in which the ionization electrons are accelerated to excite but not ionize the surrounding xenon atoms under a strong electric field, and excited atoms emit secondary scintillation photons following Eqs. 1.43 and 1.44. Since the EL process is a proportional process, it has the advantage that the fluctuations in the number of emitted photons are smaller than the fluctuations in the number of electrons emitted in the avalanche amplification.

The high-pressure xenon gas TPC can simultaneously achieve the three conditions for a sensitive $0\nu\beta\beta$ search described in Sec. 1.6. First, ^{136}Xe can be enriched relatively easily by centrifugation. A large amount of decay nuclei is achieved by using ^{136}Xe enriched xenon gas at high pressure. Second, the intrinsic energy resolution of xenon gas is good. Under an electric field with sufficiently high intensity, the average energy W_i to make one ionization electron is $W_i = 22.1\,\mathrm{eV}$ [38]. With the Fano factor F of 0.13 [39], the fluctuation in the number of ionization electrons is

$$\frac{\Delta N}{N} = 2.36\sqrt{\frac{F}{N}} = 2.36\sqrt{\frac{FW_i}{E}}\ , \tag{1.45}$$

where N is the number of ionization electrons, ΔN is its fluctuation, and E is the energy of the event. Thus the intrinsic FWHM energy resolution at the Q value of ^{136}Xe $0\nu\beta\beta$, 2458 keV, is 0.26 %. The detection of ionization electrons by the EL process can keep the good energy resolution. Lastly, the background events can be rejected by spatial pattern recognition of the reconstructed three-dimensional track of the event as described in Sec. 1.5.2.

Thus, high-pressure xenon gas TPC is advantageous in $0\nu\beta\beta$ search and is being developed by multiple groups.

NEXT

The NEXT experiment is the pioneer of $0\nu\beta\beta$ search using high-pressure xenon gas TPC with the EL process. A schematic view of the NEXT detector is shown in Fig. 1.5. Ionization

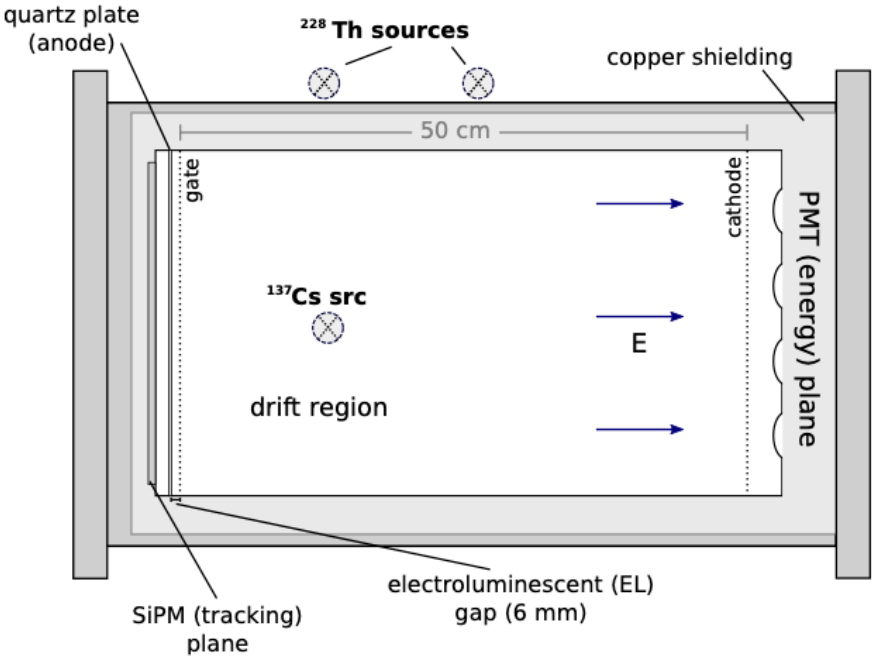

Figure1.5: Schematic view of the principle of the NEXT detector. High voltages are applied to the cathode and the gate mesh electrode. Ionization electrons undergo the EL process at the electroluminescent gap. Figure from [40]

electrons undergo the EL process at the gap between the gate mesh electrode and the anode quartz plate coated by indium tin oxide. Both the primary scintillation and EL photons are detected by the photomultiplier tube (PMT) array at the end of the cathode side to measure the deposited energy. EL photons are also detected by the dense array of silicon photomultipliers (SiPMs) at the end of the anode side to acquire the track pattern.

The 5-kg scale demonstration detector, NEXT-White, is currently under operation at Canfranc Underground Laboratory in Spain. They achieved the FWHM energy resolution of $(0.92 \pm 0.06)\,\%$ at the Q value [40]. They developed the background rejection method using a deep neural network and applied it to the real NEXT-White data, showing that the background is reduced to $10\,\%$ while maintaining the signal efficiency of $65\,\%$ [41].

The 100-kg scale successor detector, NEXT-100, is now under construction. A future ton-scale detector is planned, and its sensitivity to the half-life is expected to be 1.4×10^{27} years at $90\,\%$ confidence level after 5 years of operation [42].

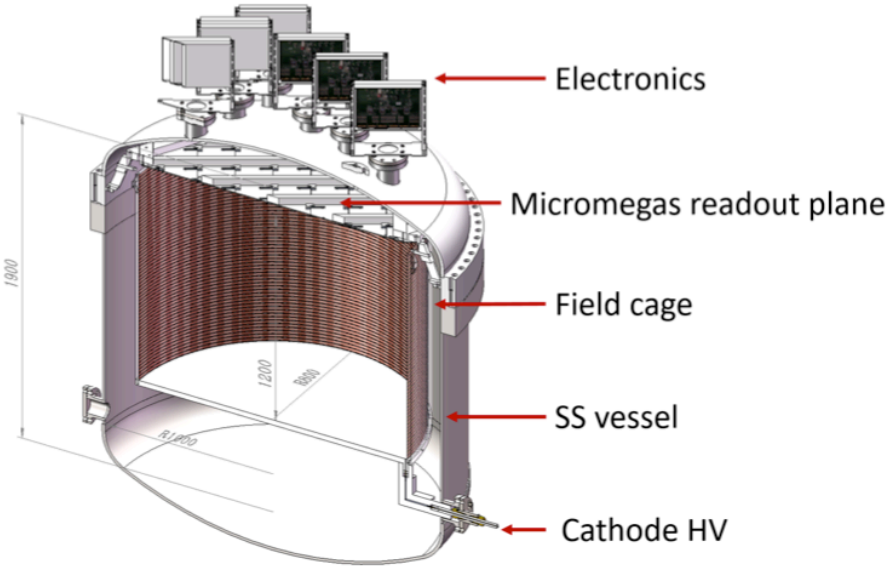

Figure1.6: Overview of the PandaX-III detector. Figure from [43].

PandaX-III

The Panda-X III experiment also adopts a high-pressure xenon gas TPC to search for $0\nu\beta\beta$. The overview of the Panda-X III detector is shown in Fig. 1.6. They use a gas mixture of xenon and 1 % trimethylamine (TMA). Although the admixture of TMA eliminates scintillation light emission, it suppresses the diffusion of ionization electrons during the drift, leading to the precise reconstruction of the track pattern. They adopt Micromegas, a kind of micropattern gas detector, to detect ionization signals with avalanche amplification. They showed an energy resolution of 14 % (FWHM) at 60 keV with the prototype detector [44]. The expected energy resolution at the Q value is 3 % (FWHM).

The detector holding 140 kg of xenon gas is currently under construction. They have develped a background rejection method based on the Kalman filter. It is expected to suppress backgrounds by a factor of 8.3×10^{-4} while keeping 50 % signal efficiency [45]. Based on this background rejection method, the sensitivity of the 140-kg detector on the half-life is expected to be 2.7×10^{26} years at 90 % confidence level after 5 years of live time [44].

AXEL

The AXEL detector is also a high-pressure xenon gas TPC using the EL process to search for $0\nu\beta\beta$. The AXEL detector has a unique cellular readout system for ionization electrons called

the electroluminescence light collection cell (ELCC). ELCC has extendability to a larger size while maintaining good energy resolution. The detail of the AXEL experiment is described in Chap. 2.

1.8 Outline of this thesis

The purpose of this thesis is to describe the development of the AXEL detector, focusing on the field shaping electrode, establishment of an analysis method to achieve good energy resolution, and evaluation and understanding of its performance at around the Q value of ^{136}Xe $0\nu\beta\beta$. The overview of the AXEL experiment is summarized in Chapter 2. The design, construction, and commissioning of the field shaping electrode, the field cage, are described in Chapter 3. The operation procedure of the prototype detector and the measurement with gamma-ray sources are described in Chapter 4. The analysis method is described in Chapter 5. Based on the result of the analysis, the detector performance is evaluated in Chapter 6. The results of the performance evaluation are discussed in Chapter 7. Future sensitivity is also discussed in this chapter. Finally, this thesis is summarized in Chapter 8.

2

AXEL experiment

AXEL (A Xenon ElectroLuminescence detector) is a project to search for $0\nu\beta\beta$ of ^{136}Xe using a high-presure xenon gas time projection chamber (TPC). The project is currently in the R&D phase. In this chapter, an overview of the AXEL project is described.

2.1 Overview of the detector

Figure 2.1 shows the schematic view of the AXEL detector. Xenon gas pressurized up to 10 bar and detector components are contained in a cylindrical vessel. High energy charged

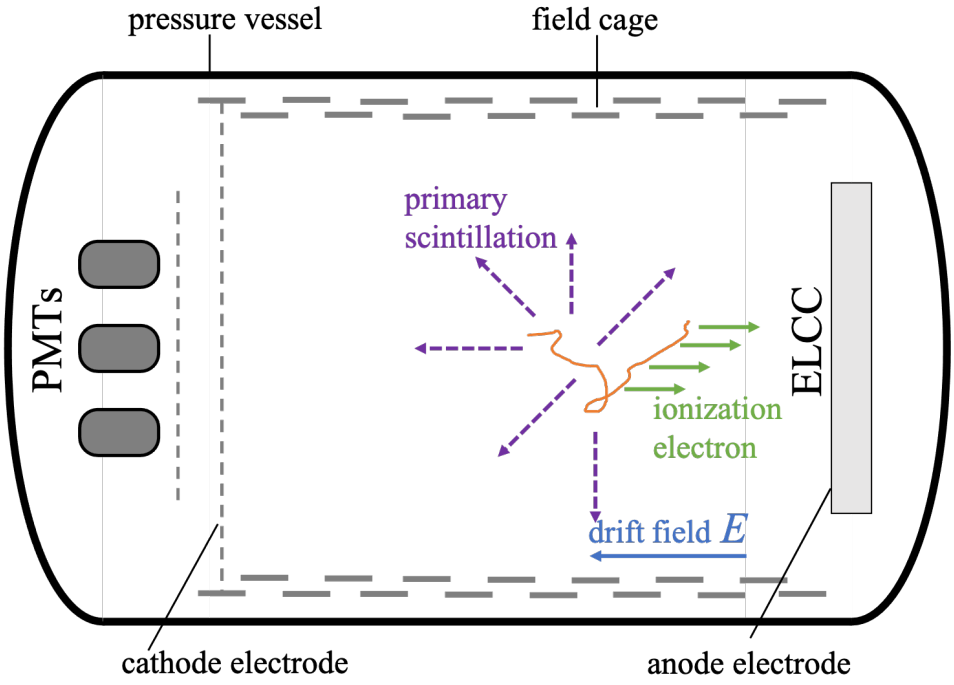

Figure2.1: Schematic view of the AXEL detector

particles, for example, β-rays generated in $0\nu\beta\beta$ or other background events, deposit their energies by exciting and ionizing the xenon atoms along the tracks. Excited atoms emit the primary scintillation photons with a wavelength of $\sim$175 nm in the timescale of several tens of nanoseconds [37]. The scintillation photons are detected by vacuum ultraviolet (VUV) sensitive photomultiplier tubes (PMTs) at the end of the cathode side. Ionization electrons drift toward the anode side with a constant drift velocity under the uniform electric field made by the field cage in the timescale of tens of microseconds. At the end of the anode side, a pixelized electron detector called Electroluminescence Light Collection Cell (ELCC) is placed. At ELCC, ionization electrons generate secondary scintillation photons with the electroluminescence process (EL process), and the photons (EL photons) are detected by photosensors. The details of ELCC are described in Sec. 2.1.1. The deposited energy of an event is derived from the photon counts at the ELCC which is proportional to the number of ionization electrons. The three-dimensional track pattern of an event is reconstructed from the two-dimensional hit pattern at the ELCC and the time interval between the hits of PMTs and ELCC.

The AXEL detector is expected to simultaneously achieve the three conditions for a sensitive $0\nu\beta\beta$ search described in Sec. 1.6 at a high level: A large amount of ^{136}Xe can be achieved by enriched high-pressure xenon gas, the good energy resolution can be achieved by the ELCC readout, and background rejection can be achieved by discriminating gamma-ray events through three-dimensional track reconstruction.

2.1.1 Electroluminescence Light Collection Cell

ELCC is a pixelized detector for ionization electrons. A schematic view of ELCC is shown in Fig. 2.2. ELCC is designed to achieve the high energy resolution for a large detection area by the small dependence of the detector response on the initial position of the ionization electrons, and also to achieve the tracking ability by pixelization. ELCC consists of a drift anode electrode, a ground potential mesh electrode, and a polytetrafluoroethylene plate (PTFE body) in between the two electrodes. The anode electrode and PTFE body have holes arranged in a hexagonal lattice pattern, and a VUV-sensitive silicon photomultiplier (SiPM) is placed for each hole behind the mesh electrode. The unit consisting of an anode hole, PTFE body hole, and a SiPM is called a cell. An electric field, called EL field, more intense than the drift electric field is generated by applying high voltage between the anode electrode and the mesh electrode. Then all the electric field lines in the drift region are gathered into the cell as shown in Fig. 2.3. The ionization electrons are drawn into the cells along the field lines when they reach ELCC. In the cells, the ionization electrons generate EL photons through the EL process, which are detected by the SiPMs.

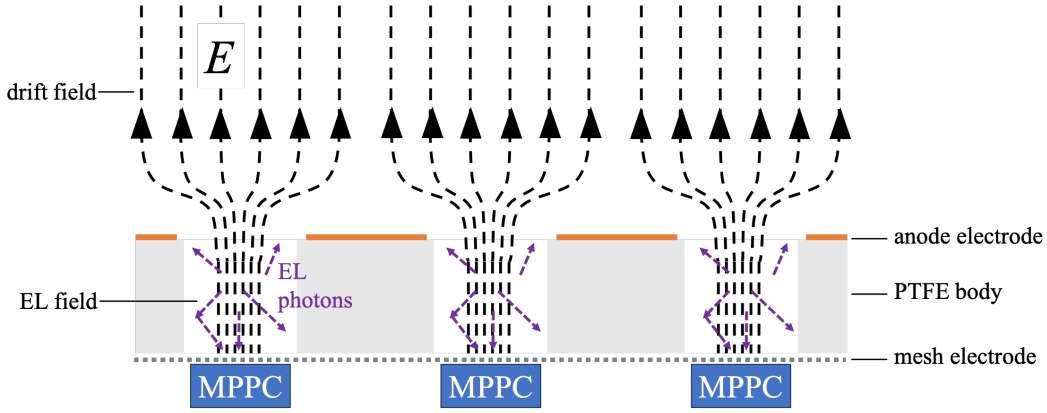

Figure2.2: Schematic cross-sectional view of ELCC

The advantages of ELCC are summarized as below.

- Small position dependence: By applying a strong electric field relative to that of the drift region, ionization electrons are drawn near the center of the cell. Therefore the number of detected photons is less dependent on the initial position of the ionization electrons.
- Rigidness: The electrodes of ELCC is supported by the PTFE body and hence there is little deformation. It leads to less channel by channel variation in the number of generated photons.
- Extendability: ELCC can be divided into units, and hence it is easy to extend the sensitive area by increasing the number of ELCC units. There is no dead region because no additional support for the electrode is necessary.

2.2 Roadmap of the AXEL experiment

We, the AXEL group, have been developing our detector by increasing its size step by step. The first prototype detector used a vessel of a 10 L volume. We demonstrated the proof-of-principle of our detector, especially ELCC, and the first evaluation of the energy resolution was done, with this 10 L prototype detector [48]. The energy resolution in FWHM was (4.0 ± 0.3) % for 122 keV electrons, extrapolated to be 0.9 – 2.0 % FWHM at the Q value.

The second prototype detector uses a vessel of a 180 L volume. The purpose of this 180 L prototype is to acquire the know-how to scale up the detector and to evaluate the performance at the energy around the Q value. For the first phase of the 180 L prototype detector, 168 channels of ELCC, 10 cm of field cage, and two PMTs were installed, resulting in 1455 cm^3 of the sensitive volume. With this first phase, the FWHM energy resolution of (1.73 ± 0.07) %

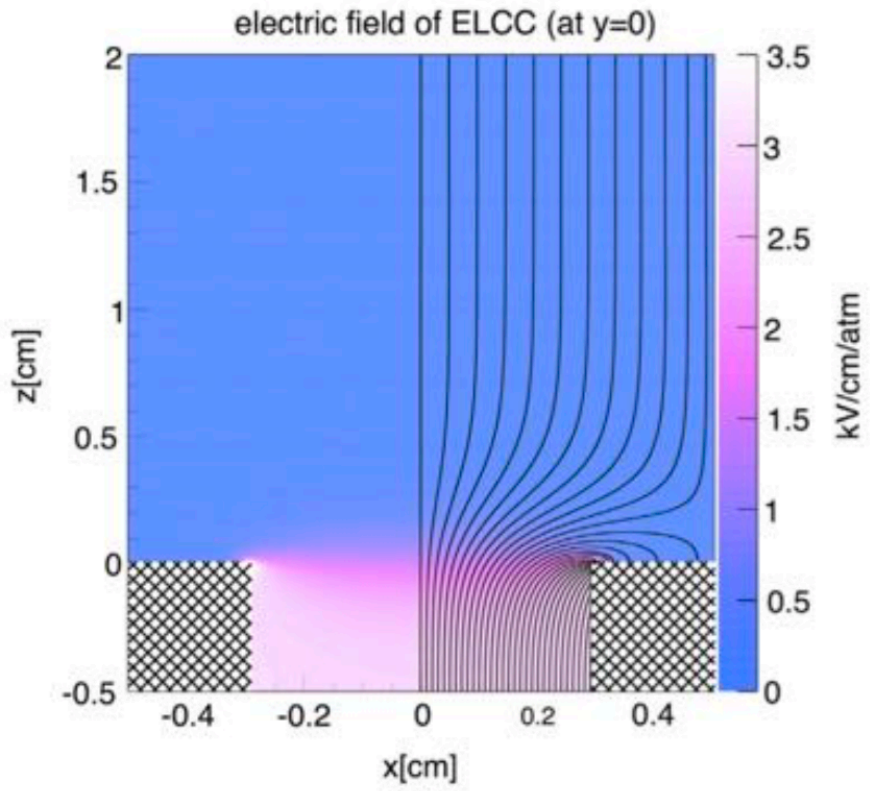

Figure2.3: Electric field strength and field line simulated by Elmer [46] at ELCC. The applied electric field is 100 V/cm/bar for the drift region and 3 kV/cm/bar for the cell. Figure from [47].

for 511 keV electrons was obtained under 4 bar xenon, extrapolated to be 0.79 – 1.52 % FWHM at the Q value [49].

As the second phase of the 180 L prototype detector, it was upgraded with an enlarged sensitive volume to realize the performance evaluation at the energy around the Q value. The detail of the upgrade is described in Sec. 2.3 and Chapter 3. As the first evaluation, the FWHM energy resolution of (0.89 ± 0.03) % for 1836 keV electrons was achieved with this second phase, extrapolated to be 0.79 % FWHM at the Q value [50].

In these studies, only events with energies lower than the Q value were acquired, and the performance evaluation only focused on the energy resolution. Furthermore, the factors determining the energy resolution were mainly unknown. In this thesis, using the second phase of the 180 L prototype detector, events with energies higher than the Q value are acquired (Sec. 6.1), not only the energy resolution but also the parameters determining the reconstructed track image are evaluated (Sec. 6.3), and the factors determining the energy resolution

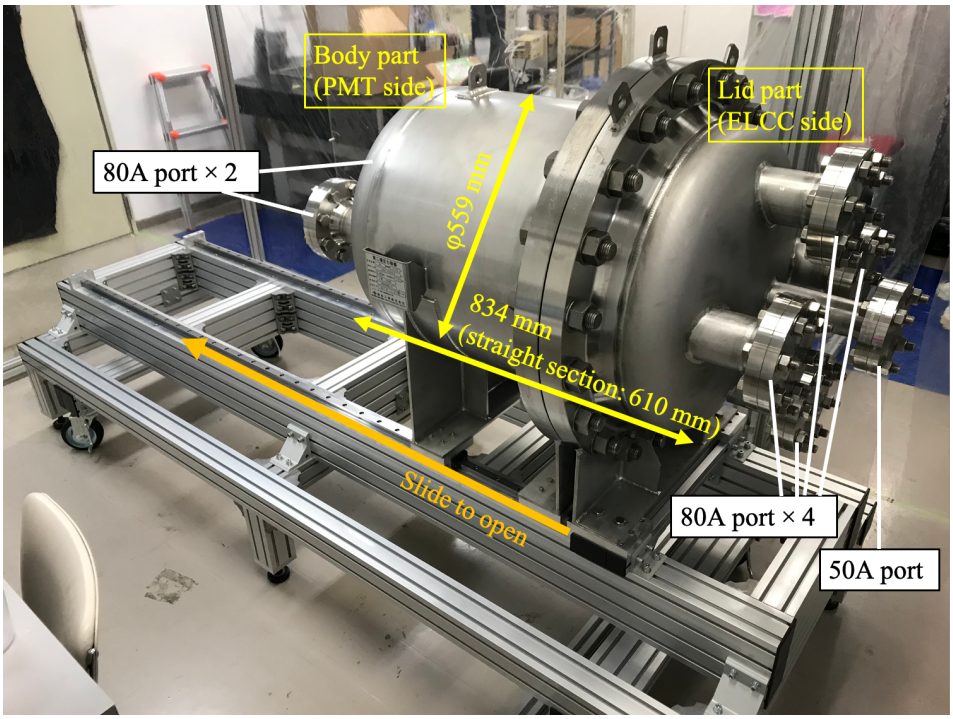

Figure2.4: Photograph of the vessel of the 180 L prototype detector

are thoroughly evaluated without unknown factor (Sec. 7.1).

Based on the techniques developed with the 180 L prototype detector, the detector with a vessel of a 1000 L volume is currently under construction. As the first step, the pressure vessel was constructed and installed in the underground facility of the Kamioka observatory, ICRR, University of Tokyo. A physics search is planned with this 1000 L detector with up to 20 kg of ^{136}Xe. In the future, we envision constructing a 1-ton-scale detector to search for $0\nu\beta\beta$ with a sensitivity of $m_{\beta\beta} = 15\,\text{meV}$–$63\,\text{meV}$.

2.3 180 L prototype detector

Here, the detector components of the second phase of the 180 L prototype detector is described. The upgrades of the 180 L prototype detector from the first phase to the second phase were mainly focused on the enlargement of the sensitive volume to fully contain the events with the energies at around the Q value.

2.3.1 Vessel

Figure 2.4 is a picture of the 180 L vessel. It is made of stainless steel. The cylindrical straight section, 610 mm long, is based on the standard of JIS 550A-sch10; the outer diameter

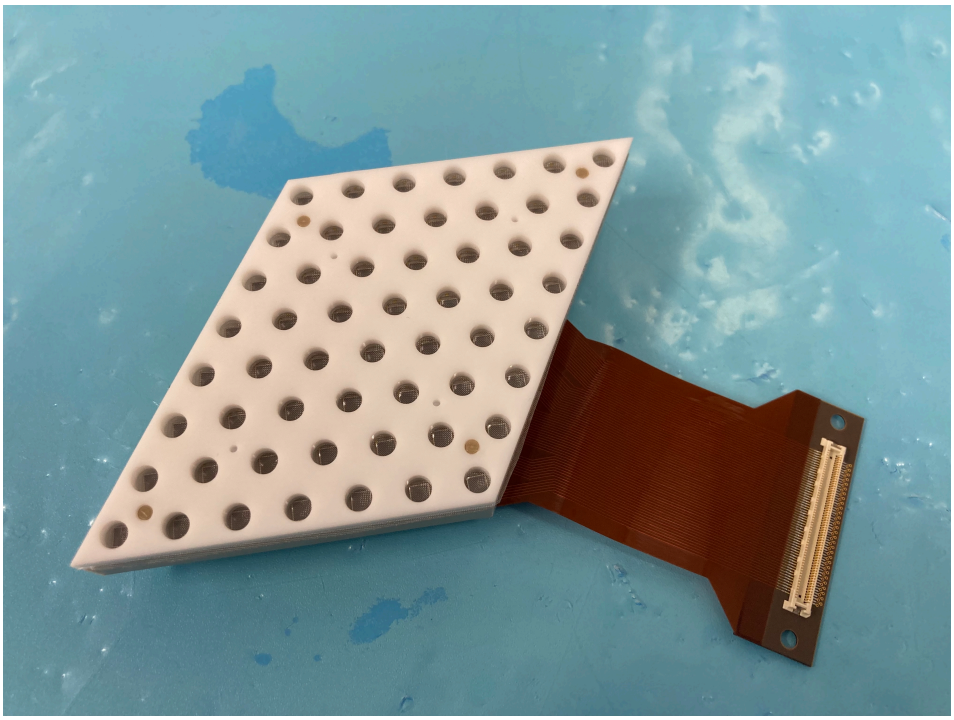

Figure2.5: Photograph of one ELCC unit

is 559 mm and the inner diameter is 547 mm. Both ends are rounded to withstand the pressure. The end-to-end length is 834 mm, resulting in a volume of 180 L. The vessel is divided into two parts. The lid part is fixed and the body part is on rails to be opened by sliding. These two parts are coupled by flanges of JIS 10K550A. There are four JIS 80A ports and one JIS 50A port on the lid part. The 50A port is used for the gas line; evacuation and circulation. One of the 80A ports is used for the anode and cathode high voltage introduction. Another one of the 80A ports is used for the feedthrough of flexible print circuit cables reading out ELCC. On the body part, there are two JIS 80A ports; one is for gas circulation, and the other is for feedthrough of PMT readout.

2.3.2 ELCC

The ELCC plane consists of parallelogram-shaped units with 56 ($= 7 \times 8$) channels each, covering 48.5 cm^2 of sensitive area. For each unit, a flexible print circuit (FPC) is attached to read out the signal and feed the bias voltages of MPPCs. Figure 2.5 is a photograph of one ELCC unit.

The dimensions of ELCC are optimized by simulations in terms of the energy resolution at 30 keV ($\sim$ the energy of K_α X-ray) for the drift field of 100 V/cm/bar and the EL field of 3 kV/cm/bar. For each set of dimensions, an electric field is calculated by Elmer [46], and the

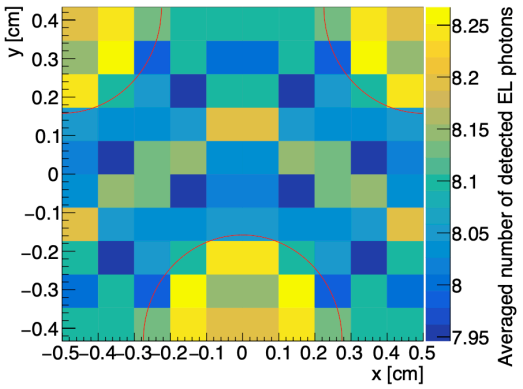

(a) EL gain map for each initial position of electrons. The red circles represent the cell position.

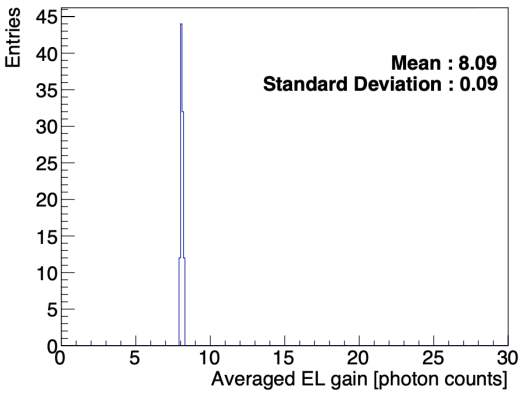

(b) Distribution of EL gain.

Figure2.6: Simulated EL gain dependence on initial positions of electrons. Figures from [47].

number of generated EL photons is calculated based on the path of ionization electrons along the electric field. The optimized dimensions are as follows [49]: the diameter of anode holes is 5.5 mm, the diameter of PTFE body holes is 4.5 mm, the depth of cells is 5 mm, and the pitch of cells is 10 mm.

In this condition, the collection efficiency of initial electrons is 99.96 %. The collection efficiency degrades if the EL field is weaker than 3 kV/cm/bar for the drift field of 100 V/cm/bar. The dependence of the averaged number of detected photons per electron (EL gain) on the initial position of an electron relative to the cell is shown in Fig. 2.6a, and Fig. 2.6b is its one-dimensional projection. The EL gain is sufficiently uniform in terms of the energy resolution.

In the second phase, the number of ELCC units is increased to twelve, and the total number of channels to 672 (Fig. 2.7). The resulting sensitive area is 580 cm^2. The detailed structure of the ELCC unit is changed to suppress discharges between the anode electrode and the mesh electrode, since the ELCC operating voltage is increased with the higher pressure of xenon gas. Figure 2.8 shows the path of discharges and upgraded structure as a countermeasure to the discharges. In the first phase, discharges occurred between the anode electrode and the ground mesh electrode at the boundaries of ELCC units and the screw holes to fix ELCC units. The following countermeasures are taken to prevent these discharges. The PTFE body is separated into two layers. The upper (the anode electrode side) layer is called the cover. The shape of the cover is made different from that of the units in order to shift the boundaries from those of the lower layers. Then, the anode electrode and the ground mesh electrode do not face each other directly. A 125 µm polyimide sheet is inserted between the two layers to block the intersection of the boundary of the cover and the boundary of the lower layer (See

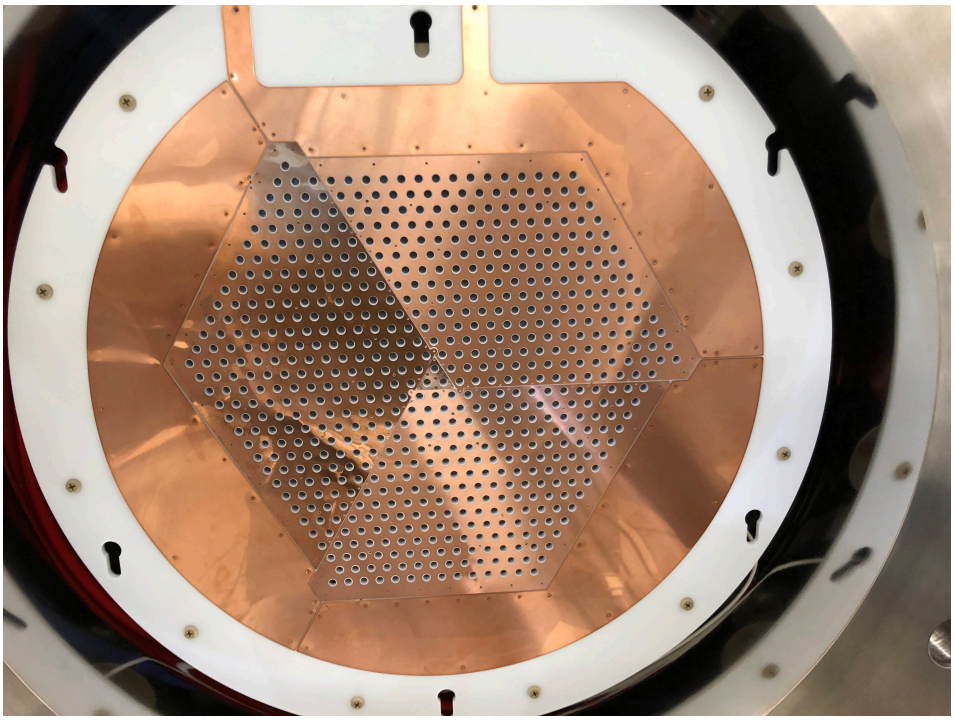

Figure2.7: Photograph of ELCC plane with 12 units and 672 channels.

Fig. 2.9). The direction of the screws to fix ELCC units is reversed so that there are no holes going through the ELCC units.

2.3.3 MPPC

EL photons generated in a ELCC cell are detected by multi-pixel photon counters (MPPCs) made by Hamamatsu Photonics, a kind of silicon photomultiplier. The VUV-sensitive model, S13370-3050CN, is used.

One MPPC consists of an array of avalanche photodiodes (APDs) and quenching resistors (See Fig. 2.10). Each APD is called a pixel. The APDs are operated in the Geiger mode ,i.e. the MPPCs are operated at voltages above the breakdown voltage (V_{br}). When a photon hits a pixel, a sustained electron avalanche occurs, and the voltage drops below V_{br} due to the current flowing the quenching resistor. Therefore, the output charge from a single pixel is a certain constant value with small fluctuations. The output charge of the entire MPPC is the sum of those of pixels and thus is proportional to the number of incident photons when the number of photons is small compared to that of the pixels.

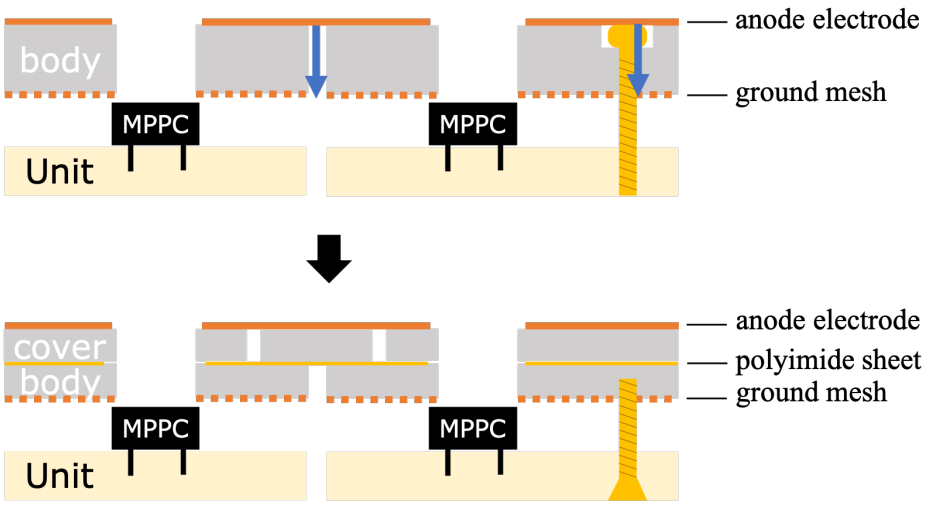

Figure2.8: Schematic cross-sectional views of ELCC structures. The previous structure is shown in the upper part and the upgraded structure to prevent discharges is shown in the lower part. The paths of discharges are shown in the blue arrows in the upper part.

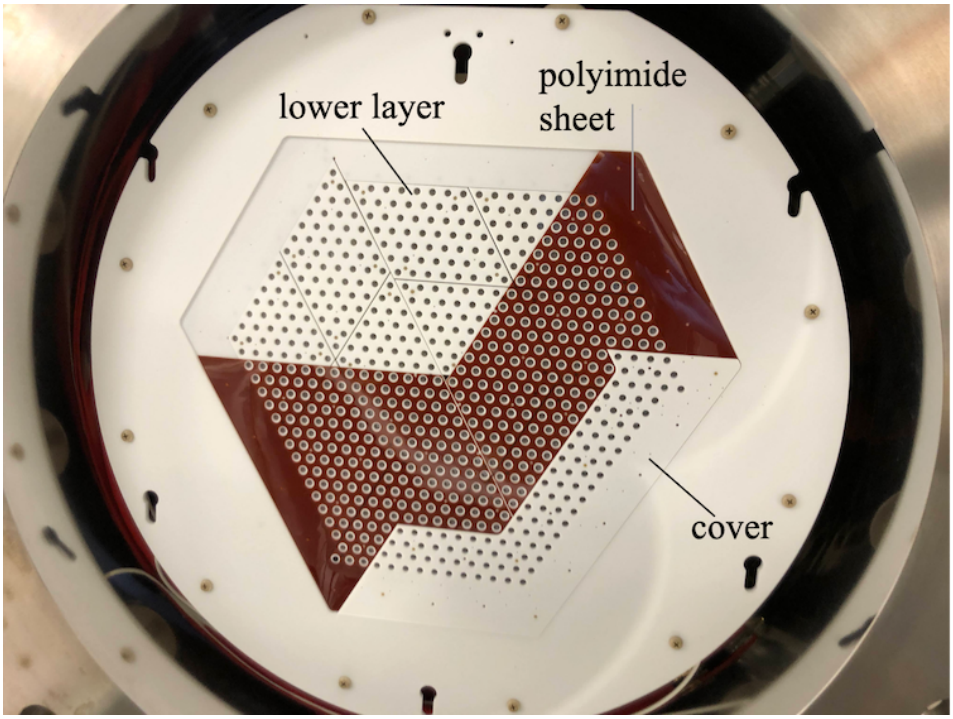

Figure2.9: Photograph of the upgraded ELCC plane during assembly. Part of the polyimide sheets and the covers are removed.

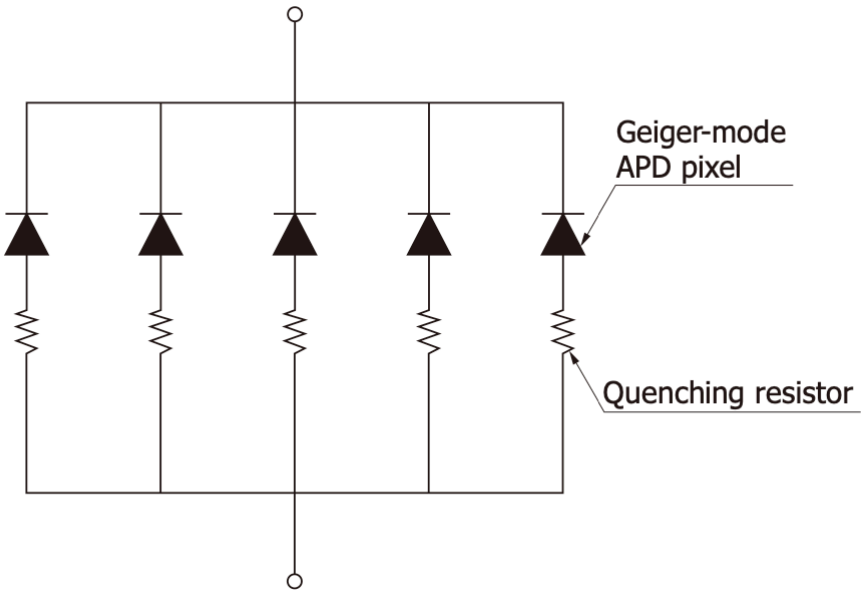

Figure2.10: Circuit diagram of a MPPC. Figure from [51]

The gain of the MPPC is defined as the released charge divided by the elementary charge e when a photon incident and is given as

$$g = \frac{C\,(V_{\mathrm{bias}} - V_{\mathrm{br}})}{e}\ , \tag{2.1}$$

where C is the capacitance of one pixel and V_{bias} is the bias voltage applied to the MPPC.

At a certain rate, pulses are generated in a MPPC regardless of the incident photon. This is called the dark current. The origin of the dark current is considered to be the thermal excitation and tunneling of an electron in the silicon crystal of APDs. The typical rate of the dark current of MPPC S13370-3050CN is $\sim 1\,\mathrm{MHz}$. The amount of the charge of the dark current pulse is mostly one photon equivalent (1 p.e.). Thus the distribution of the charge of the dark current can be used to determine the gain of the MPPC. Figure 2.11 is a typical distribution of the charge of the dark current pulses. The gain is calculated from the mean of this 1 p.e. peak.

For high incident light intensity, MPPCs have a non-linear output. This is because the number of pixels is limited, and it takes a finite time for each pixel to restore the bias voltage after the charge is released by photon detection; the output charge by a photon hit while the bias voltage is being restored is less than the original 1 p.e. charge. Thus, the non-linearity is characterized by the number of pixels and recovery time. The relation between the true number of hit photons, N_{true}, and the observed photon equivalent charge, N_{observed}, is

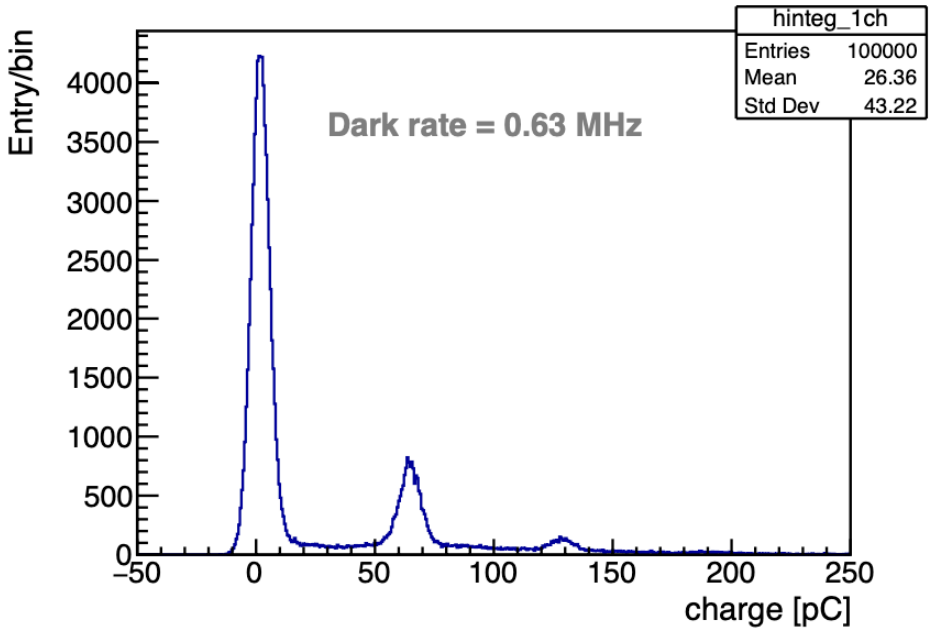

Figure2.11: Typical distribution of the charge of the dark current pulses including pedestal. The peak around the 65 pC is the 1 p.e. peak.

expressed as follows [52]:

$$N_{\text{observed}} = \frac{N_{\text{true}}}{1 + \frac{\tau}{\Delta t \cdot N_{\text{pixel}}} N_{\text{true}}} \ , \tag{2.2}$$

where Δt is the observation time window, τ is the recovery time, and N_{pixel} is the number of pixels, 3600 for our MPPC. Actually, observed photon count fluctuates statistically with N_{observed} as the mean.

The MPPC S13370-3050CN, which we use, has no protective cover or membrane on the APD pixel surface to make it sensitive to VUV. Therefore, they are vulnerable to moisture in the air, and their performance may deteriorate due to moisture absorption when stored in a humid environment. There was a case in which the dark count rate increased more than 10-fold in the MPPCs that were stored without moisture protection measures. It was found that baking at 150 °C for 24 hours could restore this increased dark count rate, and those MPPCs were taken care of. Currently, MPPCs not in use are stored in a desiccator with desiccants to avoid such problems.

2.3.4 Front-end electronics board

The readout of the output and the application of the bias voltage of the MPPCs is done by dedicated front-end electronics board AxFEB [53]. The block diagram of AxFEB is shown in Fig. 2.12. One AxFEB has 56 channels of inputs and reads out one ELCC unit. AxFEB

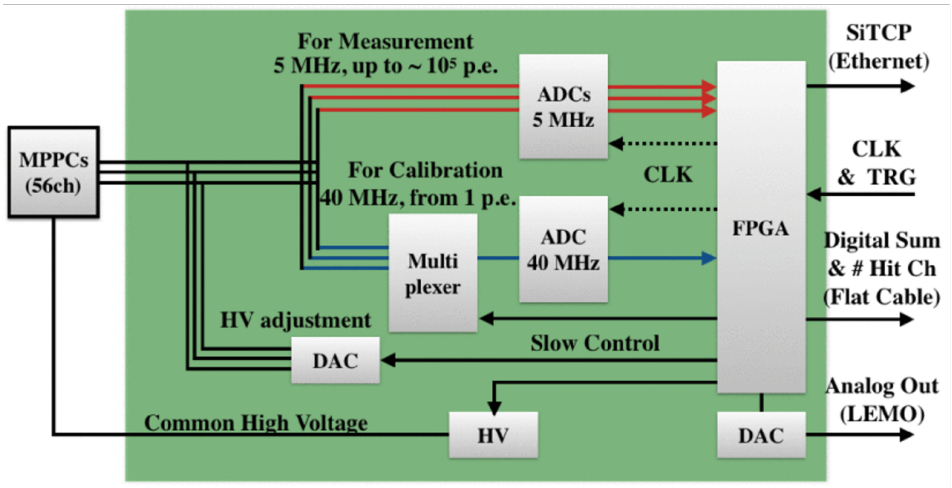

Figure2.12: Block diagram of AxFEB. Figure from [53].

has two types of ADCs. One is a 40 MS/s (MS stands for mega sampling), 2 V peak-to-peak, 12-bit ADC to which 165-times amplified signal is input. It acquires several tens of ns pulses by dark current for the calibration of the MPPC gain. This one is called high-gain ADC. Seven channels share one high-gain ADC via a multiplexer. The other is a 5 MS/s, 2 V peak-to-peak, 12-bit ADC with an amplification of 5 times and a Sallen-Key filter in the front stage. It acquires the EL signal of µs to several hundreds of µs time scale. This one is called low-gain ADC.

In addition to a common bias voltage supply, the bias voltage of each channel is adjusted by the DAC to match the gains of the MPPCs.

2.3.5 PMT

To detect primary scintillation lights in the VUV region, VUV-sensitive and high-pressure tolerant PMTs, Hamamatsu R15298, are used. To improve the detection efficiency of the primary scintillation lights with a larger sensitive volume, the number of PMTs is increased from two to seven (Fig. 2.13). A guard mesh at the ground potential is placed in front of the PMTs. The signals of PMTs are transferred via PTFE-coated coaxial cables, amplified 100-fold with fast amplifiers, and recorded by a 100 MS/s waveform digitizer (CAEN, v1724).

2.3.6 Data acquisition system

An overview of the data acquisition system is shown in Fig. 2.14

As noted in Sec. 2.3.4, one AxFEB is used to read out one ELCC unit. Since the number of ELCC units is twelve (Sec. 2.3.2), twelve AxFEBs are used. To compile the information from

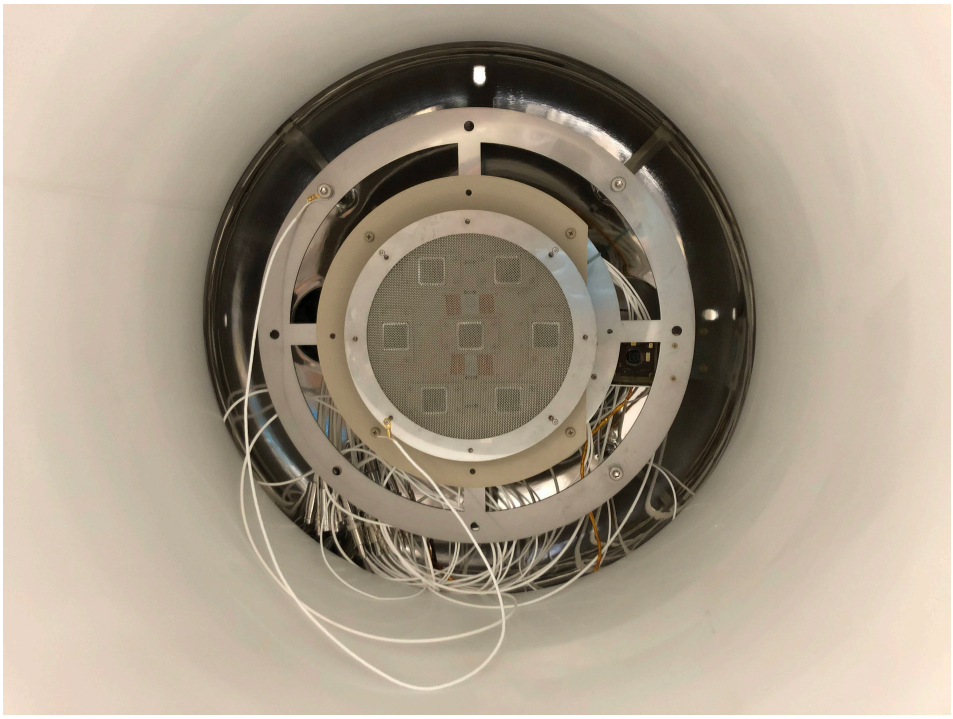

Figure2.13: Photograph of PMT array. A guard mesh at the ground potential is placed in front of the PMTs.

twelve AxFEBs and issue the triggers to all the AxFEBs, a trigger board, Hadron Universal Logic module (HUL) [54], is used. Each AxFEB sends the sum waveform over the channels to HUL, and HUL sends the trigger and veto signal and a common 160 MHz clock to AxFEBs. HUL outputs two other NIM signals. One is called send-trigger signal that is synchronized with the trigger to AxFEBs. The other is called send-header signal which is synchronized with the timing of data transmission to the DAQ PC after waveform acquisition by AxFEBs is complete. The send-trigger signal is recorded in one channel of the waveform digitizer for PMTs to be used to match the timing of the corresponding ELCC events and PMT events. The data acquisition of the PMT signal is triggered by the send-header signal from HUL.

Two kinds of triggers were used for the data acquisition of the ELCC signal. One is called fiducial trigger, which is issued when the sum height of the signal of channels other than the predefined veto channels exceeds a threshold, and the veto channels have no hits. Fiducial trigger is targeting fully contained events. The other, the whole trigger, sets a threshold on the signal sum for all channels including the veto channels. It is to take calibration data targeting 30 keV characteristic X-rays and can be prescaled for low energy events not to dominate the data.

The data from AxFEB and the waveform digitizer for PMTs are independently recorded in

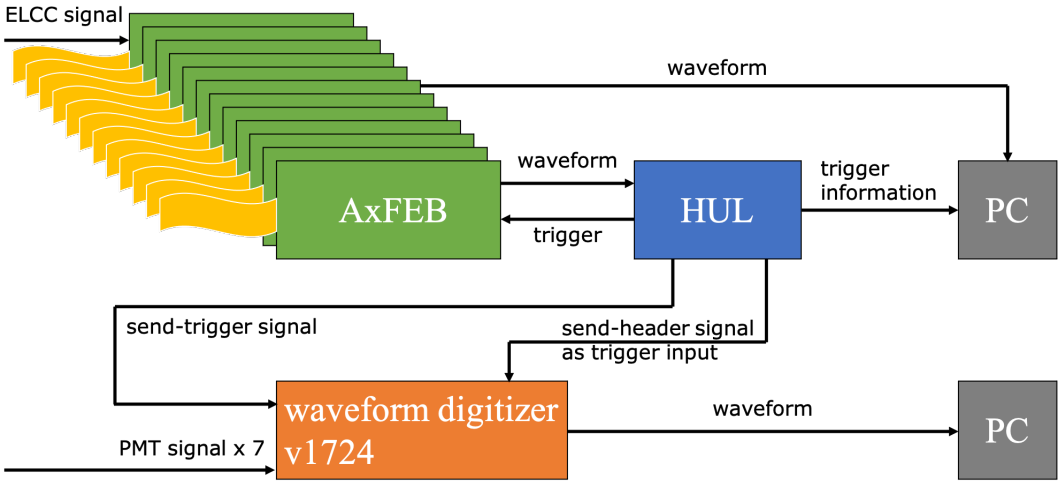

Figure2.14: Block diagram of the data acquisition system.

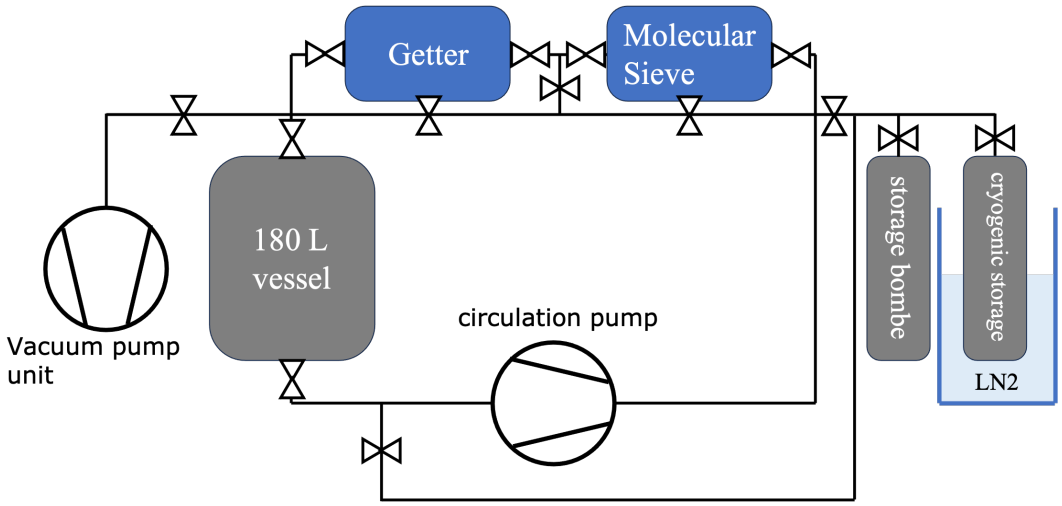

Figure2.15: Gas system for the 180 L prototype detector.

separate PCs. They are matched by software during the analysis phase.

2.3.7 Gas system

Figure 2.15 dipicts the overview of the gas system for the 180 L prototype detector. The gas system has functions of evacuation, introduction, circulation, and retrieval of the gas.

Evacuation is done by the vacuum pump unit, which consists of a turbo molecular pump (Osaka Vacuum, TG350FCAB) and a dry scroll pump (Osaka Vacuum, ISP-250C) as a fore pump. The pumping speed of the turbo molecular pump is 350 L/s.

Introduction, circulation, and retrieval are done by a metal bellows pump (Senior Aerospace,

MB-601HPAL, circulation pump in Fig. 2.15), whose maximum flow is 70 L/min.

During circulation, xenon gas can be purified by two filters; molecular sieve (Applied Energy Systems, 250C-V04-I-FP) for impurities other than N_2, for example, H_2O, O_2, CO_2, and Getter (API, API-GETTER-I-RE) for N_2.

The gas flow is monitored by a mass flow meter (Bronkhorst, F-111CM-40K-AAD-88-K). The purity of the xenon gas is monitored by a dew point meter (Michell Instruments, PURA).

Figure 2.16 shows the actual whole gas system.

To introduce and retrieve xenon gas with the single circulation pump, the storage cylinders (XeST-1 to 4 in Fig. 2.16) are connected both upstream (route through the valves SP-V3 and ST-V2) and downstream (route through the valves ST-V1 and ST-V4) of the circulation pump, and the route is switched by valves.

Not only the circulation route through all of the 180 L vessel, the getter, and the molecular sieve, bypass lines are implemented to allow circulation without passing through each of them (through valves BP-V1 to 4). The gas flow is regulated by a bellows valve (CC-V1) not to extend the rated flow of the getter and the molecular sieve, 5 L/min.

In order to start the circulation pump, the pressure around the pump must be as low as 1 bar. In case the circulation pump stops for some reason during circulation, the pressure around the pump will remain at about 8 bar, making it impossible to restart the circulation pump. To prevent this situation, a vessel for the buffer is installed (Buffer Chamber in Fig. 2.16). With the valves around the 180 L vessel (IN-V2 and CC-V1) closed and the gas in the pipeline being released into the buffer chamber, the pressure is lowered and the circulation pump can be restarted.

At the start of the retrieval of the xenon gas in the vessel, the pressure upstream of the circulation pump is higher than that downstream, thus the load on the pump is low. As retrieval proceeds, the downstream pressure exceeds the upstream pressure, and the load on the pump increases and the flow decreases. When the upstream pressure, the pressure in the vessel, reaches 0.3 bar, the flow stops, and the gas cannot be retrieved anymore by the circulation pump. The remaining xenon gas is retrieved by solidification with liquid nitrogen. To prevent xenon from freezing and blocking at the introduction port of the solidification vessel during solidification, a heater is installed at the introduction port to control the xenon temperature above the boiling point of xenon (165 K).

2.3.8 Field cage

The field cage is a set of electrodes forming the uniform drift electric field. The details of the design and development of the field cage for the 180 L prototype detector are described in Chapter 3. The installed field cage is finally 18 cm long in the drift direction, resulting in a

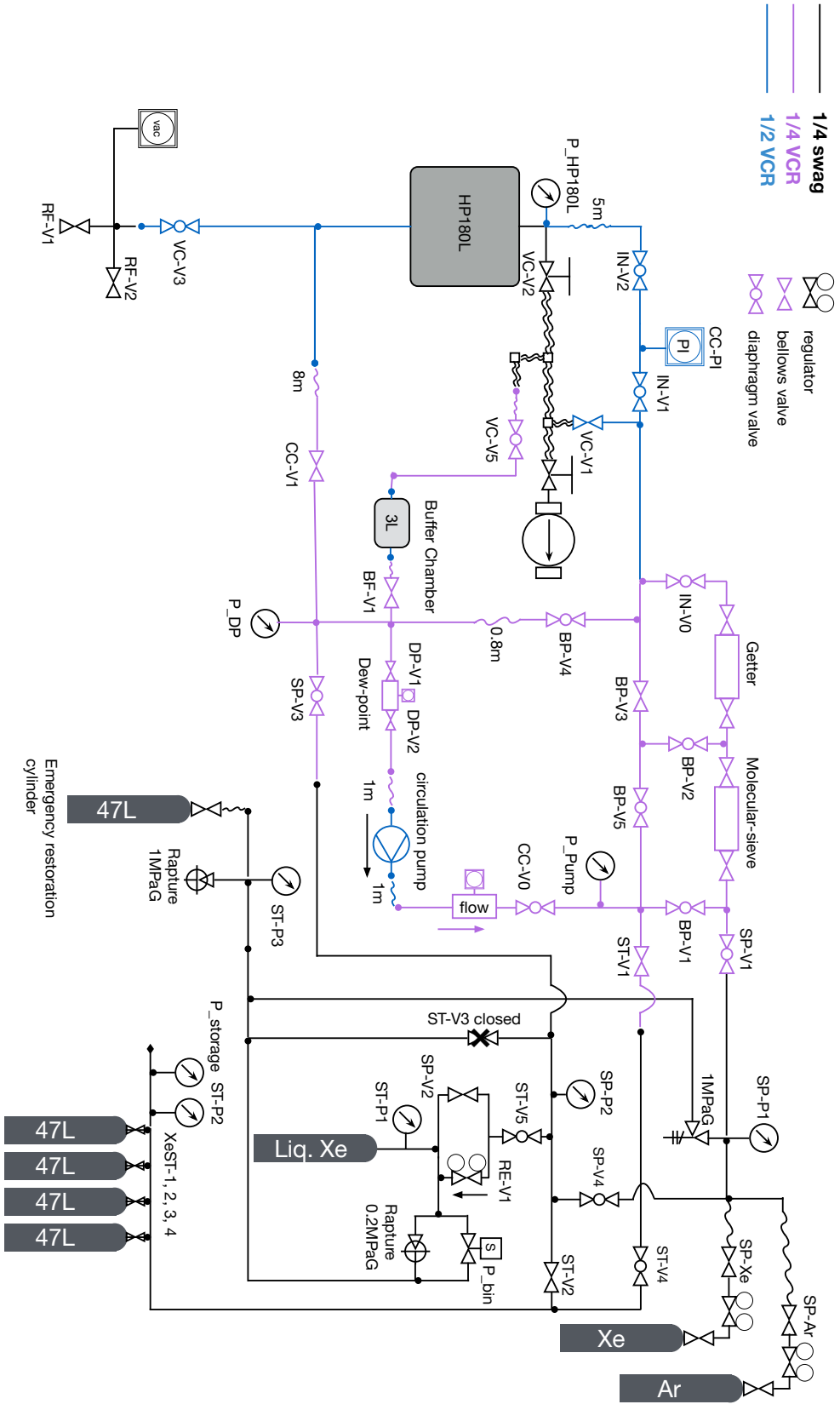

Figure2.16: Pipeline diagram of the whole gas system.

Table2.1: Summary of the detector parameters of the second phase of the 180 L prototype detector.

Detector parameters	
Sensitive area of ELCC	580 cm^2
Drift length	18 cm
Sensitive volume	10 000 cm^3
Number of ELCC channels	672
Number of PMTs	7

sensitive volume of 10 000 cm^3.

2.3.9 Summary

The detector parameters of the second phase of the 180 L prototype detector are summarized in Table 2.1.

3

Design and construction of the field cage for the 180 L prototype detector

The field cage generates a uniform drift electric field and is a key component of the AXEL detector. The quality of the drift electric field affects the energy resolution and track reconstruction capability of the detector through the recombination, attachment, and diffusion of ionization electrons. In this chapter, the requirement for the drift electric field of the AXEL detector, the design of the field cage, and the construction process of the field cage are described.

3.1 Drift electric field

In TPC, ionization electrons are detected after drifting toward the anode under the uniform drift electric field. In case the intensity of the drift field is low, a part of the ionization electrons recombine with ions, and hence the detected number of ionization electrons gets reduced, resulting in worse energy resolution with a fluctuation of recombination.

The relation between the recombination rate and the intensity of the drift field can be approximated [55] by

$$\frac{Q\left(E_{\mathrm{drift}}\right)}{Q_0} \simeq 0.8 + 0.2\left(1 + \frac{K_2}{E_{\mathrm{drift}}}\right)^{-1}, \tag{3.1}$$

where $Q(E_{\mathrm{drift}})$ is the number of detected ionization electrons, Q_0 is the number of ionization electrons produced, and E_{drift} is the intensity of the drift field. The K_2 represents the degree of recombination, and was measured to be $(0.137 \pm 0.048)\,\mathrm{kV/cm}$ at 10 bar [55]. According to Eq. 3.1, the detected ionization electrons is 97.6 % when the drift field is 100 V/cm/bar, and the degradation of the energy resolution is negligible. Thus 100 V/cm/bar is sufficiently high intensity. Actually, the relation between the drift electric field and the energy resolution in a high-pressure xenon gas detector was directly measured in [56], and the result is shown

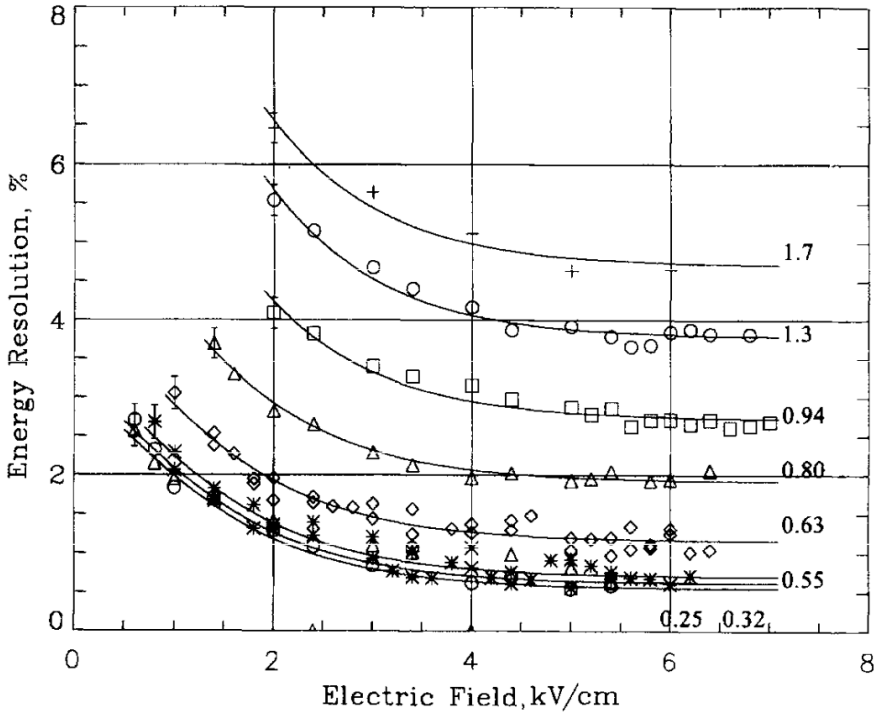

Figure3.1: Field dependence of the intrinsic energy resolution (%FWHM) measured for 662 keV gamma-rays. Densities in the unit of g/cm^3 are shown at right of the curves. [56]

in Fig. 3.1. The energy resolution for 662 keV gamma rays reaches to 0.6 % for the drift electric field of $\gtrsim$ 4 kV/cm for the xenon gas density of 0.25 g/cm^3. This corresponds to $\gtrsim$ 100 V/cm/bar. Thus we have set the target value for the drift electric field of the AXEL detector as 100 V/cm/bar.

The requirement for uniformity is also considered based on Eq. 3.1. In case $E_{\rm drift}$ deviates 5 % from 100 V/cm/bar, the change in the $Q(E_{\rm drift})$ is roughly 0.1 %. This is small compared to the intrinsic energy resolution of 0.26 %. Therefore the allowed deviation is set to be 5 %, which is sufficiently small in terms of the energy resolution.

While ionization electrons are accelerated by the drift electric field, they undergo many scattering by surrounding xenon atoms. As a result, the ionization electrons drift with a constant velocity on average and diffuse with certain rates in the transverse and longitudinal directions with respect to the drift direction. Diffusion is a statistical process and described by a Gaussian function with the standard deviation of $\sigma_{L,T}$:

$$\sigma_{L(T)} = D_{L(T)}\sqrt{v_d t}\ , \tag{3.2}$$

where $D_{L(T)}$ is the longitudinal (transverse) diffusion constant, v_d is the drift velocity and t is the time of the drift. In other words, diffusion is proportional to the square root of the

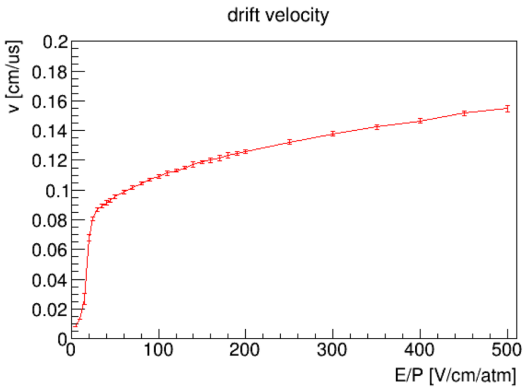

(a)

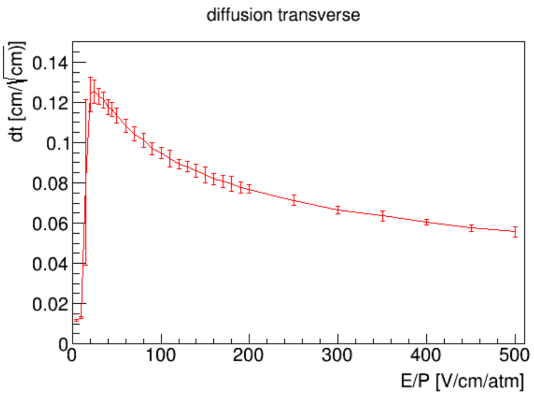

(b)

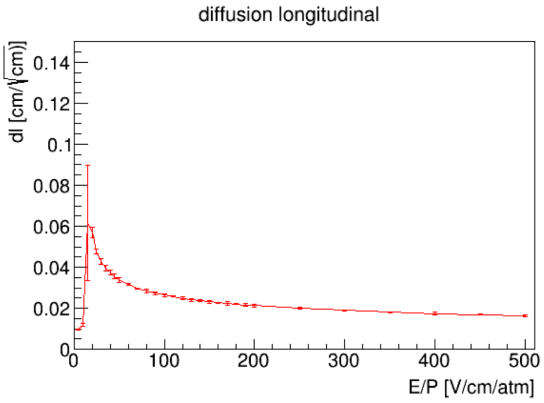

(c)

Figure3.2: Field dependence of the drift velocity (a), transverse diffusion constant (b), and longitudinal diffusion constant (c) calculated with Magboltz [57]. The calculation is done under the condition of 8 bar gas pressure and no magnetic field.

drift distance. Figures 3.2a, 3.2b, and 3.2c show the field dependence of the drift velocity and diffusion constants calculated with Magboltz [57] which incorporates the cross sections from the database [58]. The drift velocity at 100 V/cm/bar is calculated to be 0.11 cm/µs. The diffusion constants are 0.095 cm/$\sqrt{\text{cm}}$ for the transverse and 0.025 cm/$\sqrt{\text{cm}}$ for the longitudinal at 100 V/cm/bar. For example, the diffusion after a 10 cm drift is 0.3 cm for the transverse and 0.08 cm for the longitudinal. These are comparable to the position resolution for the transverse and longitudinal direction determined by the pitch of ELCC (1 cm) and the sampling speed of the FEB (0.2 µs for 1 sampling) respectively. Therefore the target value of 100 V/cm/bar is acceptable in terms of the track pattern reconstruction. In other words, the spatial resolution cannot be improved significantly even if the pitch of ELCC cells is shortened, or the sampling

rate of the signal readout is improved.

On the uniformity, the drift velocity is on a plateau at 100 V/cm/bar, and hence the deviation of the drift velocity by the 5 % deviation of the drift electric field is less than 1 %. Assuming the extreme case that the drift velocity is 1 % deviated for the full 50 cm drift, the error in the position reconstruction is 1 % of 50 cm, 5 mm. This is comparable to the transverse diffusion after 50 cm drift, 6.7 mm. Hence the deviation of 5 % in the drift field is also acceptable in terms of the track pattern reconstruction.

In conclusion, the requirement for the drift electric field is to achieve 100 V/cm/bar within the deviation of 5 %.

3.2 Design of the field cage

The goal of the field cage is to achieve 100 V/cm/bar ± 5 % in as large a volume as possible within the 180 L vessel. The ground potential of the vessel may distort the electric field in the vicinity of the vessel. To shield this ground potential of the vessel, the following structure was adopted: band-shaped rings with two different diameters are alternately lined up with overlaps as shown in Fig. 3.6. The potential difference between the anode and the cathode electrode is divided and equally distributed to each ring electrode. In order to optimize the dimensions, the electric field was calculated with an axisymmetric in the finite element method by FEMM [59]. The distance between the cathode and the anode electrodes, and the pitch of the band-shaped electrode, 10 mm, are fixed. The other dimensions like the radius, thickness, width, and radius of the edge of the band-shaped electrodes are the targets of the optimization. The optimized configuration is shown in Fig. 3.3. The band-shaped electrodes are 3 mm thick and 12 mm wide. The radii of the larger (outer) and smaller (inner) electrodes are 252.5 mm and 244.5 mm, respectively. They are aligned with overlaps of 2 mm. A 20 mm thick cylinder of high-density polyethylene (HDPE) insulates the outer electrode and the vessel.

The calculated field is shown in Fig. 3.4. The electric field in the central axis direction met the condition of 100 V/cm/bar ± 5 % within the radius of 229.3 mm from the central axis. This is sufficiently larger than the 12-unit ELCC.

To prevent electric discharges between the electrodes is also important in the design of the field cage: Frequent discharges impair the stability of the applied high voltage, and eventually carbonized and conducting discharge paths cause a short, making it impossible to apply high voltages. There is a risk of discharge if there are local regions of strong electric field. Figure 3.5 shows the electric field intensity around the electrodes. The edges of the band-shaped electrodes are rounded off with 0.3 mm radii to reduce the intensity of the local electric field. The intensity of the electric field between the inner electrodes and between the inner and the outer electrodes are smaller than 500 V/cm/bar, sufficiently small. The intensity of the elec-

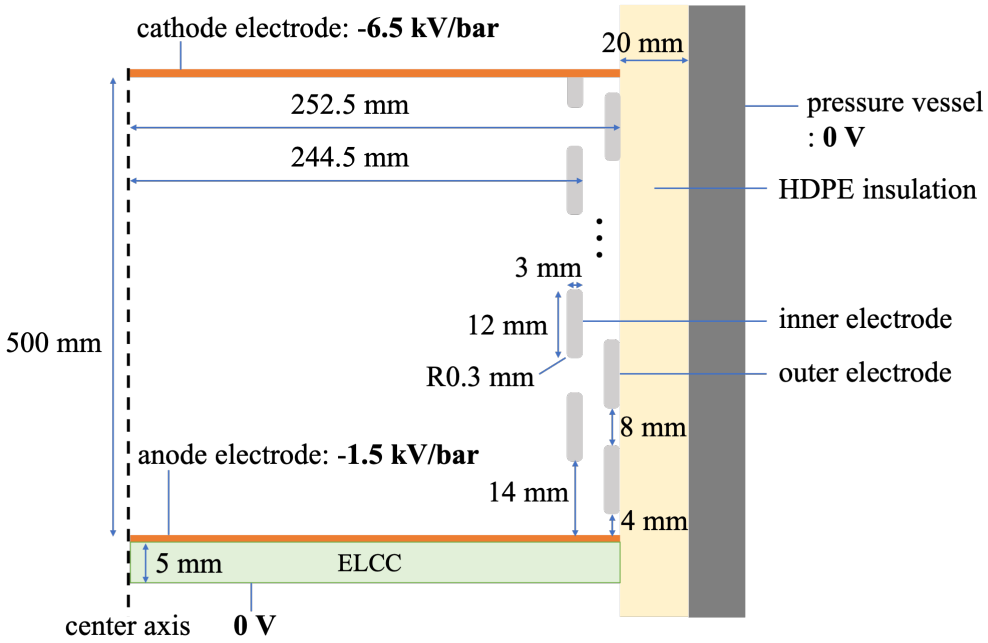

Figure3.3: Configuration in the electric field calculation by FEMM and optimized dimensions.

tric field between the outer electrodes exceeds 1 kV/cm/bar. This exceeds the threshold of the EL process. Ionization electrons produced by radioactivity may generate EL photons, and the generated VUV EL photons strike out electrons from the surrounding materials, which causes the positive feedback of electron emission and induces discharges. However, it is expected that the HDPE surface is eventually charged up, and the intensity of the electric field of this region is much weakened.

3.3 Construction

The field cage was constructed based on the above design. Figure 3.6 is a photograph of the constructed field cage.

The inner and outer electrodes are made of aluminum. Aluminum reflects VUV light, so it is adopted to increase the detection efficiency of the primary scintillation light. A small number of electrodes made of oxygen-free copper were also manufactured and tested as an option. Although it does not reflect scintillation light, oxygen-free copper may be advantageous in future detectors because it has less outgassing and radioactive impurities than aluminum. The oxygen-free copper electrodes are made with a thickness of 1.5 mm to reduce the mass. Each electrode has a straight section of 300 mm to make cabling space between the HDPE insulating cylinder and the field cage.

The cathode electrode is made of stainless steel mesh with an aperture of 71 % to pass

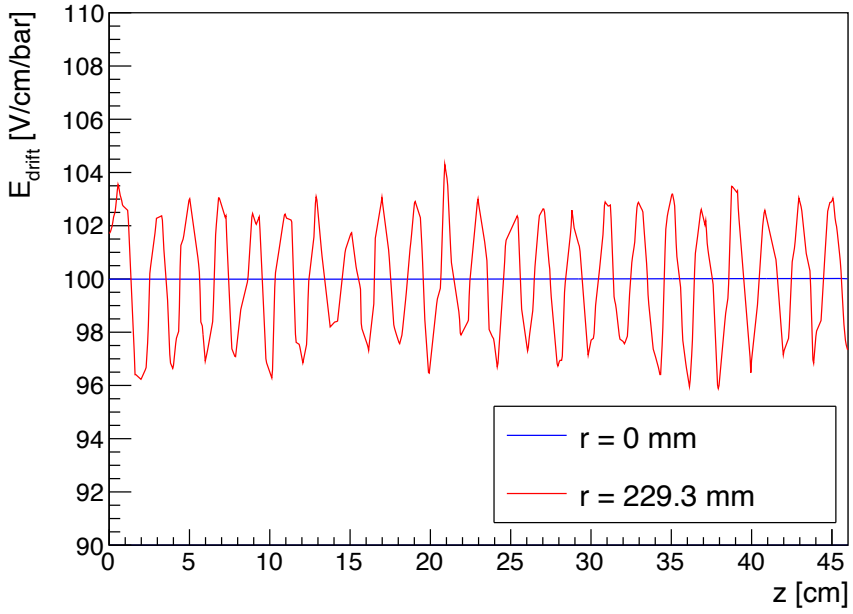

Figure3.4: The calculated electric field component of the central axis direction. The blue line shows the intensity on the central axis ($r = 0\,\mathrm{mm}$), and the red line shows the intensity on the most far line from the central axis satisfying the condition of $100\,\mathrm{V/cm/bar} \pm 5\,\%$ ($r = 229.3\,\mathrm{mm}$).

through the primary scintillation light. The mesh was point welded to a 1 mm thick stainless steel frame under tension, and thus deflection of the mesh is kept small.

The electrodes are fixed on six pillars made of polyetheretherketone (PEEK) by PEEK screws from the inside. One end of each pillar is fixed to the PTFE disk hosting ELCC units and the anode plane. To suppress surface discharge between the electrodes, the surface of the PEEK pillar is stepped, and PTFE spacers are placed between it and the electrodes (Fig. 3.7).

In fact, placing the pillars inside the field cage may distort the electric field around the pillars in the sensitive area due to the charge-up to the pillars. Within the scope of this thesis, this possible distortion of the drift field is not a problem because the outermost channels of 12-unit ELCC are well away from the pillars ($\sim 7\,\mathrm{cm}$). However, it may be problematic for the cases of future expansion and the future 1000 L detector. Nevertheless, placing the pillars inside the field cage was adopted to avoid discharges that could occur if the columns were placed outside the field cage. A schematic illustration of this discharge is shown in Figure 3.8. Charge-up between the surface of the pillar and the HDPE insulation wall may strengthen the electric field on the side surface of the pillar. At some point, the accumulated charge could be

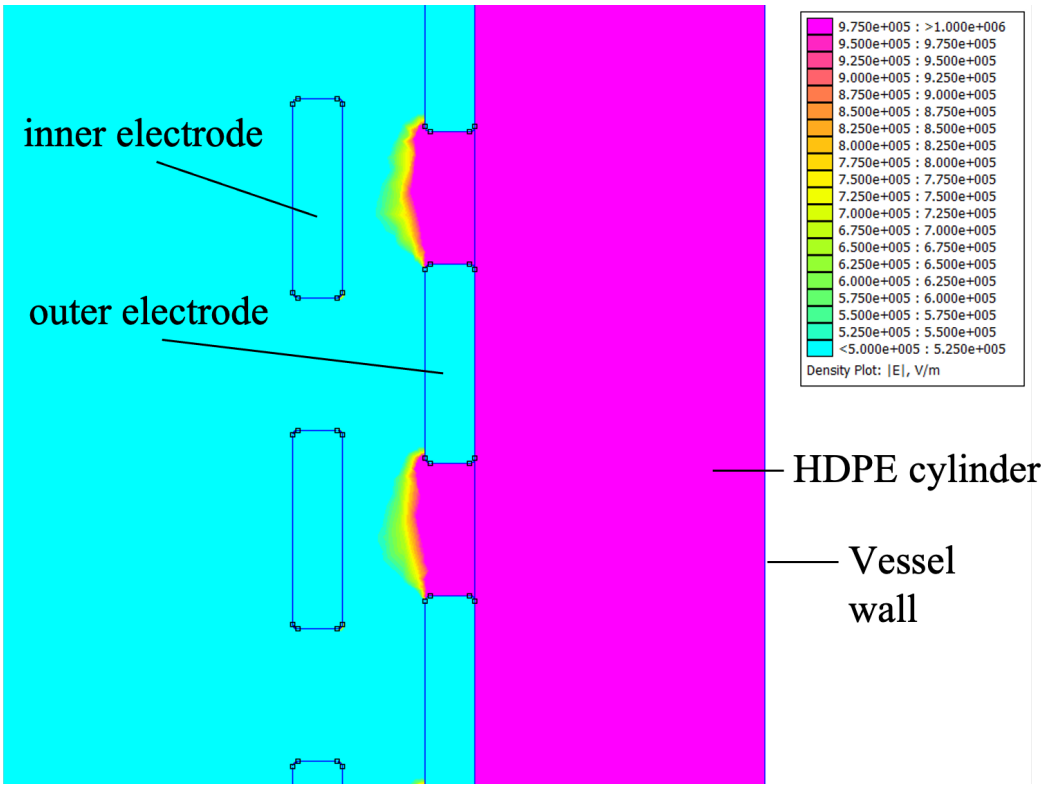

Figure3.5: Intensity of the electric field around the inner and the outer electrodes. The calculation assumes the xenon gas pressure of 10 bar, and hence the color scale corresponds to from 500 V/cm/bar to 1 kV/cm/bar.

released all at once through the side surface of the pillar. When designing the field cage for the 1000 L detector, it is desired to design a structure that can solve this pillar problem such as making azimuthal dips in the inner wall of the HDPE insulator.

The HDPE insulating cylinder was made by bending a single 15 mm thick plate of HDPE and fusing the ends. The thickness was reduced from the 20 mm in the electric field simulation to allow for the electrodes to fit without being stuck. Since the withstand voltage of HDPE is ~ 30 kV/mm, 15 mm thick of HDPE can insulate ~ 450 kV. The voltage of the electrode is 60 kV in maximum, thus the thickness of the HDPE cylinder is sufficient.

Negative high voltage is applied to the cathode mesh via a cable made of wires and silicone rubber cover (Accu-Glass Products, SIL-TYP26-15'), which is tolerant up to 30 kV. The cathode, the inner and the outer electrodes, and the anode are connected in series via 100 MΩ resistors to equally apply potential differences between neighboring electrodes. The resistors are fixed on the PEEK pillar on the straight section of the electrodes by the same screws fixing electrodes on the pillar. To electrically connect the electrodes and resistors, stainless steel screws are used insted of PEEK screws for other pillars (Fig. 3.9).

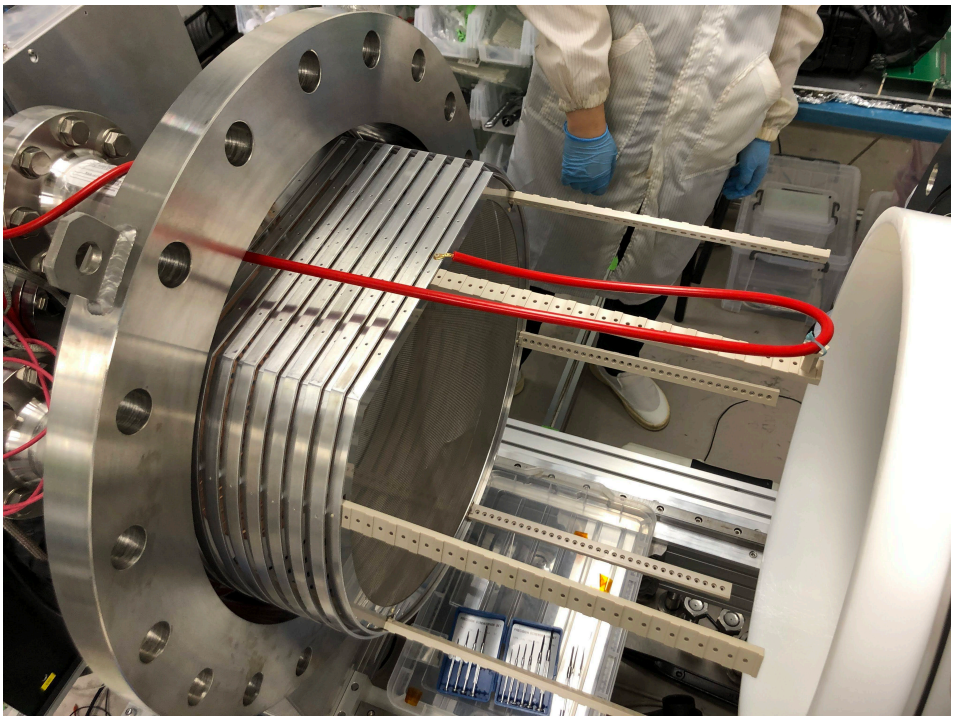

Figure3.6: Photograph of the field cage. It is supported by the lid part of the vessel. A white cylinder on the right side is the HDPE insulator.

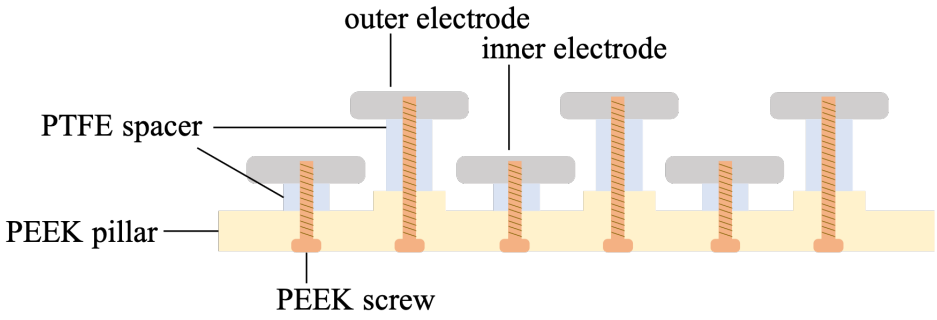

Figure3.7: Schematic cross-sectional view of the electrodes fixed on the PEEK pillar.

Due to the limitation of the cathode high voltage supply, the number of installed electrodes this time is nine for the inner and nine for the outer. Hence the length between the cathode mesh electrode and the anode plane, the drift length, is 18 cm, which was 10 cm before this upgrade.

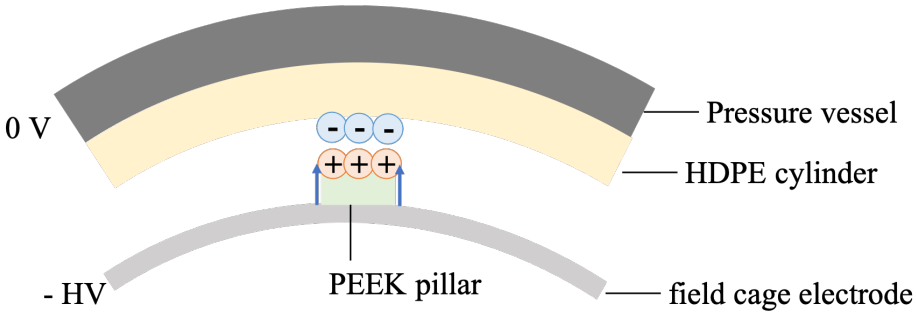

Figure3.8: Schematic illustration of the possible discharge on the outside pillar. The blue arrows show the path of the discharge. View from the drift direction.

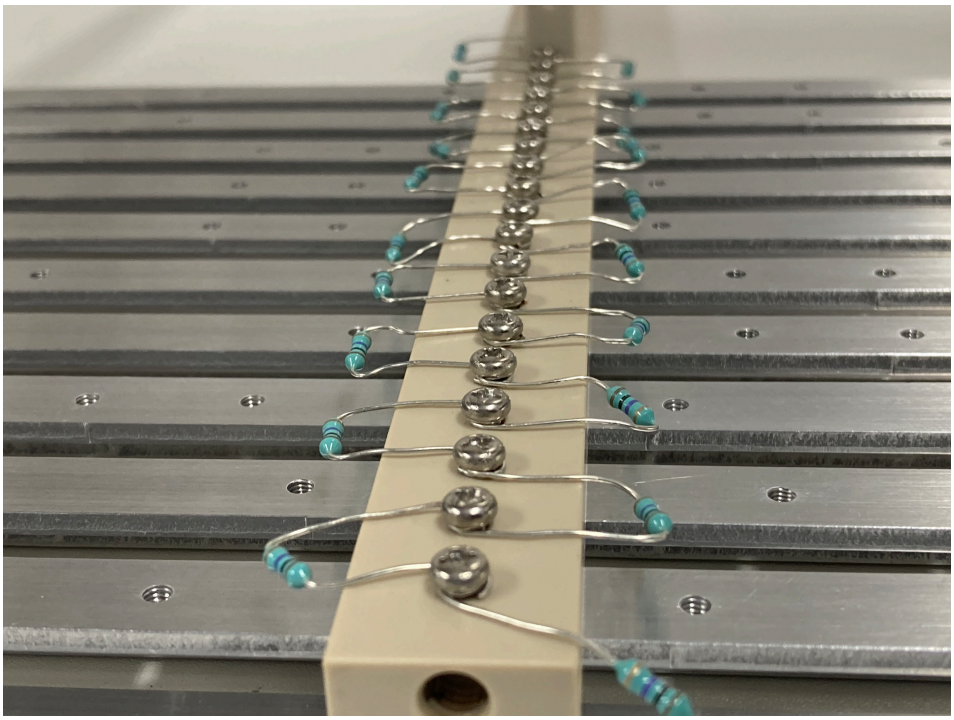

Figure3.9: Photograph of the resistor chain dividing the high voltage.

3.4 Commissioning of the field cage

During the first commissioning of the assembled field cage in xenon gas, frequent discharges occurred. The field cage was examined to identify the location of the discharges from their traces. There was a long trace of discharge on the surface of the silicone rubber coating of the high voltage feeding cable (Fig. 3.10a). There were also burn traces on both sides at the cathode side of the PEEK pillar at the straight section. They ran between the stainless steel

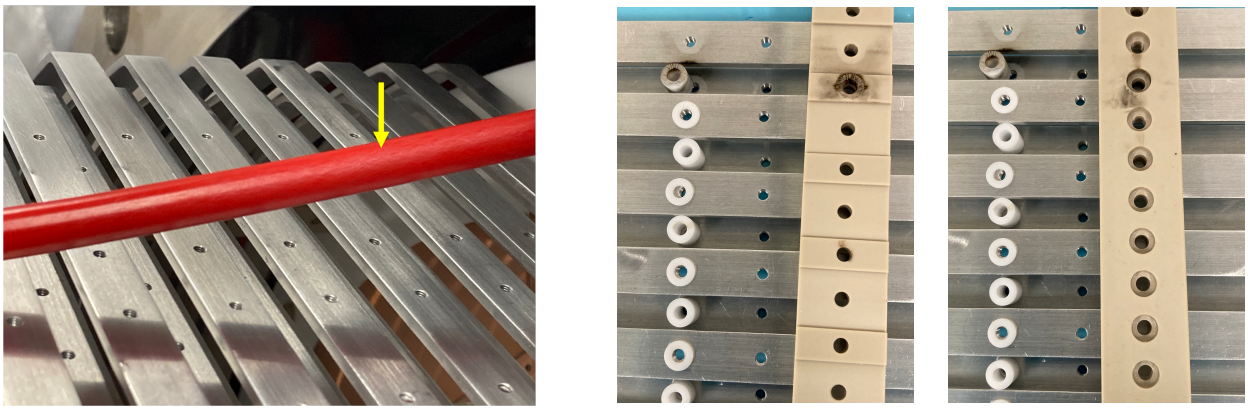

(a) (b)

Figure3.10: Trace of the discharge found in the inspection. On the high voltage feeding wire (a) and on the PEEK pillar at the straight section of the band electrode (b).

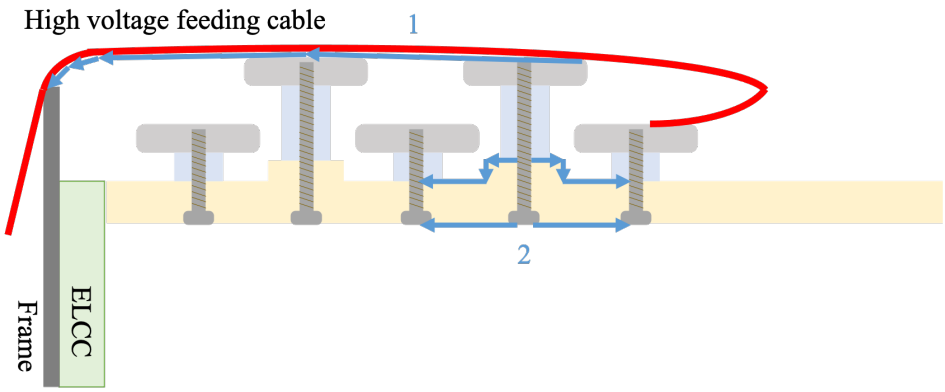

Figure3.11: Inferred mechanism of the discharges occurred in the high voltage applying test. Paths of the discharges are shown by the blue arrows.

screws holding the electrodes and resistors (Fig. 3.10b).

Based on these traces, we consider that discharges have occurred as illustrated in Fig. 3.11. First, the high voltage feeding cable was sagging and touching the inner electrode closest to the cathode and the stainless steel frame holding the ELCC. Thus a discharge on the cable surface occurred between the inner electrode and the frame. Then, because the first discharge lowered the potential of the inner electrode contacted by the cable, the potential difference between it and the upper and the lower outer electrodes increased, causing discharges between the screws.

To suppress these discharges, the following countermeasures were taken. A jig was installed to support the high voltage feeding cable so that the cable is lightly tensioned and does not touch the electrodes (as shown in Fig. 3.6). The cable was wrapped by 125 µm thick

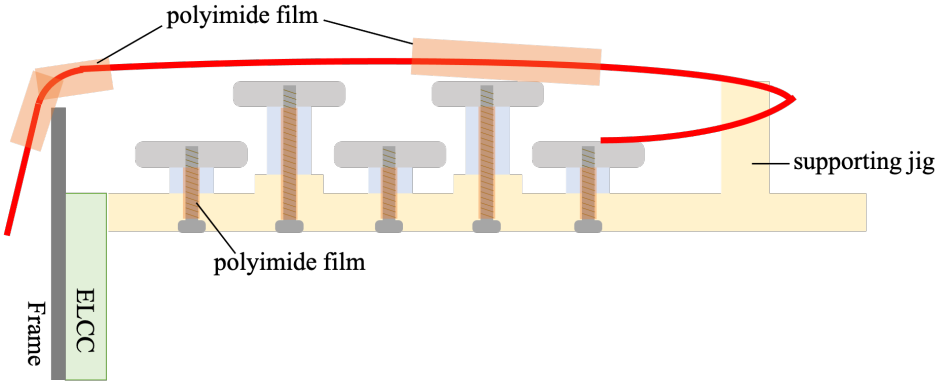

Figure3.12: Summary illustration of the countermeasures taken to suppress discharges.

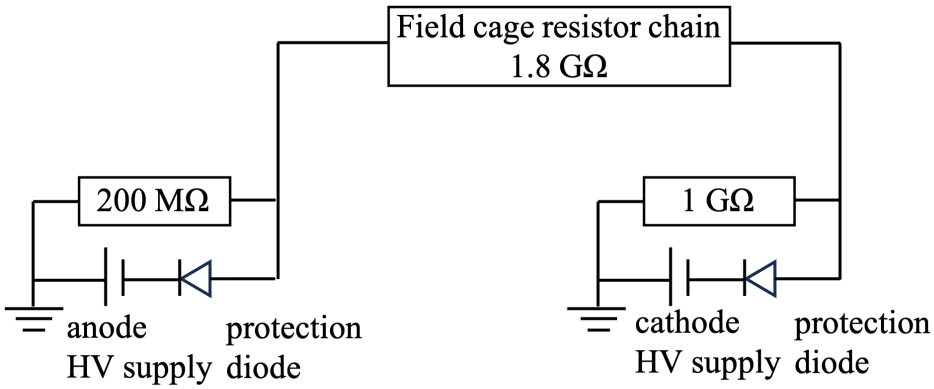

Figure3.13: Diagram of the high voltage supplying system.

polyimide films to prevent direct contact at points near the frame and electrodes where there is a possibility of contact. The stainless steel screws which fix the electrodes and the resistor chain were wrapped by 50 µm thick polyimide films to conceal the screw threads. These countermeasures are illustrated in Fig. 3.12. With these countermeasures, the rate of discharge was reduced, and the remaining discharges became not destructive. Hence it became possible to conduct a measurement.

3.5 Interlock system for discharges

Figure 3.13 shows the diagram of the cathode and anode high voltage supplying system. Each high voltage supply has a load resistor and protection diode to prevent it from being damaged by reverse current. The output currents are hence 34 µA for the cathode and 52 µA for the anode in case of the operation with the EL field of 3 kV/cm/bar and the drift field of 100 V/cm/bar.

The interlock system is implemented for each high voltage supply so that the supply of voltage can be cut off immediately to stop the discharges when they occur. The interlock systems monitor the output current of each high voltage supply which rapidly increases in case of discharges. The interlock system is realized by a data logger (Graphtec, GL820). The analog outputs proportional to the output current of the high voltage supply are input to the data logger, and the 5 V alarm outputs of the data logger monitoring the output current are input to the power control of the high voltage supplies which cut the power to the high voltage supplies when 5 V signal is input. The threshold for the alarm output is set at 300 µA for the cathode and 450 µA for the anode respectively.

Another option for the interlock for discharges is to monitor the rate of signals from PMTs, i.e., monitoring the frequent emission of light due to discharges. The PMT output is input to a NIM discriminator. The output of the discriminator is converted to TTL pulses by a level converter, and the TTL pulse is counted by a digital pulse counter. The pulse counter outputs analog voltage (0 V to 10 V) proportional to the counted pulse frequency. The output voltage is input to the data logger and another alarm output is fired when the pulse frequency exceeds 1000 Hz. This option was also implemented but not used because it is not possible to distinguish between discharges at the anode side and the cathode side.

After the high voltage is cut off by the interlock, the voltage setting is slightly lowered and re-applied, and then the voltage is gradually restored manually.

4

Operation of the 180 L prototype detector

To evaluate the performance of the AXEL detector at the energy around the Q value of ^{136}Xe $0\nu\beta\beta$, measurements with the upgraded 180 L prototype detector were conducted. In this chapter, preparation, the condition, and the procedure of the measurement are described.

4.1 Evacuation of the vessel and introduction and purification of xenon gas

Before introducing xenon gas into the vessel, an evacuation of the air in the pressure vessel is needed. The evacuation was done by the vacuum pump unit described in Sec. 2.3.7. The vessel was purged with 1 bar of argon gas to strike out the remaining gas molecules on the surface of the detector components once one day after and another one week after the start of the evacuation. After the second argon purge, the evacuation was conducted for another one week. The reached vacuum level was measured by a cold cathode gauge (DIAVAC, C-4A), and the outgassing rate was measured by a Pirani gauge (DIAVAC, PSG-1) with the vacuum encapsulation method, i.e., a technique measuring the time increase in pressure by closing the vessel after an evacuation. The vacuum level reached 3.9×10^{-2} Pa and the outgassing rate was 1.23×10^{-4} Pa m^3/s. Figure 4.1 shows the trend of the outgassing rate after the second argon purge. This outgassing rate corresponds to 77.7 ppm/day of impurity for 7.6 bar and 180 L xenon gas. This outgassing rate is not sufficiently low, however, since it would take two or more weeks to lower it by an order of magnitude, and since it can be dealt with by purification, evacuation was terminated here.

After the evacuation, 7.6 bar of natural xenon gas was filled, and the gas was circulated with a flow of 5 NL/min and purified by the molecular sieve and the getter described in Sec. 2.3.7 (Fig. 2.15). The performance of molecular sieves deteriorates with continued use due to the

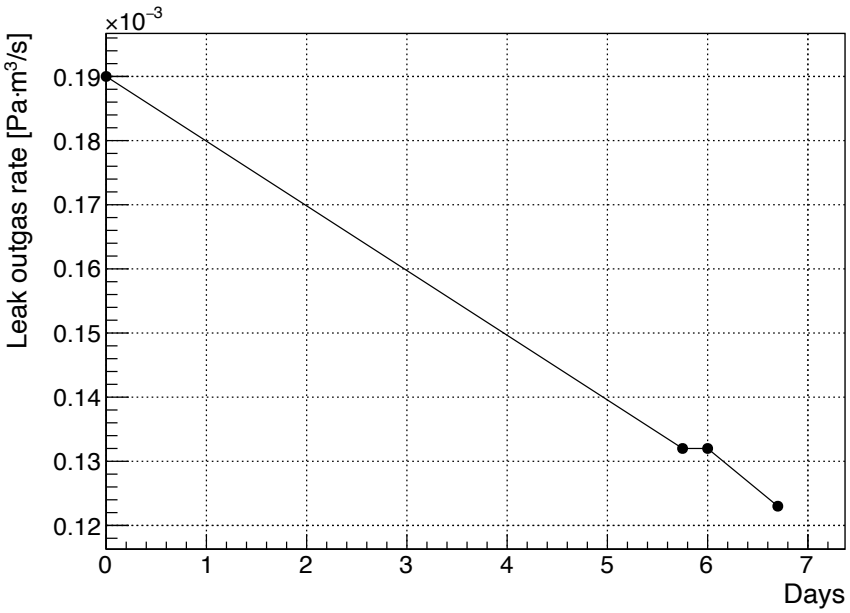

Figure4.1: Trend of the outgassing rate after the second argon purge.

adsorption of impurities. This can be recovered by baking. Figure 4.2 shows the change in the purification capacity of the molecular sieve before and after baking at 120 °C for 6 days. Also this time, baking was performed before the start of purification.

Before starting the measurement, three weeks of purification term was taken while monitoring the improvement of the dew point and EL-light yield. The improvement of the purity in terms of the water concentration during the purification is shown in Fig. 4.3. The measurement was started when the water concentration calculated from the dew point converged to about 0.1 ppm.

4.2 Measurement condition

The intensity of the EL and drift electric fields were set to be 2.5 kV/cm/bar and 83.3 V/cm/bar, respectively. These are lower than the design values of 3 kV/cm/bar and 100 V/cm/bar. This is because frequent discharges stil occurred at ELCC at the design value. The discharges were thought to occur through the boundary of the ELCC cover, across the surface of the polyimide sheet, and down the inner side of the cell to the mesh, at the point where the boundary of the ELCC cover and the cell hole are close. The ratio between the EL and drift field intensity was kept to be 30:1 to maintain 100 % collection efficiency of ionization electrons into the ELCC cells. The applied high voltages were hence −9.5 kV for the anode and −20.9 kV for the cathode (See Figs. 2.1 and 2.2 for the positions of the anode

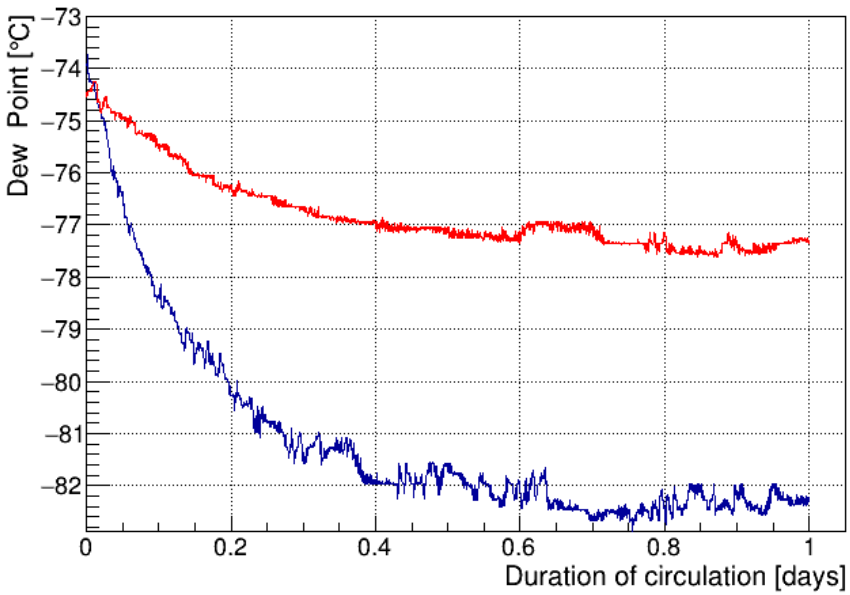

Figure4.2: Change in the purification capacity of the molecular sieve by baking. The red (blue) line corresponds to before (after) the baking.

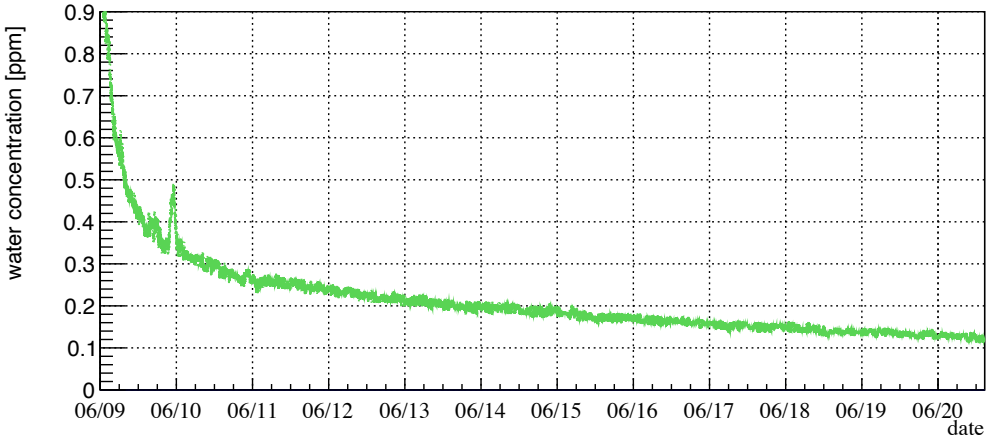

Figure4.3: Improvement of the water concentration during the purification period.

and the cathode electrodes). The measurement conditions are summarized in Table 4.1. At these conditions, discharges happened once per several hours on both the anode and cathode. When a discharge occurs, the interlock system (Sec. 3.5) detects it and cuts off the high voltages.

For this measurement, two kinds of gamma-ray sources were used. One is an ^{88}Y source, which mainly emits gamma rays of 898.0 keV and 1836 keV. The intensity of the source was

Table4.1: Summary of the measurement conditions.

Gas	Natural xenon
Pressure	(7.6 ± 0.1) bar
Anode voltage	(-9.50 ± 0.02) kV
Cathode voltage	(-20.90 ± 0.02) kV
EL field	(2.50 ± 0.05) kV/cm/bar
Drift field	(83.3 ± 0.2) V/cm/bar
Gas temperature	28 °C – 32 °C
Water concentration	0.08 ppm – 0.14 ppm

9 kBq. Another one is a set of thoriated tungsten rods. They are commercial products for welding and include 2 % of thorium by mass. Thus they can be used as a source of thorium series radiations including 2615 keV gamma rays from ^{208}Tl. The amount of used thoriated tungsten rods was 1 kg, resulting in 80 kBq. The source was set on the outside surface of the vessel during the measurement.

4.3 Data taking

Data were taken for five days for ^{88}Y and one day for thoriated tungsten rods in June 2022 with intervals for commissioning and data checking. The data taking with the thoriated tungsten rods was terminated due to the fault of the circulation pump. The anode and cathode voltages, gas pressure, gas temperature, water concentration, etc. were monitored during the data taking. Figure 4.4 shows the trends of important monitor values. The xenon gas pressure was stable at 7.6 bar within roughly 0.1 bar. The gas temperature was in almost rising trend from 28 °C to 32 °C. This is thought to be caused by heat inflow from the circulation pump ($\sim$ 60 °C). The water concentration, as an indicator including other impurities, ranged between 0.08 ppm and 0.14 ppm.

To select fully contained events, the outermost 90 channels out of 672 channels of ELCC were assigned to the veto channels. There was one channel with a high dark current and one dead channel. The high dark-current channel and six channels around the dead channel were also added to the veto channels (See Fig. 4.5).

The threshold of the fiducial trigger (Sec. 2.3.6) was set for the moving average of the sum waveform for 90 samplings (18 µs) to be $\sim$ 1500 ADC counts over the baseline, corresponding around 400 keV. The threshold of the whole trigger (Sec. 2.3.6) was set for the sum waveform to be $\sim$ 15 ADC counts over the baseline, sufficiently low to taking K_α X-rays. The prescale factor for the whole trigger was set to be 1/50.

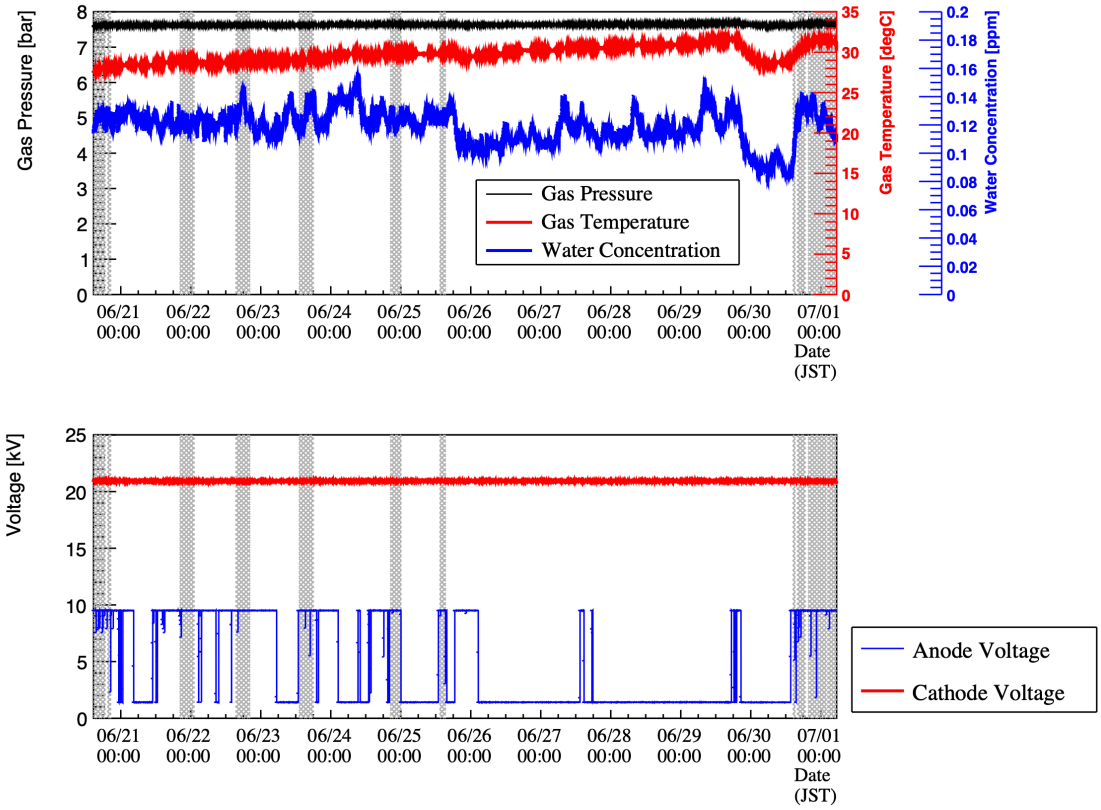

Figure4.4: Trend of the monitor data. The upper panel is for gas conditions, and the lower panel is for high voltages. The gray-shaded areas are data-taking periods. The drop in the anode voltage corresponds to discharges or manual off.

As described in the Sec. 2.3.6, data acquisition of the PMT signal is triggered by the send-header signal from HUL. The waveform recording window is set to 600 µs, and the pre-trigger region is 95 % of the window so that the timing of primary scintillation is certainly included in the window.

The number of total acquired events is 1 145 761 for the ^{88}Y run and 869 422 for the thoriated tungsten rod run. The whole dataset was used to evaluate the detector performance.

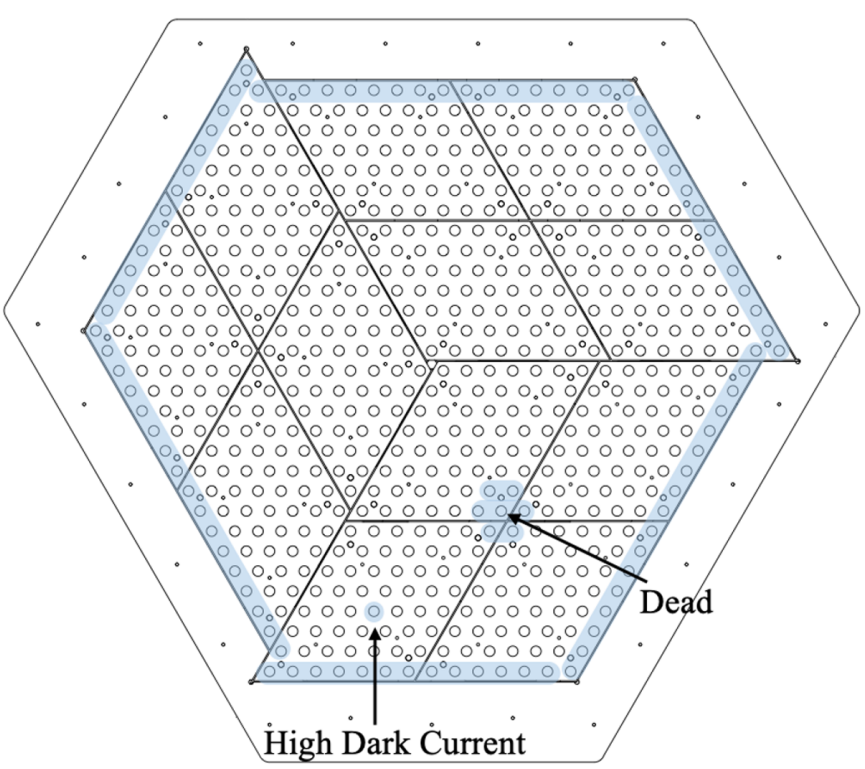

Figure4.5: Configuration of veto channels. The blue-shaded channels were assigned to veto.

5

Analysis

The signal generation process of the AXEL detector is illustrated in Fig. 5.1. The ELCC detects the ionization electrons through the EL process. The EL photons are detected by the MPPCs, so the energy deposit is derived from the MPPC output. Defining the drift direction as the z-axis, the spatial pattern of the energy deposit is reconstructed from the hit pattern in each channel (xy-direction) and the timing information (z-direction). The PMTs detect

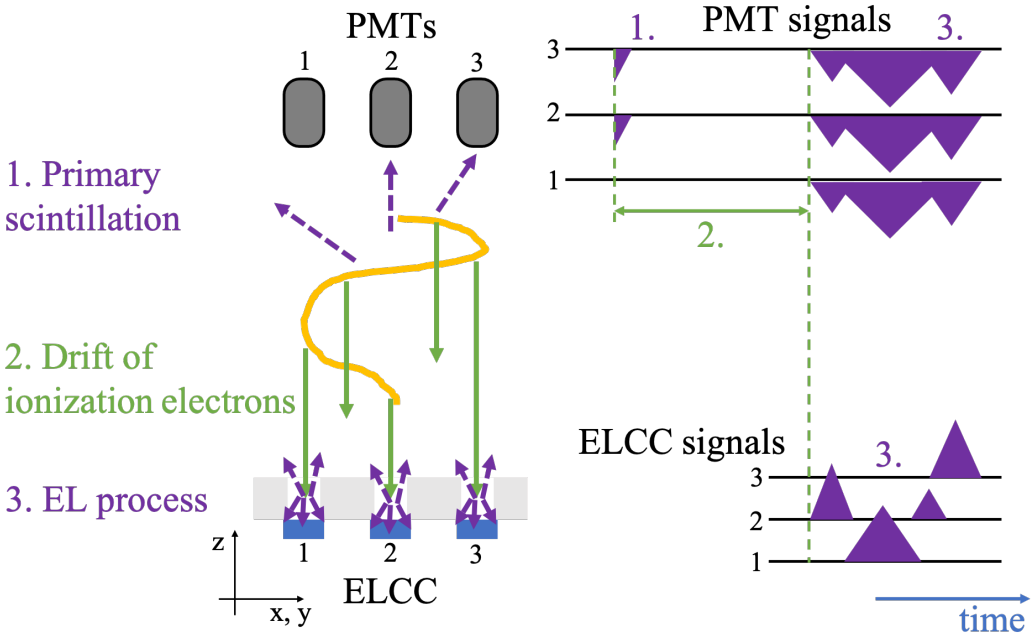

Figure5.1: Schematic illustration of signal generation. The primary scintillation occurs and is detected by PMTs. After the drift of the ionization electrons, the EL process occurs in the ELCC cells and the EL lights are detected both by the MPPC of each ELCC cell and by the PMTs.

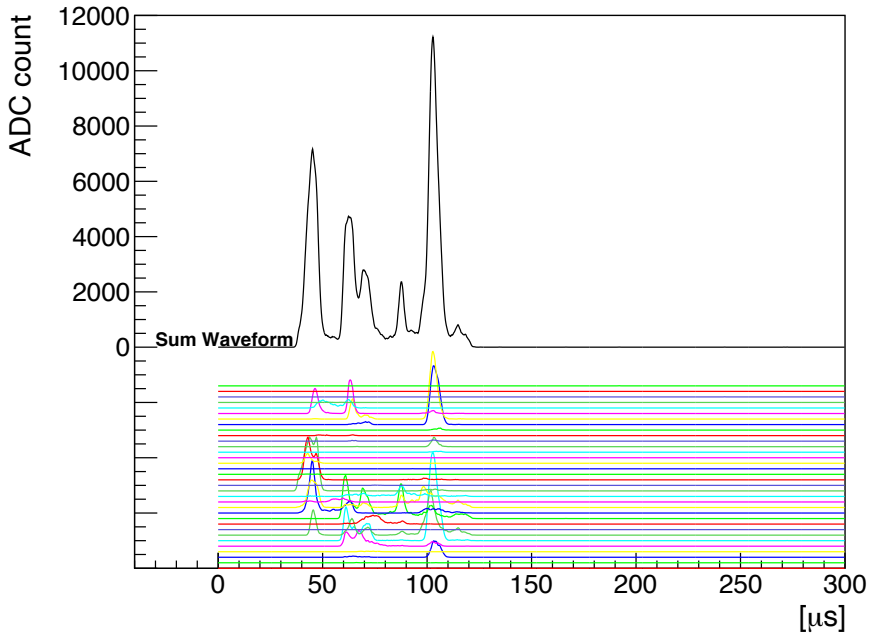

Figure5.2: Typical waveforms of the ELCC signal. The waveform of each channel is drawn in colored lines with arbitrary offsets. The sum of the waveforms is drawn in the black line.

both the primary scintillation and EL light in ELCC. The absolute z-position of the event is derived from the time interval of these two signals divided by the drift velocity.

The analysis process is composed of three steps. The first is the ELCC waveform analysis (Sec. 5.1), which consists of the search for hits, clustering, correction to the non-linearity of MPPCs, and correction to the gain of the EL process in each ELCC cell. The second is the PMT waveform analysis (Sec. 5.2), which consists of the search for PMT hits, identification of the primary scintillation, and matching to the ELCC events. The last step is overall cuts and corrections (Sec. 5.3).

The same analysis method was used for both the ^{88}Y run and the thoriated tungsten rod run (hereafter, thorium run), however, the correction coefficients are different for each run.

5.1 ELCC waveform analysis

Figure 5.2 shows typical waveforms of the ELCC signal, i.e. the MPPC output. Since the ionization electrons are spatially distributed, they leave hits in multiple channels. Both the waveform of each channel and the summed waveform are depicted in Fig. 5.2.

5.1.1 Hit search and clustering

The baseline of the waveform of each channel is calculated as a mean of ADC counts of the last 200 samplings (40 µs) of the data-taking window since there are no hits in this region for most of the events.

Hits are searched for a threshold of 3.5 ADC counts above the baseline, which corresponds to 3.8 photons/0.2 µs equivalent. This threshold is determined from the noise level, mostly one ADC count and occasionally two ADC counts from the baseline. It is sufficiently low to detect all incident ionization electrons since the average number of detected photons per ionization electron is 12.5 (See Sec. 5.1.3).

The rising edge and the falling edge of the waveform is defined to be the rise timing and the fall timing of a hit. The rise timing and the fall timing of a hit are defined as the threshold-crossing timing. From the five samplings before the rise timing to the five samplings after the fall timing, the ADC counts of the waveform are summed up, and the sum is converted to the photon count by using the gain of the channel's MPPC. The gains are pre-calculated using the MPPC's dark current pulses, as described in Sec. 2.3.3.

A single cluster is defined as a consecutive energy deposit in three-dimensional space. As noted in Sec. 1.5.1, photoelectric absorption events are typically single-clustered and Compton scattering events are typically multiple-clustered. The typical size of the cluster is, for example in the case of 1000 keV cluster, $\sim$ 30 channels of ELCC and $\sim$ 50 µs in the time width. Hits that are in adjacent channels and overlapped in time are identified as belonging to the same single cluster. All hits in an event are assigned to one of the clusters according to this way.

Events are removed from further analysis if ADCs overflow, the rise timing is less than 20 samplings (4 µs) or the fall timing is over 1300 samplings (260 µs), to ensure the entire hit is contained within the data-taking window (1500 samplings, 300 µs), and the hit is not overlapped in the region for baseline calculation.

5.1.2 MPPC non-linearity correction

As described in Sec. 2.3.3, MPPCs have a non-linear output for high incident light intensity. To acquire the incident number of photons and obtain better energy resolution, this non-linearity has to be corrected. The correction is done by the following equation:

$$N_{\mathrm{corrected}} = \frac{N_{\mathrm{observed}}}{1 - \frac{\tau}{\Delta t \cdot N_{\mathrm{pixel}}} N_{\mathrm{observed}}} \ , \tag{5.1}$$

where N_{observed} and $N_{\mathrm{corrected}}$ are the photon counts before and after the correction respectively, τ is the recovery time, Δt is the time width applying this correction, 200 ns in this

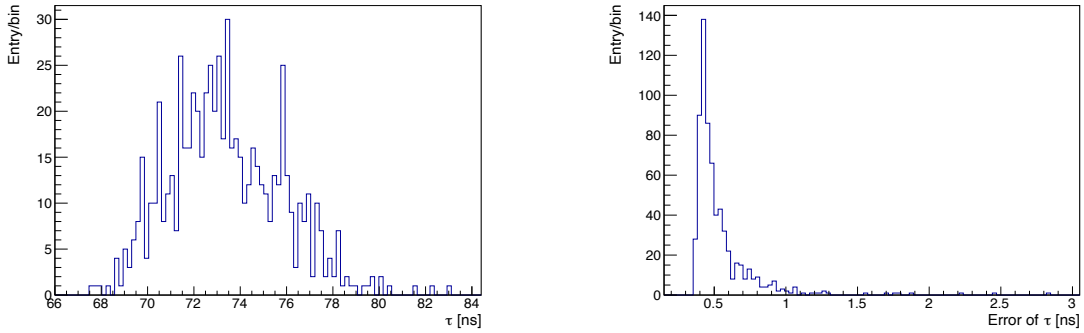

(a) (b)

Figure5.3: Distribution of the measured recovery times of MPPCs (a) and their measurement errors (b).

analysis corresponding to the sampling speed of the FEBs, and $N_{\mathrm{pixel}} = 3600$, the number of pixels. This is the form in which Eq. 2.2 is solved for N_{true}.

The recovery times of each MPPC were measured in advance by measuring the responses to the high-intensity LED light. To monitor the true number of photons incident to MPPCs, one MPPC with a 5%-ND filter attached was used as a reference. Figure 5.3a shows the distribution of the measured recovery times and Fig. 5.3b is the distribution of their measurement errors. The mean of the measured recovery times is 73.4 ns, and the mean of the measurement error is 0.53 ns.

5.1.3 EL gain correction

The gain of the EL process in each ELCC cell (hereafter, EL gain) is defined as the mean of detected photon count when one ionization electron enters the cell. The EL gains are different channel by channel due to dimensional differences by machining accuracy, differences in the photon detection efficiency of MPPCs, and so on. The distribution of the EL gains is shown in Fig. 5.4a. Thus, each signal should be corrected using its gain relative to the mean over channels to obtain better energy resolution.

The correction factors are determined by using the peak of K_α characteristic X-rays in the photon count spectra. The K_α X-ray signal spreads over several channels due to diffusion, so photon count spectrum of the clusters in which the target channel has the highest photon counts is used. The correction factor for the target channel is derived from the ratio of the K_α peak of this spectrum to that of the spectrum by the whole channels. Throughout this procedure, the correction factors of the adjacent channels affect the determination of the correction factor of the channel. Hence this procedure is applied to all channels and iterated

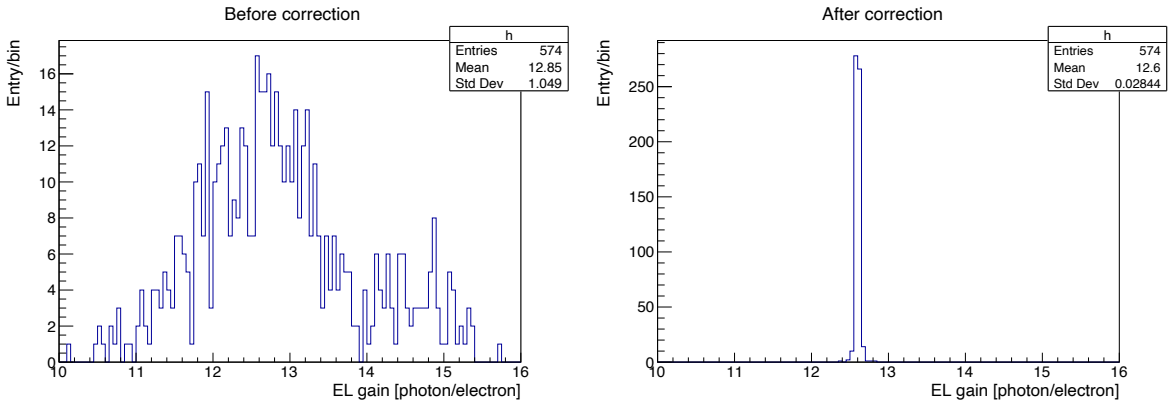

(a) (b)

Figure5.4: Distribution of the EL gains before (a) and after (b) the correction for the channels other than the veto channels.

multiple times until the factors converge: in this analysis, six times. The distribution of the EL gains after six times of corrections is shown in Fig. 5.4b. The mean of the EL gains is 12.6 photon/electron for this measurement. This is slightly higher than the EL gain expected by simulation (See Fig. 2.6b). This is considered to be because of the uncertainties in the simulation conditions, for example, the reflectance of the PTFE.

5.2 PMT waveform analysis

Figure 5.5 shows typical signal waveforms of the PMTs. Very narrow hits coinciding in two PMTs and preceding the EL signals are the primary scintillation photon candidates. In addition to the PMT waveforms, the send-trigger signal from HUL is also recorded in one channel for timing matching between the ELCC signals, as noted in Sec. 4.3.

5.2.1 Hit search and identification of hits by the primary scintillation

The baseline of the waveform of each channel is calculated as a mean of ADC counts of the first 1000 samplings (10 µs) of the data-taking window since there are no hits in this region for most of the events. The hit threshold is set at 200 ADC counts below the baseline. It is sufficiently higher than noise and lower than 1 p.e. wave height. To separate hits by scintillation light from hits by EL lights, hits are selected when they have a width less than 400 ns and are more than 1 µs apart from other hits. Hereafter, hits selected by this criterion are called scintillation-like hits, and the others are called EL-like hits. Of these scintillation-like hits, those that are coincident within 100 ns in two or more channels are reconstructed as

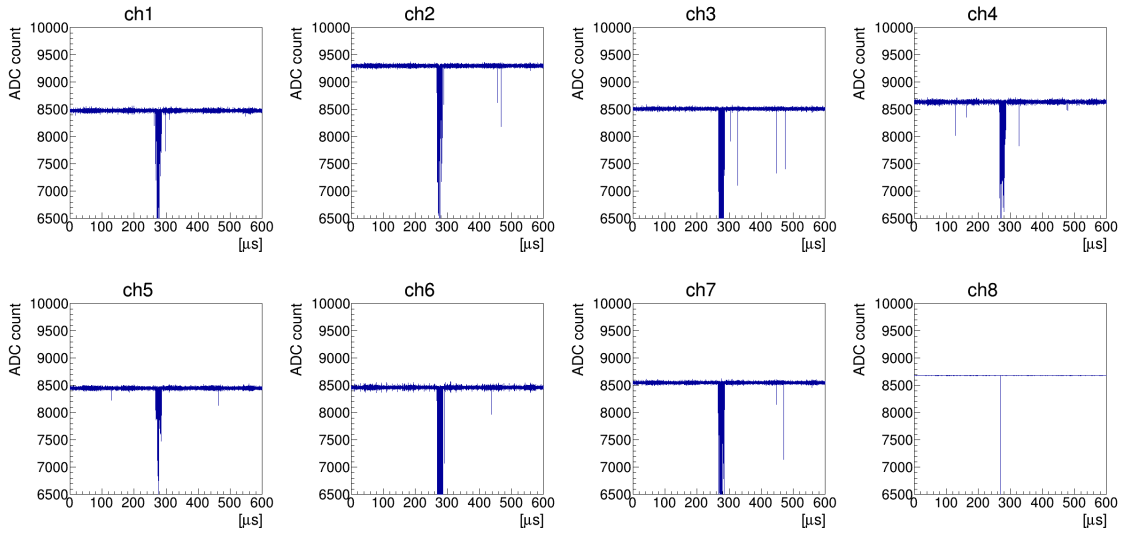

Figure5.5: Typical waveforms of the PMTs. The hits at ∼130 µs in channel 4 and channel 5 are the scintillation signals. The hits at around 300 µs are EL from ELCC. Channel 8 records the send-trigger signal from HUL as mentioned in Sec. 4.3, not the PMT signal.

a hit cluster by the primary scintillation light. For example, in Fig 5.5, the hits at ∼130 µs in channel 4 and channel 5 are coincident, and reconstructed as a hit cluster by the primary scintillation light. The events with only one reconstructed hit cluster are selected for the further analysis. In case there are two or more hit clusters, such events are cut because it is not possible to determine which hit cluster is the actual primary scintillation. The distribution of the number of hit clusters is shown in Fig. 6.8 for 1836 keV events.

5.2.2 Matching of ELCC and PMT events and reconstruction of z-position

The corresponding ELCC event and PMT event are matched based on the event time information by the timestamp and the internal clock of the ELCC FEBs and the PMT digitizer. For matched events, the time interval between the primary scintillation and the ELCC hits is calculated. To match the time axes of the ELCC signal waveform and PMT signal waveform, the send-trigger signal from HUL (Fig. 5.5 bottom right) which corresponds to the fixed timing in the data acquisition window for ELCC is used. Figure 5.6 shows the distribution of the time intervals between the primary scintillation and the fall timing of ELCC signal. Since all of the events crossing the cathode mesh electrode have the fall timing of EL signal corresponding to the position of the cathode mesh, such events make a peak in this distribution. The peak corresponds to the cathode plane of the field cage: in other words, $z = 18$ cm. From this, the drift velocity of ionization electrons is derived to be 1.04 mm/µs. Using this drift velocity, the

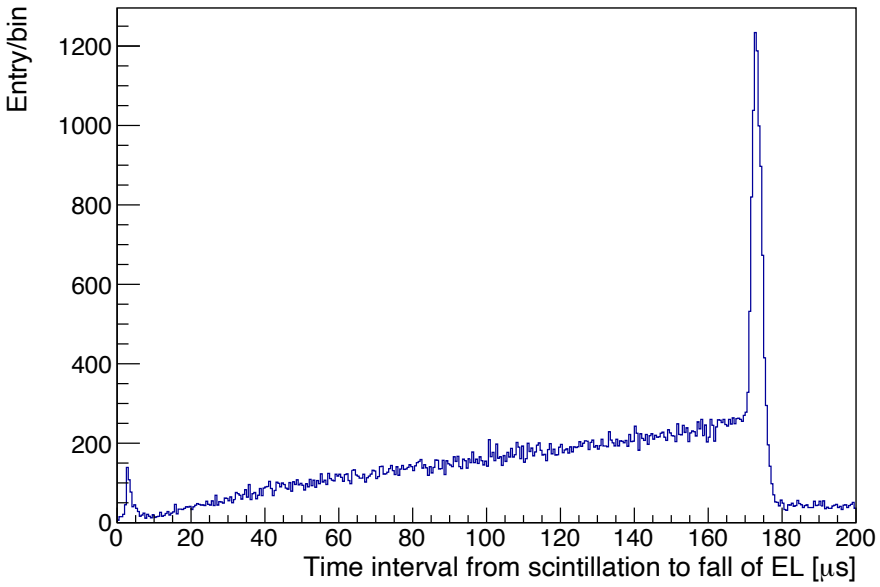

Figure5.6: Distribution of the time intervals between scintillation and the fall timing of ELCC signals. The peak at 175 µs is formed by the events across the cathode plane.

z-position of each ionization signal detected by ELCC is reconstructed.

5.2.3 Selections to avoid timing mismatch or z mis-reconstruction

For typical events, the z-positions of the events are determined without ambiguity by following the above method, but not for some events. To ensure that only events in which the z-positions are correctly reconstructed are retained for subsequent analysis, the following three selections are applied.

First, there are some events in which multiple send-trigger signals are accidentally detected. Such events are removed because it leads to a timing mismatch depending on which one corresponds to the true beginning of the ELCC events.

Second, there are events with EL-like hits existing in the region where the scintillation hit is expected. Since an EL-like hit is a set of narrow hits, a part of the EL-like hits in such events can be misidentified as a scintillation-like hit. Fig. 5.7 shows a typical PMT waveform of such an event. Such cases can occur if the buffer of the FEB is full and the FEB misses the former EL waveform. Therefore events in which EL-like hits exist in the region corresponding to within 18 cm from the rising edge of the ELCC waveform are removed.

Finally, there is a possible case in which scintillation from the region not sensitive to the ELCC is accidentally detected by the PMTs. These cases lead to the mis-reconstruction of the

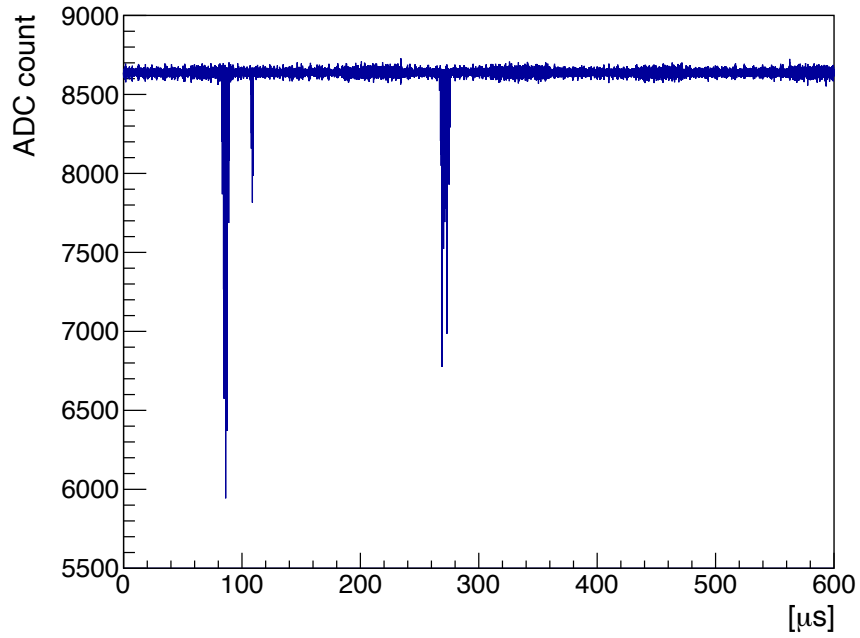

Figure5.7: Example of the PMT wavform of the events to be cut. There are EL-like hits at $\sim 100\,\mu s$ instead of scintillation-like hits.

z-position when the wrong hit cluster is used. To prevent as much deterioration of the energy resolution as possible due to mis-reconstructions of z-position, events in which scintillation-like hits exist in the region corresponding to within 2 cm from the rising edge of the ELCC waveform are cut. The schematic drawing of an example of a cut event is shown in Fig. 5.8. The reason for the 2 cm criterion is that ionization electrons generated within 2 cm from the ELCC surface are not guaranteed to be collected into the ELCC [49]. The energy resolution would be worse for events which deposit energy within 2 cm from the ELCC surface.

The effect of the mis-reconstructions of z-position on the energy resolution is discussed in Sec. 7.1.4, and the possible improvement to reduce mis-reconstructions is proposed in Sec. 7.3.

5.3 Fiducial volume cuts and overall corrections

Using the information obtained from the ELCC and PMT signal analysis, fiducial volume cut and overall corrections are applied.

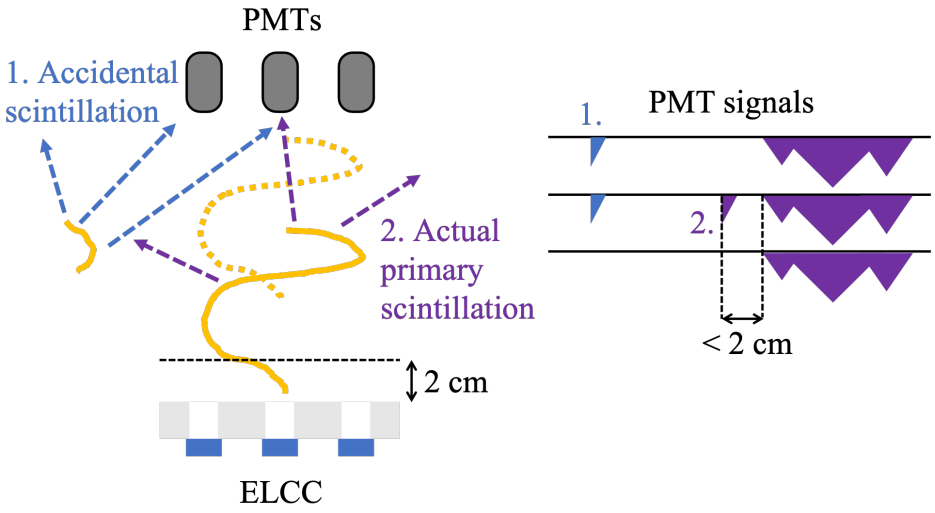

Figure5.8: Schematic example of an event that should be cut because of the mis-reconstruction of the z-position. Scintillation photons by an accidental event out of the sensitive volume of the ELCC hit two or more PMTs (1). The actual primary scintillation photons corresponding to the energy deposit within 2 cm above the ELCC only hit one PMT (2). The z-position is mis-reconstructed as the dotted curve.

5.3.1 Elimination of clusters with small photon counts

Many events contain a few to several tens of clusters with photon counts less than one hundred. These clusters are generated from one to a few electrons considering the average EL gain of 12.6. Figure 5.9 shows the distribution of the photon counts and the drift distance from the leadign edge, rising, of the ELCC signal for these small photon-count clusters. The dense region around 180 mm, which corresponds to the length of the drift region, is considered to be clusters by electrons generated by VUV EL-light hitting the cathode mesh. The other clusters can be formed in the same manner with various detector components and also by the ionization electrons that attach to impurities in the gas during drift and are released after a while. Such a phenomenon is also observed in liquid xenon detectors [60–62].

If such clusters with small photon counts are included in the event, the fiducial cut is applied more severely than it should be. Also, the number of clusters is greater than it should be. Therefore clusters with less than 100 photons are eliminated from events. The total photon counts of eliminated clusters in a event are 400 photons at maximum. Thus the effect on the reconstruction of energy is less than 0.04% for the 1836 keV photopeak and negligible compared to the energy resolution.

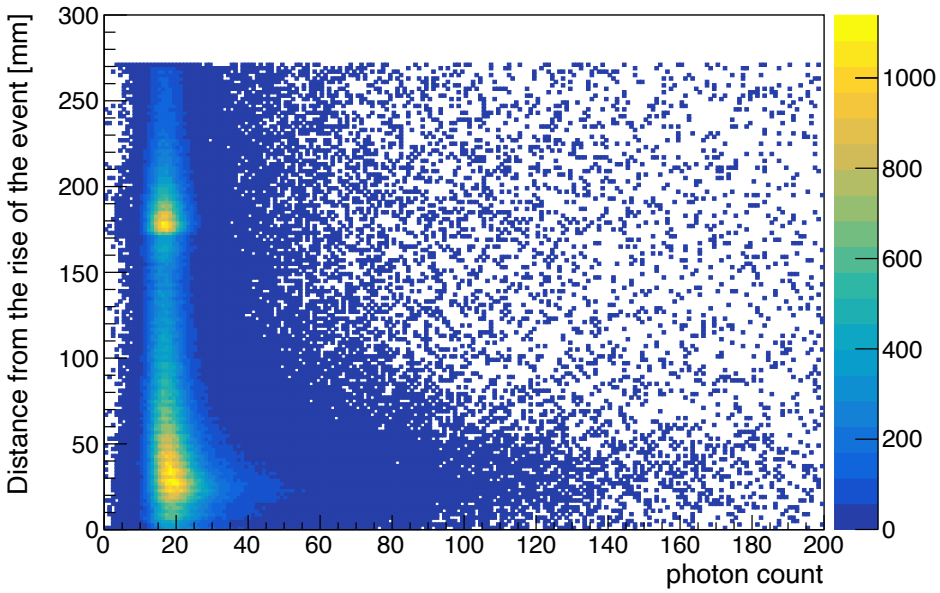

Figure5.9: Drift distance from the rising, leading edge, of the event and photon counts of the small photon-count clusters.

5.3.2 Fiducial volume cut

The fiducial channel of the ELCC is defined to be the channels other than the veto channels defined as described in Sec. 4.3. The fiducial volume is defined as the volume above the fiducial channels and the z-position of 2 cm to 17.5 cm. The reason for the lower edge of 2 cm is the same as described in Sec. 5.2.3, and the upper edge of 17.5 cm is to fully reject the events crossing the cathode electrode, $z = 18$ cm. Events fully contained in the fiducial volume are selected for further analysis, i.e. rejecting events that have any hits on veto channels and events whose z-position extends beyond the $2\,\text{cm} < z < 17.5\,\text{cm}$ region.

5.3.3 Correction of time variation

Figure 5.10 shows the time variation of photon counts of clusters around the K_α energy. The cause of variation can be changes in the gas conditions: temperature, density, and purity. The correction factors are derived for divisions every 30 minutes as the ratio of the K_α peak of the time division to the K_α peak for the whole time. The width of the time bin, 30 minutes, is determined so that the width of the peak of 1836 keV is minimized; balanced between the statistical error of the correction factor and the sensitivity to the time variation. The correction factor of each time bin is determined with the accuracy of 0.137 % in average.

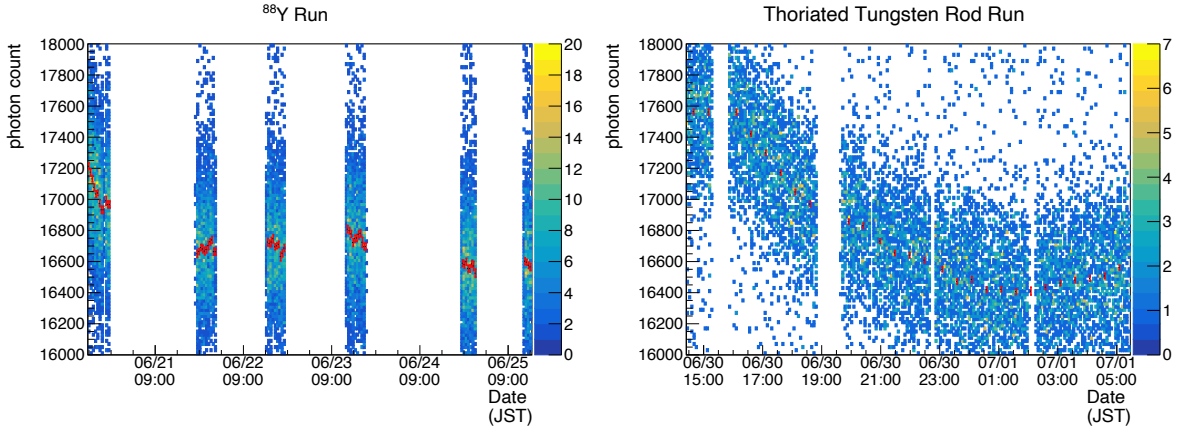

Figure5.10: Variation of photon counts with time. The red points with the error bar represent the K_α peak in each time division. The left panel is for the ^{88}Y run and the right is for the thorium run.

5.3.4 Correction of z-dependence

Some amount of the ionization electrons are not detected because of the attachment by impurities during drift. This attenuation is characterized by the following equation.

$$N(z) = N_0 \exp\left(-\frac{z}{\lambda}\right) \simeq N_0 \left(1 - \frac{z}{\lambda}\right) \text{ if } z \ll \lambda \ , \tag{5.2}$$

where N_0 and $N(z)$ are the photon counts before and after the attachment respectively and λ is the attenuation length of the ionization electrons. Figure 5.11 shows the dependence of the photon counts of K_α clusters on the z-position. From this dependence, the attenuation lengths of $\lambda = (21\,700 \pm 3700)$ mm for the ^{88}Y run and $\lambda = (17\,000 \pm 2700)$ mm for the thorium run were obtained. These correspond to the electron lifetimes of (20.9 ± 3.6) ms and (16.3 ± 2.6) ms respectively. Using these attenuation lengths, the photon counts are corrected for every sampling of the waveforms.

5.3.5 Overall fine-tuning for the recovery times of MPPCs

As described in Sec. 5.1.2, the non-linearity of the MPPCs is corrected using the recovery times of MPPCs measured in advance. However, the effective recovery times can vary depending on the conditions of the MPPCs, such as temperature, or shadow of the mesh electrode in front of MPPCs. The deviation in photon counts due to the difference between the true

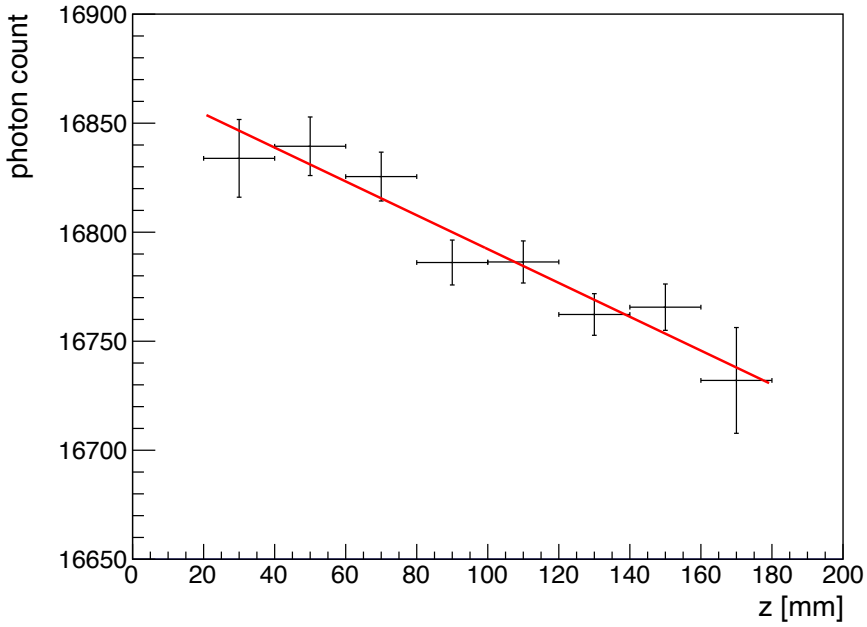

Figure5.11: Dependence of the photon counts of K_α clusters on the z-position for the ^{88}Y run. The red line shows the fitted function.

effective recovery time and the measured recovery time can be expressed as follows.

$$\sum_i r^i N^i_{\rm rec} - N_{\rm true} = \sum_i \frac{r^i N^i_{\rm obs}}{1 - k' N^i_{\rm obs}} - N_{\rm true} \simeq \Delta k \sum_i r^i \left(N^i_{\rm rec}\right)^2, \tag{5.3}$$

where $N_{\rm true}$ is the true total photon count of the event, i runs for every sampling of the waveform of every hit channel, $N^i_{\rm obs}$ and $N^i_{\rm rec}$ are the photon count for each sampling of the waveform before and after the MPPC non-linearity correction, respectively, r^i is the correction factor other than the MPPC non-linearity, $k^{(\prime)} = \tau^{(\prime)} / \left(\Delta t \cdot N_{\rm pixel}\right)$, $\tau^{(\prime)}$ is the true (measured) recovery time of the channel, and $\Delta k = k - k'$. The last line assumes that Δk is small and common among channels. This equation indicates that, if there exists an overall bias in the recovery times, it appears as a slope of the relation between the photon counts and $\sum_i r^i \left(N^i_{\rm rec}\right)^2$ (defined as corrected squared sum, CSS).

Figure 5.12 shows the distribution of the photon counts and the CSS. To determine the Δk and corresponding biases of the MPPC recovery times, the peaks with high statistics are used; the photopeak of 898 keV gamma rays and the double escape peak of 1836 keV gamma rays for the ^{88}Y run, and the photopeak of 583 keV gamma rays and the double escape peak of 2615 keV gamma rays for the thorium run. From the slope at each peak of the photon counts,

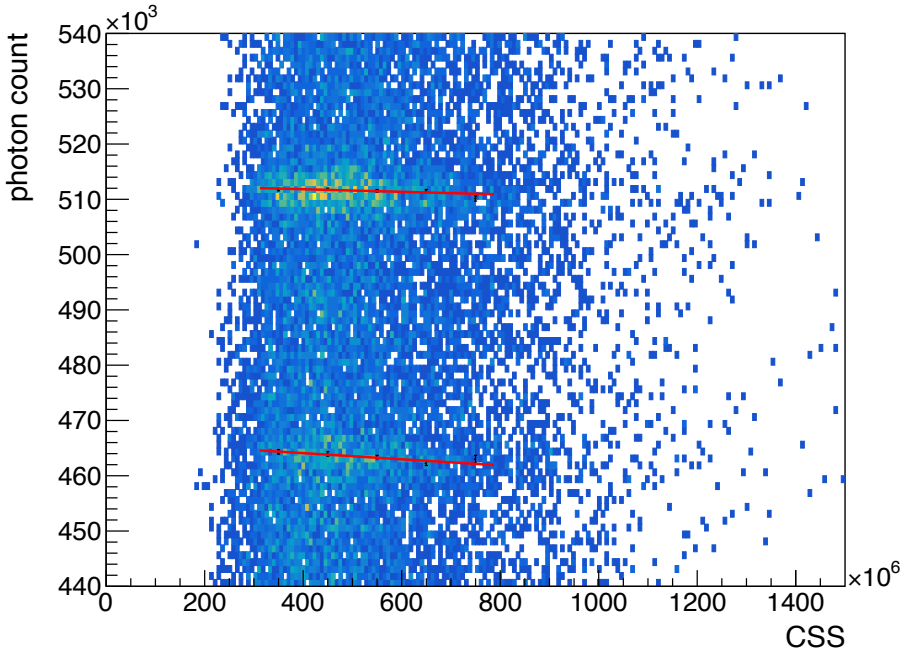

Figure5.12: Relation between the photon counts and the CSS for the photopeak of 898 keV gamma rays ($\sim 5.1 \times 10^5$ photon) and the double escape peak of 1836 keV gamma rays ($\sim 4.6 \times 10^5$ photon) in the ^{88}Y run.

the biases for the MPPC recovery times were derived as +2.35 ns for the ^{88}Y run and +3.13 ns for the thorium run.

The MPPC non-linearity correction, EL gain correction, time variation correction, and z dependence correction are repeated with the recovery times shifted by these biases.

6

Results

From the analysis in the previous chapter, EL photon count and track of events are obtained. Based on these, the performance of the detector is evaluated.

6.1 Linearity and Energy resolution

Figure 6.1 is the EL photon-count spectra of each run. Several peaks are identified in the spectra; peaks of characteristic X-rays of xenon, full peaks of gamma rays from the sources and environment, and double escape peaks of pair creation. Each peak was fitted assuming a Gaussian peak and linear background. For the gamma-ray full peaks, single-clustered events and multi-clustered events were fitted separately. Figure 6.2 shows an example of the fit results, and Table 6.1 is the summary. A good energy resolution of $(0.73 \pm 0.11)\,\%$ is achieved for 1836 keV single-clustered events. The energy resolutions for the other peaks are also good,

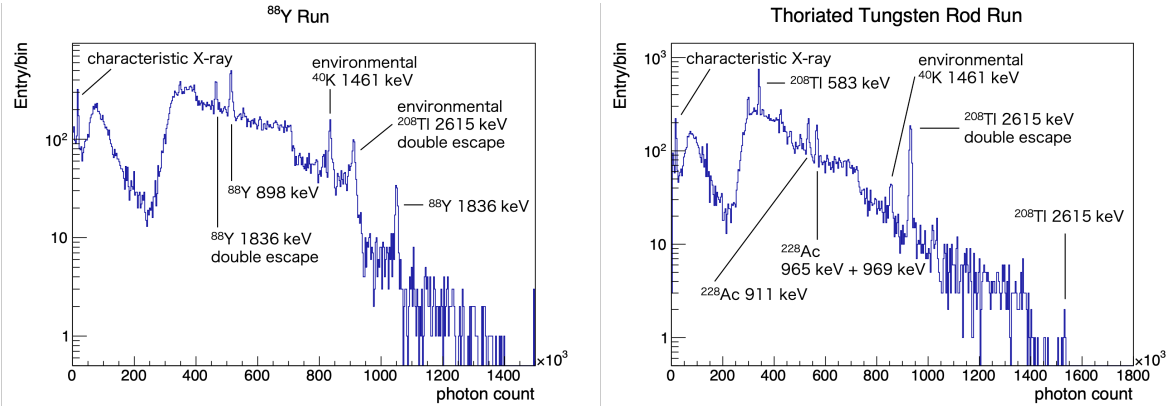

Figure6.1: Photon count spectra after all of the corrections and cuts. The left panel is for the ^{88}Y run and the right is for the thorium run. The dip around 200 photon count corresponds to the threshold of the fiducial trigger.

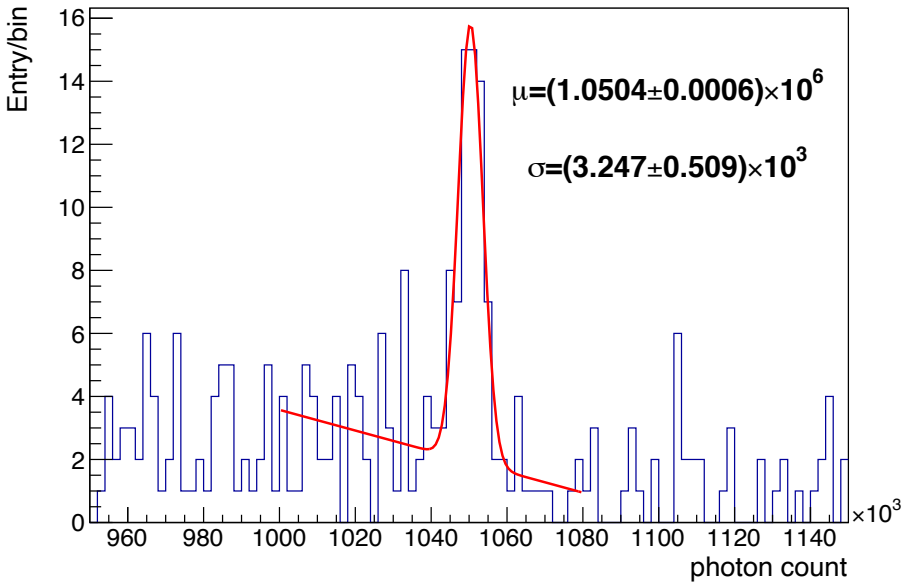

Figure6.2: Result of the fit to the spectrum of the single-clustered full energy peak of ^{88}Y 1836 keV gamma ray events.

though multiple-clustered events have slightly worse energy resolutions for most cases. Possible reasons for these worese energy resolutions for the multiple-clustered events are discussed in Sec. 7.2.

To evaluate the energy resolution at the Q value, extrapolation is needed. Before conducting the extrapolation, the linearity of the photon counts versus the energies is confirmed. Figures 6.3a and 6.3b show the mean photon counts of each peak versus the energy from a database. [18]. The ratio of the data point to the fitted proportional line is shown in Figs. 6.3c and 6.3d. Linearity is good except that the K_α and K_β peaks are below the fitted line.

By extrapolating these results, the energy resolution at the Q value of ^{136}Xe $0\nu\beta\beta$, 2458 keV, is estimated. Two cases are considered for the dependence on E; $a\sqrt{E}$ and $a\sqrt{E+bE^2}$. The former is for a situation dominated by statistical fluctuation, and the latter is with systematics contributing. The data points of single-clustered gamma-ray peaks are fitted by these two functions. Fit results are summarized in Table 6.2, and Fig. 6.4 shows the results of the extrapolation to the Q value. The estimated energy resolution at the Q value is $(0.60 \pm 0.03)\,\%$ for the form of $a\sqrt{E}$ and $(0.70 \pm 0.21)\,\%$ for the form of $a\sqrt{E+bE^2}$. As shown in Table 6.2, the coefficient b for the form of $a\sqrt{E+bE^2}$ is zero-consistent, and the extrapolated energy resolution at the Q value is consistent within the error between the form of $a\sqrt{E}$ and $a\sqrt{E+bE^2}$. Thus it can be said that the effect of systematic term linearly depending on E is sufficiently small, and the energy resolutions are dominated by statistical

Table6.1: Summary of the result of peak fit. SS stands for the single-site events and MS stands for the multiple-site events for gamma-ray full peaks. ^{40}K multi-cluster events in the thorium run were too few to evaluate the resolution.

	Energy	mean photon counts	resolution [FWHM]
^{88}Y run			
K_α	29.68 keV	$(1.6870 \pm 0.0004) \times 10^4$	(4.389 ± 0.050) %
K_β	33.62 keV	$(1.9166 \pm 0.0011) \times 10^4$	(4.722 ± 0.125) %
Double escape of ^{88}Y 1836 keV	814.1 keV	$(4.6512 \pm 0.0022) \times 10^5$	(1.194 ± 0.102) %
^{88}Y SS	898.0 keV	$(5.1374 \pm 0.0022) \times 10^5$	(1.152 ± 0.119) %
^{88}Y MS			(1.386 ± 0.109) %
environmental ^{40}K SS	1461 keV	$(8.3458 \pm 0.0042) \times 10^5$	(0.81 ± 0.11) %
environmental ^{40}K MS			(1.09 ± 0.16) %
^{88}Y SS	1836 keV	$(1.0504 \pm 0.0006) \times 10^6$	(0.73 ± 0.11) %
^{88}Y MS			(0.98 ± 0.19) %
thorium run			
K_α	29.68 keV	$(1.7270 \pm 0.0005) \times 10^4$	(4.107 ± 0.053) %
K_β	33.62 keV	$(1.9604 \pm 0.0013) \times 10^4$	(5.003 ± 0.155) %
positron annihilation SS	511.0 keV	$(2.9889 \pm 0.0022) \times 10^5$	(1.221 ± 0.182) %
positron annihilation MS			(1.541 ± 0.362) %
^{208}Tl SS	583.2 keV	$(3.4115 \pm 0.0012) \times 10^5$	(1.152 ± 0.078) %
^{208}Tl MS			(1.32 ± 0.13) %
^{228}Ac SS	911.2 keV	$(5.3298 \pm 0.0049) \times 10^5$	(1.46 ± 0.23) %
^{228}Ac MS			(1.17 ± 0.19) %
environmental ^{40}K SS	1461 keV	$(8.5596 \pm 0.0077) \times 10^5$	(0.65 ± 0.22) %
Double escape of ^{208}Tl 2615 keV	1593 keV	$(9.3178 \pm 0.0020) \times 10^5$	(0.940 ± 0.044) %

factors. The achieved energy resolution at the Q value is the best ever among the $0\nu\beta\beta$ search experiments using xenon.

6.2 Track reconstruction

The track images of events are successfully reconstructed. Figures 6.5 and 6.6 are typical reconstructed track images of a 2615 keV event and a 1593 keV event. The former is consistent with a photoelectric absorption of a 2615 keV gamma ray from ^{208}Tl. The latter is considered to be a double escape of a 2615 keV pair creation. A dense energy deposit at the end of the track ("blob") is confirmed in Fig. 6.5. In Fig. 6.6, two blobs can be seen corresponding to the

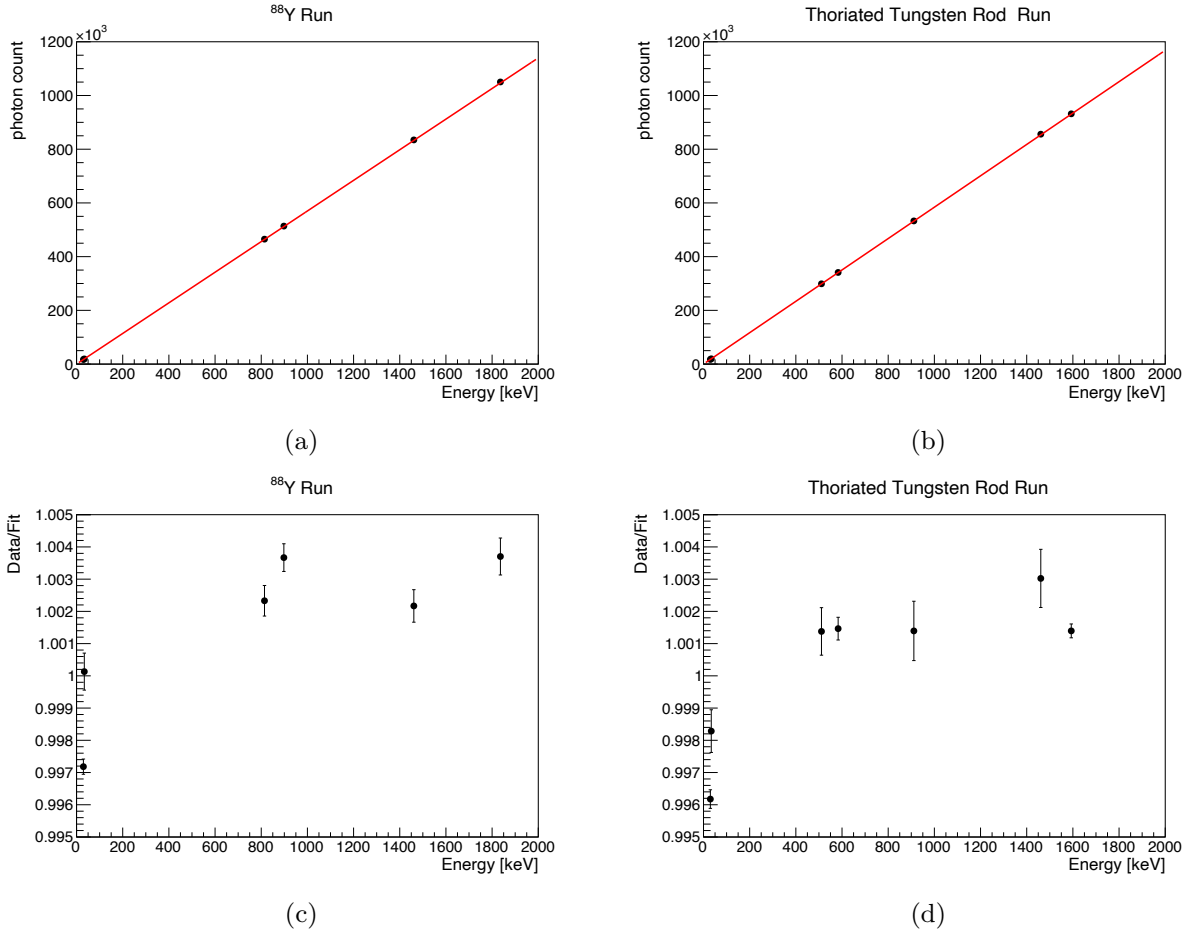

Figure6.3: Relation between the photon counts and the corresponding energies. The lines are the fit results as proportional ((a) and (b)). The ratio of the data point to the fit ((c) and (d)).

Table6.2: Summary of the fitted functions to the energy resolutions.

Function	a	b	Extrapolated FWHM energy resolution at the Q value
$a\sqrt{E}$	$(2.99 \pm 0.13) \times 10^{-1}$	–	$(0.60 \pm 0.03)\,\%$
$a\sqrt{E + bE^2}$	$(2.70 \pm 0.35) \times 10^{-1}$	$(2.73 \pm 3.58) \times 10^{-4}$	$(0.70 \pm 0.21)\,\%$

endpoints of the electron and the positron. The number of blobs will be a key to distinguishing the $0\nu\beta\beta$ signals from the gamma-ray backgrounds as noted in Sec. 1.5.2.

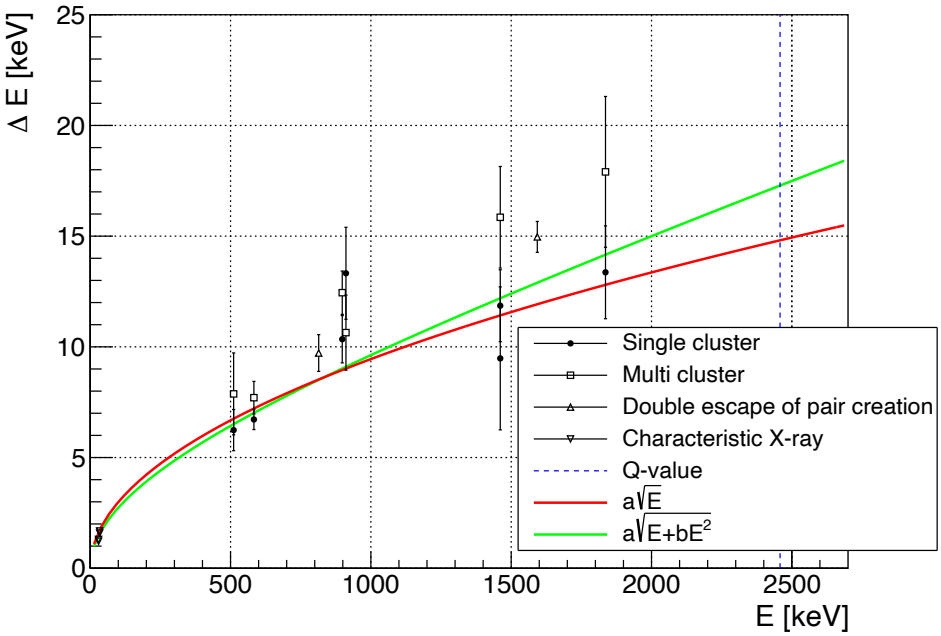

Figure6.4: Extrapolation of the FWHM energy resolution to the Q value of ^{136}Xe $0\nu\beta\beta$ with two kinds of the fit function, $a\sqrt{E}$ and $a\sqrt{E+bE^2}$. Only the single-cluster gamma-ray data points (solid circle) were used for the fit.

6.3 Drift velocity and diffusion

In the development of the algorithm to distinguish signals from backgrounds based on track images, the properties of track images should be understood and reproduced in the simulation dataset. For this purpose, the drift velocity and the diffusion of the tracks is evaluated in this section.

As described in Sec. 5.2.2, the drift velocity of ionization electrons is 1.04 mm/µs in this measurement. This is consistent with the expectation of 1.05 mm/µs calculated by Magboltz.

To evaluate the diffusion of the tracks, the K_α clusters, whose track length is about 0.8 mm and much smaller than the spread by diffusion, are used. They are selected for every 1 cm interval in the z-direction and overlaid with respect to each center position to obtain averaged hit distributions. The standard deviations of the distribution in the x, y, and z directions are plotted as a function of the z-position in Fig. 6.7. They are fitted by the form of $\sqrt{{p_0}^2 z + {p_1}^2}$, where the fit parameter p_0 corresponds to the diffusion of ionization electrons during drift and the parameter p_1 corresponds to the offset term, for example, by the pixelization at ELCC for the transverse direction, and by the Sallen-Key filter in AxFEB and finite time of

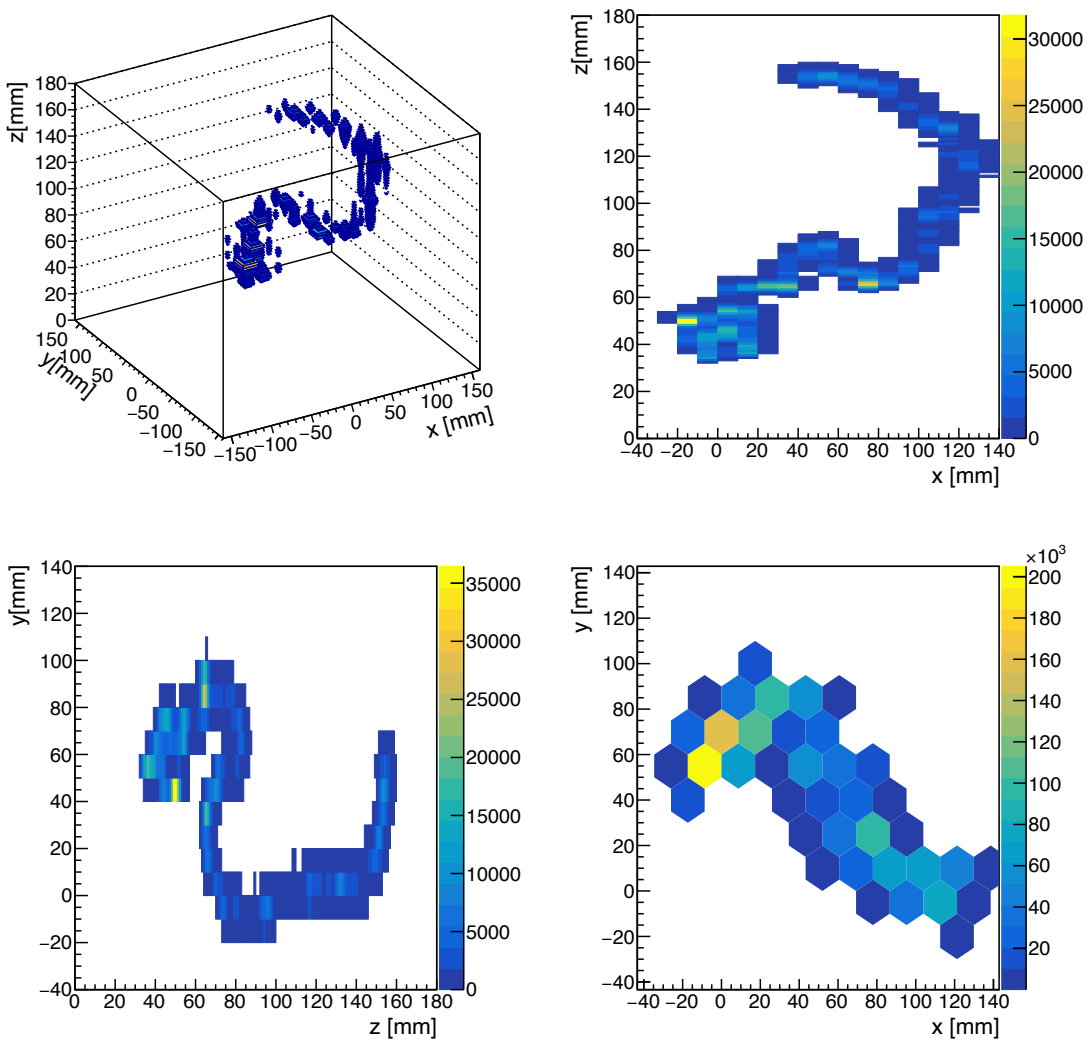

Figure6.5: Reconstructed track image of a 2615 keV event. It is considered to be a photoelectric absorption event.

EL photon generation in ELCC cells for the longitudinal direction. The fit results are $p_0 = (0.1120 \pm 0.0004)\,\mathrm{cm}/\sqrt{\mathrm{cm}}$ for the transverse direction and $p_0 = (0.0264 \pm 0.0002)\,\mathrm{cm}/\sqrt{\mathrm{cm}}$ for the longitudinal direction. The expectations calculated by Magboltz are $0.115\,\mathrm{cm}/\sqrt{\mathrm{cm}}$ for the transverse diffusion and $0.0323\,\mathrm{cm}/\sqrt{\mathrm{cm}}$ for the longitudinal diffusion. The same analysis was performed on the simulation dataset generated with these expected diffusion constants. The simulation takes into account the generation of photons in the ELCC (1 µs) and the response of AxFEB. As shown in Fig. 6.7, the transverse diffusion is roughly reproduced but the longitudinal diffusion differs both for the offset and z dependence. For the longitudinal direction, an additional offset of 1.5 µs is added to the simulation and is also displayed in Fig. 6.7.

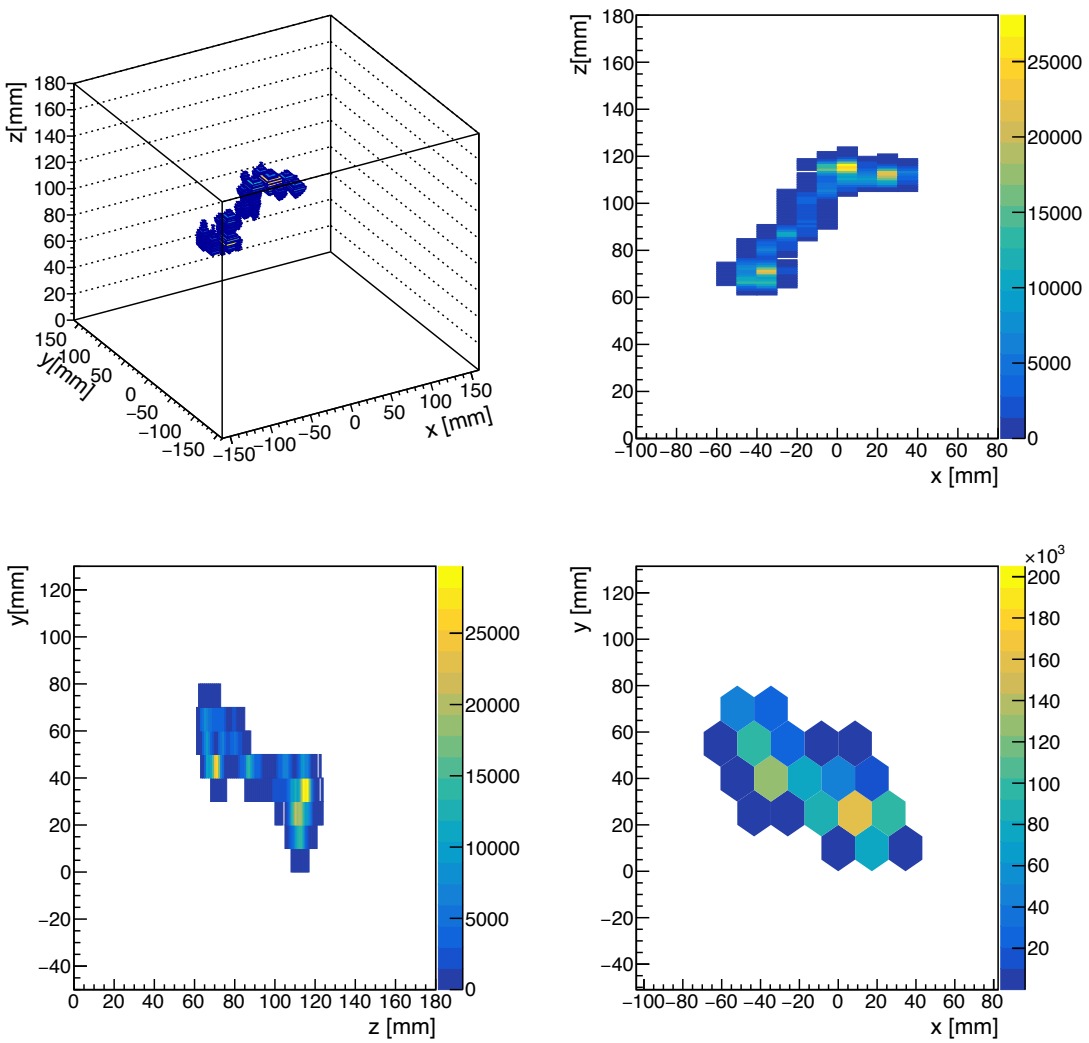

Figure6.6: Reconstructed track image of a 1593 keV event. It is considered to be a double escape event of a pair creation by a 2615 keV gamma ray.

The agreement between the measurement and simulation becomes better. There is, however, still disagreement, indicating that the diffusion constant is different. The diffusion constant is sensitive to the impurities in the gas, and this may be the reason for the disagreement. Since the amount of impurities can easily varies between measurements, it is important to calculate the diffusion constants from the data in this way.

Simulation can be tuned using these data, which is quite important to validate the algorithms separating the $0\nu\beta\beta$ signal from the gamma-ray background based on the track image.

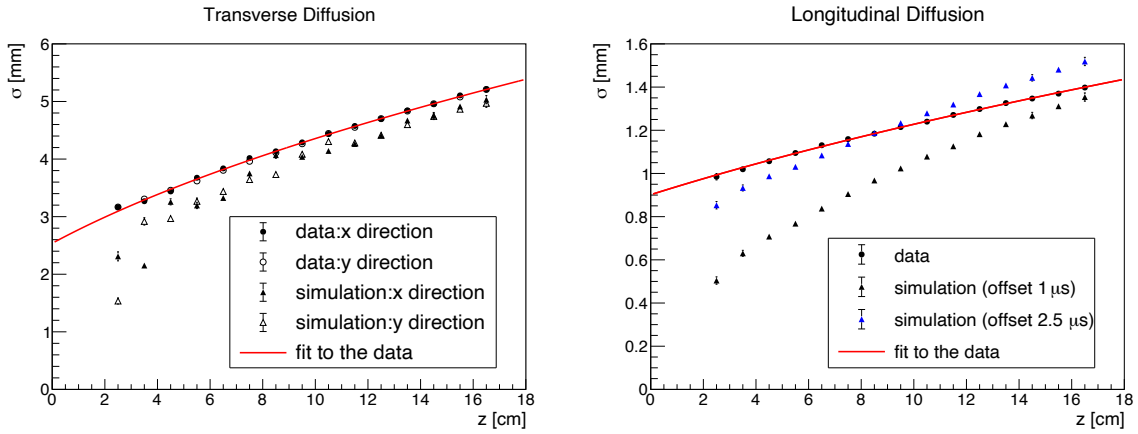

Figure6.7: The standard deviation of the averaged hit distribution of the K_α clusters in the transverse (left panel) and the longitudinal (right panel) direction to the drift direction. The results for the simulation dataset are also shown.

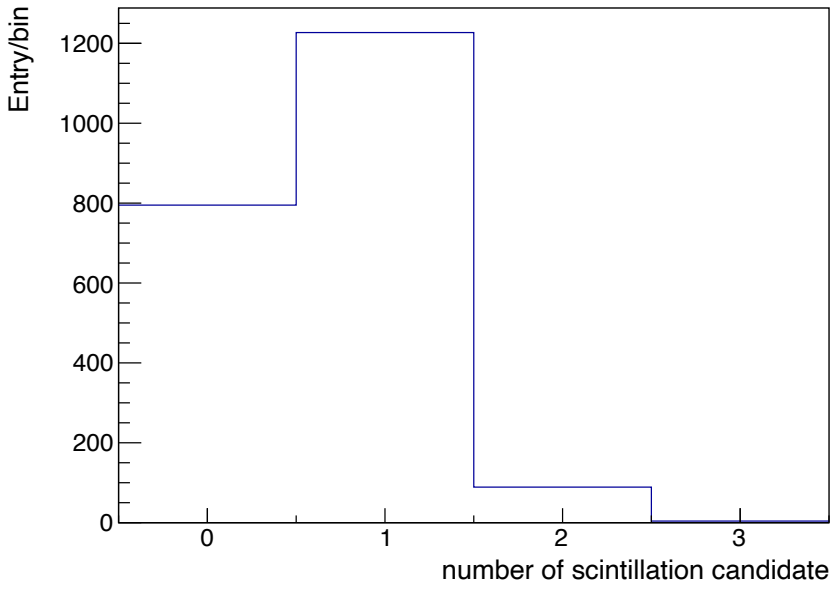

Figure6.8: Number of candidates for the primary scintillation light for 1836 keV events.

6.4 Scintillation detection

Figure 6.8 shows the distribution of the number of hit clusters for the primary scintillation light candidates for 1836 keV events. Assuming the efficiency of detecting the right scintillation light is ε, and the average number of the detected accidental scintillation hits is $\mu_{\rm acc}$, the

probabilities that no or just one hit cluster is detected as a primary scintillation light candidate are as follows.

$$P\left(n_{\mathrm{sci}}=0\right)=\left(1-\varepsilon\right)e^{-\mu_{\mathrm{acc}}} \tag{6.1}$$

$$P\left(n_{\mathrm{sci}}=1\right)=\left(1-\varepsilon\right)\mu_{\mathrm{acc}}e^{-\mu_{\mathrm{acc}}}+\varepsilon e^{-\mu_{\mathrm{acc}}} \tag{6.2}$$

From Fig. 6.8, it follows that $\varepsilon = 0.60$ and $\mu_{\mathrm{acc}} = 0.075$.

Since the average energy to make one scintillation photon is measured to be 72 eV [63], the number of generated scintillation photons for 1836 keV events is 26 000. Considering the average distance to the PMTs is 47 cm, the area of one PMT is 2 cm × 2 cm, the photon detection efficiency of the PMT is 21 %, and the apertures of the meshes are 71 % for the cathode mesh and 67 % for the PMT guard mesh, the total number detected by seven PMTs is ~ 2.6. Thus it is natural that the efficiency for reconstructing the primary scintillation is rather low, $\varepsilon = 0.60$, requiring the coincidence of two or more PMTs. R&D to improve the scintillation detection efficiency for the future detector is ongoing.

7

Discussion

In this chapter, the performance obtained in the previous chapter, especially the energy resolution, is discussed in detail. The expected sensitivity of the future detector for $0\nu\beta\beta$ search is also described.

7.1 Understanding of the energy resolution

In order to achieve better energy resolution, it is required to understand the factors determining the measured energy resolution. Contributions from various sources to the energy resolution were evaluated for the peak of ^{88}Y 1836 keV gamma rays. As the sources, the fluctuation in the signal generation process (Sec. 7.1.1), the errors in the correction process (Sec. 7.1.2), the hardware-origin errors (Sec. 7.1.3), and the mis-reconstruction of the z-position (Sec. 7.1.4) are considered.

For some sources, their effects are estimated based on the simulation. The simulation includes the whole signal generation process. Events are generated by Geant4 [64–66]. The distribution of ionization electrons is calculated from the energy deposit, and the drift of the ionization electrons is simulated considering the diffusion. The number of photons detected at ELCC along the time is calculated based on the simulated response of ELCC (Sec. 2.3.2) to the drifted ionization electrons. For the mean EL gain, the value obtained in the measurement, 12.6, is used. The photon detection along the time is converted to the waveform using the response of the Sallen-Key filter and digitization in the AxFEB. The generated waveforms are analyzed in the same process as the data. In this simulation process, some process is switched off to compare the energy resolution and to evaluate its effect on the energy resolution.

Table 7.1 summarizes the breakdown of the energy resolution at 1836 keV. The details in each source of the energy resolution are described in Secs. 7.1.1 to 7.1.4. The total estimated energy resolution is 0.63 % to 0.67 % while the measured energy resolution is (0.73 ± 0.11) %. They are in agreement within the margin of error.

Table7.1: Breakdown of the energy resolution at 1836 keV listed in descending order.

Error in the time variation correction (Sec. 7.1.2)	0.32 %
Fluctuation of the number of initial ionization electrons (Sec. 7.1.1)	0.29 %
Fluctuation of the EL generation and detection (Sec. 7.1.1)	0.24 %
Error in the EL gain correction (Sec. 7.1.2)	0.23 %
Recombination (Sec. 7.1.1)	0.22 %
Fluctuation of the MPPC non-linearity (Sec. 7.1.1)	0.18 %
z mis-reconstruction (Sec. 7.1.4)	0.13 %
Variation in time bin of time variation correction (Sec. 7.1.2)	$\lesssim$ 0.16 %
Error in the z-dependence correction (Sec. 7.1.2)	$\lesssim$ 0.11 %
Accuracy of the MPPC recovery times (Sec. 7.1.2)	$\lesssim$ 0.11 %
Offset of the baseline (Sec. 7.1.3)	$\lesssim$ 0.09 %
Fluctuation of the attachment (Sec. 7.1.1)	$\lesssim$ 0.02 %
Position dependence of the EL gain (Sec. 7.1.3)	0 %
Waveform filtering in the FEB (Sec. 7.1.3)	0 %
Estimation total	0.63 % to 0.67 %
Data total	(0.73 ± 0.11) %

7.1.1 Fluctuation in the signal generation process

The following five sources are considered in this category; fluctuation of the number of initial ionization electrons, recombination, attachment, fluctuation of the EL generation, and fluctuation of the MPPC non-linearity.

The fluctuation of the number of initial ionization electrons is calculated to be 0.29 % as same as Eq. 1.45, replacing the energy to 1836 keV.

As discussed in Sec. 3.1, the energy resolution deteriorates as the drift electric field is lowered. This is because of the recombination of ionization electrons. As can be read from Fig. 3.1, the energy resolution for 661.7 keV gamma rays is 0.6 % at $\gtrsim$100 V/cm/bar but is worsened to 0.7 % at the electric field at which the measurement was performed (83.3 V/cm/bar). This difference corresponds to 0.22 % at 1836 keV.

The number of ionization electrons is reduced by 0.83 % by attachment during the 180 mm drift with the measured attenuation length of 21 700 mm (Eq. 5.2). Considering the mean photon count at 1836 keV is 1.05×10^6, the fluctuation of this reduction is at most $2.36 \times \sqrt{1.05 \times 10^6 \times 0.83\,\%}/1.05 \times 10^6 = 0.02\,\%$, where 2.36 is the conversion factor from the standard deviation to the FWHM.

The fluctuation of the EL generation and detection was evaluated by a simulation, and was found to be 0.24 %.

As discussed in Sec. 5.1.2, MPPCs suffer from non-linearity when the number of photons simultaneously incident is close to the number of pixels. This is a statistical process so the fluctuation remains even after the non-linearity is corrected. By comparing the simulations with and without this effect, the contribution was estimated to be 0.18 %.

7.1.2 Correction error

Errors in the following four corrections can contribute to the energy resolution; EL gain correction, MPPC recovery times, time variation correction, and z-dependence correction.

The contribution from the error of the EL gain correction (Sec. 5.1.3) is calculated as follows,

$$\frac{\sqrt{\sum_{\mathrm{ch}} \left(\epsilon_{\mathrm{ch}} \bar{N}_{\mathrm{ch}}\right)^2}}{\bar{N}} \times 2.36 \simeq \bar{\epsilon} \sqrt{\frac{\sum_{\mathrm{ch}} \bar{N}_{\mathrm{ch}}^2}{\bar{N}^2}} \times 2.36, \tag{7.1}$$

where ϵ_{ch} is the error for each channel, $\bar{\epsilon}$ is the mean error, $\bar{N}_{\mathrm{ch}}$ is the mean photon count for each channel, and $\bar{N}$ is the mean total photon count at 1836 keV. As the mean of the distribution of the fit errors for the K_α peak of each channel during the EL gain correction, $\bar{\epsilon}$ is derived to be 0.46 %. For every events, $\sum_{\mathrm{ch}} N_{\mathrm{ch}}^2/N^2$ is calculated, and $\sum_{\mathrm{ch}} \bar{N}_{\mathrm{ch}}^2/\bar{N}^2 = 0.043$ is derived as the mean of its distribution. Using these values, the contribution to the energy resolution is 0.23 %. This result is also interpreted as $\bar{\epsilon}/\sqrt{n_{\mathrm{eff}}} \times 2.36$, where n_{eff} is the effective number of the hit channels. Calculated from the result 0.23 %, $n_{\mathrm{eff}} = 22.7$.

The accuracy of the MPPC recovery time measurement affects the energy resolution in two ways: precision of individual MPPC's recovery times and overall bias. The recovery times of individual MPPCs were measured with about 0.5 ns precision. Its effect was estimated by simulation and found to be negligible [50]. The effect of the overall bias is evaluated based on the Eq. 5.3 in Sec. 5.3.5. After the overall fine-tuning of the recovery times, Δk is $(-0.29 \pm 1.84) \times 10^{-6}$, consistent with zero, which is thanks to the fine-tuning. For 1836 keV events, the FWHM of the distribution of CSS is 6.15×10^8, and therefore the contribution to the energy resolution is at most $\sqrt{0.29^2 + 1.84^2} \times 10^{-6} \times 6.15 \times 10^8 / \left(1.05 \times 10^6\right) = 0.11\%$.

The time variation correction factor is determined from the K_α peak fit in each time bin (Sec. 5.3.3). The average fit error is 0.137 %, therefore the error of the scale factor is also 0.137 %, and the contribution to the energy resolution is 0.32 %, multiplied by 2.36.

The variation within the time bin is also evaluated. There is at most 0.24 % variation in the time bin of 30 minutes. Assuming the variation in the time bin is uniform, the contribution to the energy resolution is at most $0.24\% \times \frac{2.36}{\sqrt{12}} = 0.16\%$.

When there is an error in the attenuation length determination, the error from the z-

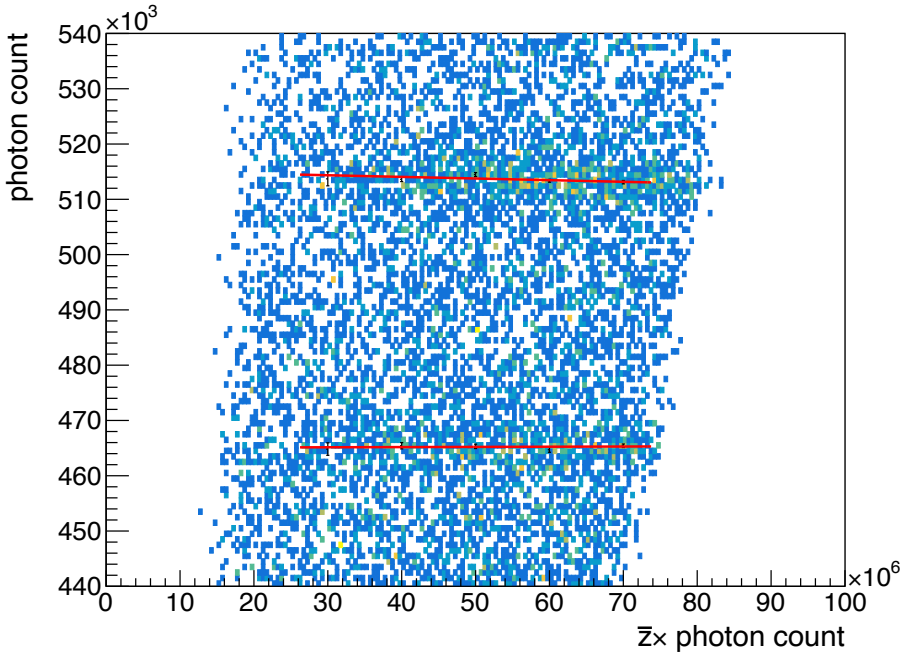

Figure7.1: Relation between the corrected photon counts (N_{cor}) and the product of the photon counts and the mean z-posision ($\bar{z}N_{\mathrm{cor}}$). The clusters at $\sim 5.1 \times 10^5$ photons and $\sim 4.6 \times 10^5$ photons correspond to the photopeak of 898 keV gamma rays and the double escape peak of 1836 keV gamma rays, respectively.

correction (Sec.5.3.4) on the photon counts is calculated as

$$\Delta N_{\mathrm{cor}} = \sum_i p^i N^i_{\mathrm{obs}} \left(1 + \frac{z^i}{\lambda'}\right) - \sum_i p^i N^i_{\mathrm{obs}} \left(1 + \frac{z^i}{\lambda}\right) \tag{7.2}$$

$$\simeq \left(\frac{1}{\lambda'} - \frac{1}{\lambda}\right) \bar{z} N_{\mathrm{cor}} \tag{7.3}$$

where p^i is the correction factor other than the z-dependence correction, z^i is the z-position of each sampling of the waveform, λ' is the attenuation length used in the correction, λ is the true attenuation length, and $\bar{z}$ is the z-position of the event given as the mean weighted by the photon counts. Figure 7.1 shows the distribution of N_{cor} versus $\bar{z}N_{\mathrm{cor}}$. In this distribution, $1/\lambda' - 1/\lambda$ would appear as a slope. From this plot, $1/\lambda' - 1/\lambda$ is obtained as $(-1.52 \pm 1.12) \times 10^{-5}\,\mathrm{mm}^{-1}$, consistent with zero. Because the FWHM of the distribution of $\bar{z}N_{\mathrm{cor}}$ for 1836 keV events is 6.03×10^7 mm, the contribution to the energy resolution is at most $\sqrt{1.52^2 + 1.12^2} \times 10^{-5} \times 6.03 \times 10^7$ photons, that is 0.11 %.

7.1.3 Hardware-origin error

Position dependence of the EL gain and errors arising from the waveform processing in the FEB are considered.

The EL gains depend on the injection positions of ionization electrons relative to the cell as described in Sec. 2.3.2, and the dependence is included in the simulation. The effect on the energy resolution was found to be negligible by comparing the results of simulations with and without this EL gain dependence on the position of ionization electrons.

In the FEBs, the signal waveforms are shaped by the Sallen-Key filters and then digitized. The effect of these filtering and digitization was evaluated by simulation and was found to be negligible.

The baseline of the waveform is unknown within one ADC count. This leads to two effects on the energy reconstruction. First, event-by-event fluctuation of the unknown offset causes fluctuation in the photon count determination. In addition, since the event time width itself fluctuates, the offset affects the photon count determination even if it is constant. The contribution to the energy resolution from the baseline offset is calculated from the mean and standard deviation of the event time width and was found to be 0.09 % at most. The contributions from hardware are small. This is natural because they were so designed.

7.1.4 Mis-reconstruction of z-position

If the primary scintillation is wrongly identified, the z-position of the event is mis-reconstructed and the correction of z-dependence is wrongly applied. From Eq. 6.2, the probability of mis-reconstruction of the z-position is $\frac{(1-\varepsilon)\mu_{\mathrm{acc}}e^{-\mu_{\mathrm{acc}}}}{P(n_{\mathrm{sci}}=1)}$ since only the events with just one hit cluster are chosen in the analysis. Using the values $\varepsilon = 0.60$ and $\mu_{\mathrm{acc}} = 0.075$, this mis-reconstruction probability is calclulated to be 5 %. Assuming the mis-reconstruction distributes uniformly from 0 mm to 180 mm, the mis-correction of z-dependence uniformly distributes from 0 to 0.83 %. Then, the contribution to the energy resolution is $\sqrt{5\%} \times \frac{0.83\%}{\sqrt{12}} \times 2.36 = 0.13\%$.

7.2 Character of multiple-clustered events

The estimation in the previous section was made for the single-clustered track case. As shown in Table 6.1, the energy resolutions for the multiple-clustered events are worse than those of the single-clustered events for most energy peaks. To find the cause of this, we focus on CSS (corrected squared sum).

Even after the fine-tuning of the overall bias of the recovery times of MPPCs (Sec. 5.3.5),

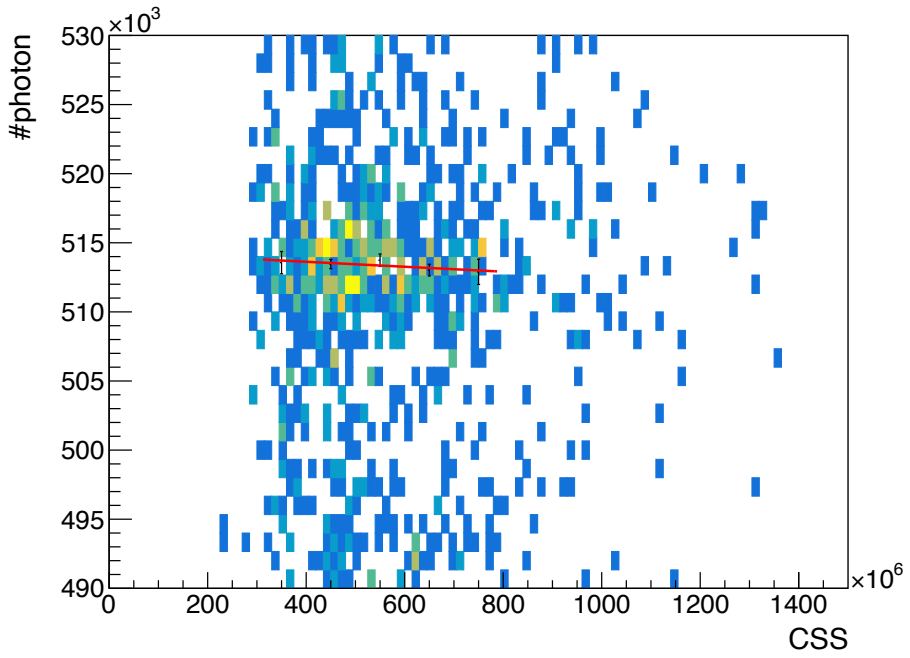

Figure7.2: Relation between the photon counts and the CSS for the multiple-clustered events of 898 keV in the ^{88}Y run after the bias rejection for MPPC recovery times. A slope remains in the distribution, and it corresponds to the recovery time bias of 1.3 ns.

it was found that a bias of 1.3 ns remains for the multiple-clustered events (Fig. 7.2). This indicates that the overall bias differs between the single-clustered events and the multiple-clustered events.

Besides, as shown in Fig. 7.3, CSS of the multiple-clustered events is slightly higher than that of the single-clustered events. High CSS means that the energy deposit is concentrated in a small volume. This is as expected because multiple-clustered events contain more than one track, i.e. multiple stop points. Hence it is possible that the contributions from recombination and fluctuation of the MPPC non-linearity are larger for the multiple-clustered events.

Considering the $0\nu\beta\beta$ search, multiple-clustered background events are rejected by its spatial pattern. Therefore worse energy resolution for the multiple-clustered events is not a problem in the $0\nu\beta\beta$ search in principle. However, $0\nu\beta\beta$ events are expected to have two blobs, and hence their CSS values are expected to be slightly high. Thus, to obtain better energy resolution for the $0\nu\beta\beta$ events, a better understanding of this worse energy resolution for the multiple-clustered events is needed.

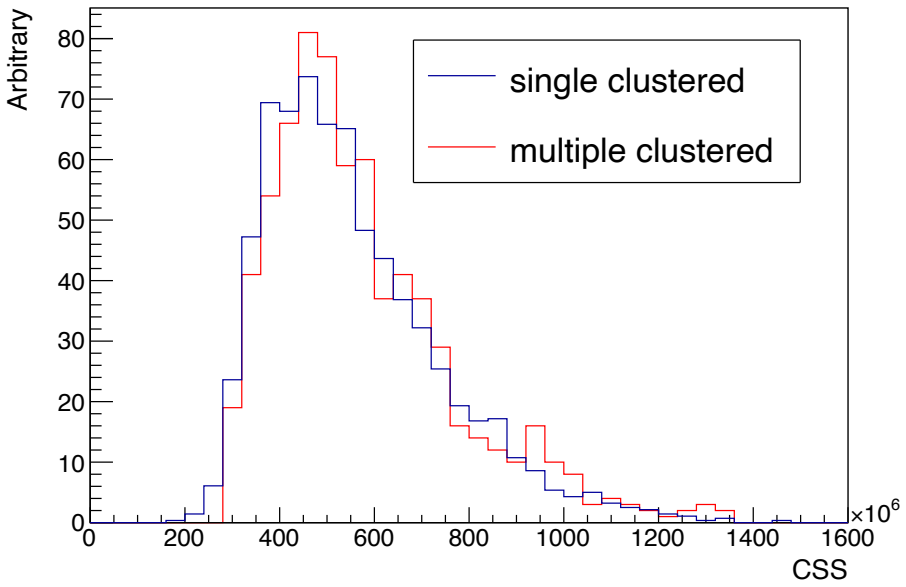

Figure7.3: Distributions of CSS for the single-clustered and the multiple-clustered 898 keV peak. The heights are scaled to match the number of entries.

7.3 Future improvement

In the contributions shown in Table 7.1, the fluctuation of the EL generation and detection can be suppressed by increasing the detected number of photons. To achieve this, we are now developing new ELCC with MPPCs of approximately two times larger sensitive areas and anode electrodes with higher discharge resistance. This improvement increases the number of detected photons by a factor of 2.6, thus reducing the contribution to the energy resolution from 0.24 % to 0.15 %.

The contribution from recombination can be much suppressed by applying a stronger drift electric field, which is now limited by the discharges at ELCC.

The accuracies of the EL gain correction and the time variation correction are limited by the statistics of the K_α peak events and therefore can be reduced to a negligible level by taking more data with a steadier condition.

Mis-reconstruction of z-position comes from the limited efficiency of the primary scintillation detection, which is now 1 p.e. level. We are developing a wavelength-shifting-plate configuration to improve the efficiency of primary scintillation detection and reduce mis-reconstruction using the information of photon counts.

With these countermeasures, the total energy resolution is expected to be improved down

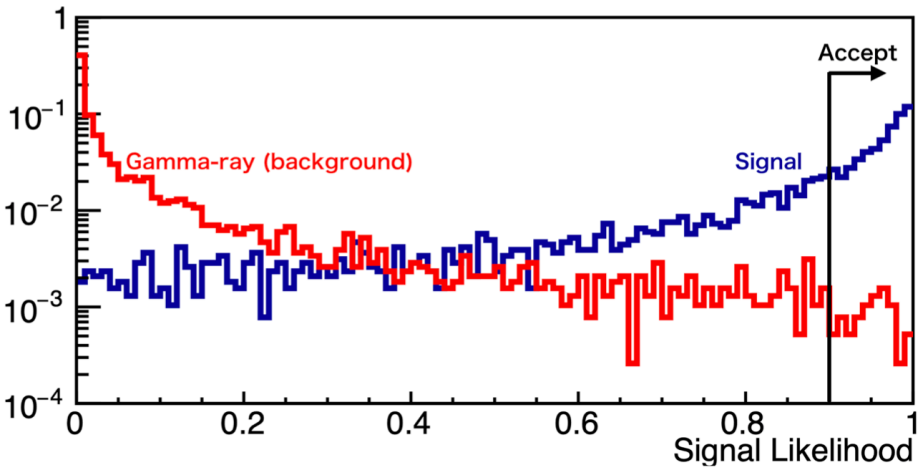

Figure7.4: Signal likelihood output of the neural network. The output is from 0 to 1, and the higher value indicates the more signal-like. The blue line is for the $0\nu\beta\beta$ signals, and the red line is for the ^{214}Bi backgrounds. Figure from [67].

to 0.37% (FWHM) at 1836 keV, which corresponds to 0.32% (FWHM) at the Q value.

7.4 Sensitivity of $0\nu\beta\beta$ search with 1-ton AXEL detector

Assuming the future AXEL detector with 1 ton of pure ^{136}Xe and the main background source of ^{214}Bi in the 10 tons of oxygen-free copper as an inner wall of the vessel, the previous study with three-dimensional convolutional neutral network, a kind of deep learning, applied on the track pattern estimated that the signal efficiency and the background rate are 36.0 % and 3.50 event/year, respectively, when no cut is applied to the energy [67]. Figure 7.4 shows the signal likelihood output of the neural network and the optimal cut threshold. The above background rate and the signal efficiency are based on this result.

Based on these values, the sensitivity for ten years of observation is calculated for the case where the FWHM energy resolution is 0.6 %, extrapolated from the measurement, and 0.32 % as expected in the previous section. A schematic illustration of the energy spectra of $0\nu\beta\beta$ and ^{214}Bi for the FWHM resolution of 0.6 % and 0.32 % case is shown in Fig. 7.5. First, the signal efficiency and the background rate are recalculated based on the assumed energy resolution and the various ranges of the energy selection (region of interest, ROI). Then, a 90 % confidence level upper limit on the number of signals $N^{\rm sig}_{\rm upper}$ is calculated for the null signal case from the background rate following the Feldman-Cousins method [68]. Then, the 90 % confidence level sensitivity is

$$T^{0\nu}_{1/2} = N_{\rm Xe} \times t \times \frac{\varepsilon_{\rm sig}}{N^{\rm sig}_{\rm upper}} \ , \tag{7.4}$$

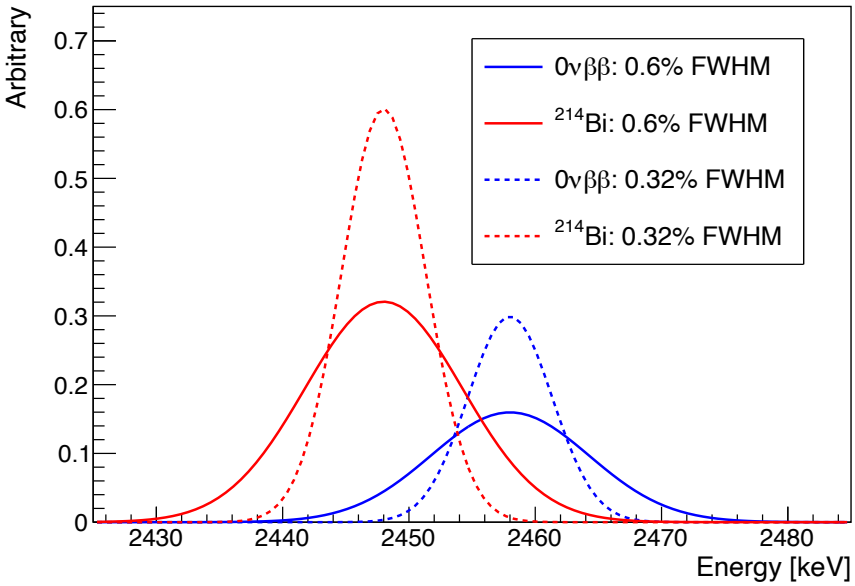

Figure7.5: Expected energy spectra of $0\nu\beta\beta$(blue) and ^{214}Bi (red) for the FWHM energy resolution of 0.6 % (solid) and 0.32 % (dashed) cases. Two times more events is assumed for ^{214}Bi than $0\nu\beta\beta$.

where $N_{\mathrm{Xe}} = 4.43 \times 10^{27}$ is the number of xenon atoms for 1 ton, $t = 10$ years is observation time, and $\varepsilon_{\mathrm{sig}}$ is the signal efficiency.

Figure 7.6 shows the calculated sensitivity. The maximum sensitivity is 1.25×10^{27} years for the ROI of $Q \pm 8$ keV in the case of 0.6 % resolution and 2.53×10^{27} years for the ROI of $Q \pm 4$ keV in the case of 0.32 % resolution. The latter corresponds to 11–47 meV of $m_{\beta\beta}$ assuming the same nuclear matrix element as the result of KamLAND-Zen [31], i.e. calculated values based on energy-density functional theory [69–71], interacting boson model [72, 73], shell model [74–76], and quasiparticle random phase approximation [77–81]. Since the region of inverted ordering neutrino mass is $m_{\beta\beta} \gtrsim 20$ meV, this result demonstrates the impact of the energy resolution of 0.32 %.

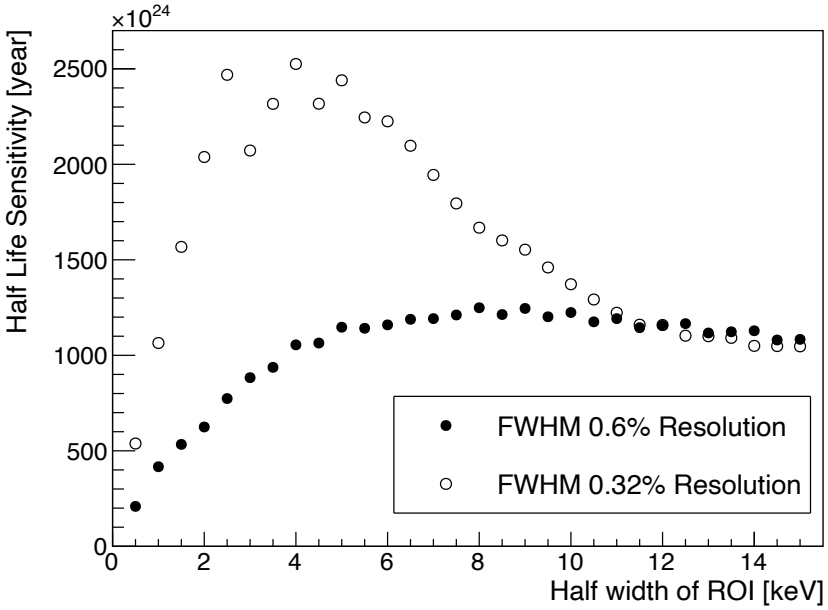

Figure7.6: 90 % confidence level sensitivity in the half-life of $0\nu\beta\beta$ of the AXEL 1 ton detector for 10 years of observation.

8

Conclusion

The discovery of neutrino oscillation revealed the existence of neutrino mass, and it is known to be extremely small from the cosmological observations and the direct mass measurement. In principle, neutrino can have the Majorana mass term, if so, the smallness of neutrino mass may be naturally explained by the See-Saw model. The Majorana nature of neutrino is also a key to understanding the matter-antimatter asymmetry in the universe via the Leptogenesis model. The most plausible way to confirm the Majorana nature of the neutrino is to observe the neutrinoless double-beta decay ($0\nu\beta\beta$). The half-life of 0nbb is inversely proportional to the square of the effective Majorana mass of the electron neutrino ($m_{\beta\beta}$). The current best lower limit on the half-life of ^{136}Xe $0\nu\beta\beta$ is set by the KamLAND-Zen experiment to be $T^{0\nu}_{1/2} > 2.3 \times 10^{26}$ year. This corresponds to the best upper limit on the $m_{\beta\beta}$ of $m_{\beta\beta} <$ (36 – 156) meV. To conduct a sensitive search for such a rare process, a large amount of double-beta decay nuclei, good energy resolution, and background rejection capability are required.

We have been developing a high-pressure xenon gas time projection chamber, AXEL, to search for $0\nu\beta\beta$ of ^{136}Xe. In the AXEL detector, the ionization signal is read out through the electroluminescence process by a pixelized detector, ELCC. The ELCC allows good energy resolution and three-dimensional track reconstruction, which can be used to discriminate background events. The prototype detectors have been developed by increasing the size step by step. The current prototype detector uses a vessel of a 180 L volume. The purpose of the 180 L prototype detector is to establish the performance at the energy around the Q value of ^{136}Xe (2458 keV).

The drift field cage is one of the key components of the AXEL detector. The field cage generates a uniform electric field to drift ionization electrons. The uniformity of the drift electric field affects the energy resolution and the track reconstruction capability. The requirement for the drift field was studied, and it was found that the field intensity higher than 100 V/cm/bar and the uniformity within 5 % have to be realized. The field cage was designed to satisfy this

condition in as large a volume as possible in the 180 L vessel and was constructed. At the first commissioning, electric discharges occurred on the field cage. The paths of the discharges were examined and addressed to prevent discharges, which leads to stable operation.

The measurement for the performance evaluation of the 180 L prototype detector was conducted with two kinds of gamma-ray sources: ^{88}Y (898 keV, 1836 keV) and thorium series radiation (mainly 2615 keV from ^{208}Tl). The data were processed to get better energy resolution, especially eliminating the dispersions and biases of detector responses.

The acquired energy spectrum has a peak at 2615 keV. This is the first observation exceeding the Q value in the history of the AXEL development, though the statistics were limited to evaluate the energy resolution due to a trouble of the gas circulation pump. Other peaks were fitted and the energy resolution was evaluated. The obtained FWHM energy resolution is (0.73 ± 0.11) % at 1836 keV. The FWHM energy resolution at the Q value is estimated to be (0.60 ± 0.03) % when extrapolated by the energy dependence of $a\sqrt{E}$, and (0.70 ± 0.21) % when extrapolated by $a\sqrt{E + bE^2}$. This is the best energy resolution ever among the $0\nu\beta\beta$ search experiments using xenon.

In the reconstructed track images, the dense energy deposits at the end of the track, blobs, were observed, corresponding to the number of electrons in the events. This is a clear feature that can be used to discriminate between the $0\nu\beta\beta$ signal and the gamma-ray backgrounds. The diffusion constants were derived from the data for the first time, which is important for developing algorithms to discriminate the signal and background based on simulated track images.

We investigated possible sources that affect the energy resolution exhaustively and succeeded in fully explaining the measured energy resolution. The result suggests that further development of the ELCC and improvement of the primary scintillation detection can significantly improve the energy resolution to the level of 0.32 % FWHM at the Q value. With this improved energy resolution, the future AXEL detector is expected to achieve a sensitivity of (11 – 47) meV for $m_{\beta\beta}$.

Bibliography

[1] F. Reines, C. L. Cowan, F. B. Harrison, A. D. McGuire, and H. W. Kruse, *Detection of the Free Antineutrino*, Phys. Rev. **117** (Jan, 1960) 159–173.

[2] G. Danby, J. M. Gaillard, K. Goulianos, L. M. Lederman, N. Mistry, M. Schwartz, and J. Steinberger, *Observation of High-Energy Neutrino Reactions and the Existence of Two Kinds of Neutrinos*, Phys. Rev. Lett. **9** (Jul, 1962) 36–44.

[3] K. Kodama et al., *Observation of tau neutrino interactions*, Phys. Lett. B **504** (2001) 218–224.

[4] **ALEPH, DELPHI, L3, OPAL, SLD, LEP Electroweak Working Group, SLD Electroweak Group, SLD Heavy Flavour Group** Collaboration, S. Schael et al., *Precision electroweak measurements on the Z resonance*, Phys. Rept. **427** (2006) 257–454, arXiv:hep-ex/0509008.

[5] **Super-Kamiokande** Collaboration, Y. Fukuda et al., *Evidence for Oscillation of Atmospheric Neutrinos*, Phys. Rev. Lett. **81** (Aug, 1998) 1562–1567.

[6] I. Esteban, M. C. Gonzalez-Garcia, M. Maltoni, T. Schwetz, and A. Zhou, *The fate of hints: updated global analysis of three-flavor neutrino oscillations*, JHEP **09** (2020) 178, arXiv:2007.14792 [hep-ph].

[7] *NuFIT 5.2*, 2022. www.nu-fit.org.

[8] **Super-Kamiokande** Collaboration, K. Abe et al., *Atmospheric neutrino oscillation analysis with external constraints in Super-Kamiokande I-IV*, Phys. Rev. D **97** (2018) 072001, arXiv:1710.09126 [hep-ex].

[9] **T2K** Collaboration, K. Abe et al., *Measurements of neutrino oscillation parameters from the T2K experiment using* 3.6×10^{21} *protons on target*, Eur. Phys. J. C **83** (2023) 782, arXiv:2303.03222 [hep-ex].

[10] **Hyper-Kamiokande** Collaboration, K. Abe et al., *Hyper-Kamiokande Design Report*, arXiv:1805.04163 [physics.ins-det].

[11] **JUNO** Collaboration, A. Abusleme et al., *JUNO physics and detector*, Prog. Part. Nucl. Phys. **123** (2022) 103927, arXiv:2104.02565 [hep-ex].

[12] **Planck** Collaboration, N. Aghanim et al., *Planck 2018 results. VI. Cosmological*

parameters, Astron. Astrophys. **641** (2020) A6, arXiv:1807.06209 [astro-ph.CO]. [Erratum: Astron.Astrophys. 652, C4 (2021)].

[13] S. Brieden, H. Gil-Marín, and L. Verde, *Model-agnostic interpretation of 10 billion years of cosmic evolution traced by BOSS and eBOSS data*, JCAP **08** (2022) 024, arXiv:2204.11868 [astro-ph.CO].

[14] P. Ade et al., *The simons observatory: science goals and forecasts*, JCAP **2019** (Feb, 2019) 056.

[15] **KATRIN** Collaboration, M. Aker et al., *Direct neutrino-mass measurement with sub-electronvolt sensitivity*, Nature Phys. **18** (2022) 160–166, arXiv:2105.08533 [hep-ex].

[16] M. Fukugita and T. Yanagida, *Barygenesis without grand unification*, Phys. Lett. B **174** (1986) 45–47.

[17] R. N. Mohapatra et al., *Theory of neutrinos: a white paper*, Rept. Prog. Phys. **70** (Oct, 2007) 1757.

[18] S. Chu, L. Ekstroem, and R. Firestone, *Lund/LBNL Nuclear Data Search*, 2023. http://nucleardata.nuclear.lu.se/toi/.

[19] B. Pritychenko, *Systematic analysis of double-beta decay half lives*, Nucl. Phys. A **1033** (2023) 122628, arXiv:2303.00838 [nucl-th].

[20] **NEMO-3** Collaboration, R. Arnold et al., *Measurement of the double-beta decay half-life and search for the neutrinoless double-beta decay of ^{48}Ca with the NEMO-3 detector*, Phys. Rev. D **93** (2016) 112008, arXiv:1604.01710 [hep-ex].

[21] M. Agostini et al., *Results on $\beta\beta$ decay with emission of two neutrinos or Majorons in ^{76}Ge from GERDA Phase I*, Eur. Phys. J. C **75** (2015) 416, arXiv:1501.02345 [nucl-ex].

[22] R. Arnold et al., *Final results on ^{82}Se double beta decay to the ground state of ^{82}Kr from the NEMO-3 experiment*, Eur. Phys. J. C **78** (2018) 821, arXiv:1806.05553 [hep-ex].

[23] **NEMO-3** Collaboration, J. Argyriades et al., *Measurement of the two neutrino double beta decay half-life of Zr-96 with the NEMO-3 detector*, Nucl. Phys. A **847** (2010) 168–179, arXiv:0906.2694 [nucl-ex].

[24] E. Armengaud et al., *Development of ^{100}Mo-containing scintillating bolometers for a high-sensitivity neutrinoless double-beta decay search*, Eur. Phys. J. C **77** (2017) 785, arXiv:1704.01758 [physics.ins-det].

[25] **NEMO-3** Collaboration, R. Arnold et al., *Measurement of the $2\nu\beta\beta$ Decay Half-Life and Search for the $0\nu\beta\beta$ Decay of ^{116}Cd with the NEMO-3 Detector*, Phys. Rev. D **95** (2017) 012007, arXiv:1610.03226 [hep-ex].

[26] **CUORE** Collaboration, D. Q. Adams et al., *Measurement of the $2\nu\beta\beta$ Decay Half-Life of ^{130}Te with CUORE*, Phys. Rev. Lett. **126** (2021) 171801, arXiv:2012.11749 [nucl-ex].

[27] **KamLAND-Zen** Collaboration, A. Gando et al., *Measurement of the double-β decay*

half-life of ^{136}Xe *with the KamLAND-Zen experiment*, Phys. Rev. C **85** (2012) 045504, arXiv:1201.4664 [hep-ex].

[28] **NEMO-3** Collaboration, R. Arnold et al., *Measurement of the* $2\nu\beta\beta$ *decay half-life of* ^{150}Nd *and a search for* $0\nu\beta\beta$ *decay processes with the full exposure from the NEMO-3 detector*, Phys. Rev. D **94** (2016) 072003, arXiv:1606.08494 [hep-ex].

[29] F. T. Avignone, III, S. R. Elliott, and J. Engel, *Double Beta Decay, Majorana Neutrinos, and Neutrino Mass*, Rev. Mod. Phys. **80** (2008) 481–516, arXiv:0708.1033 [nucl-ex].

[30] J. Engel and J. Menéndez, *Status and Future of Nuclear Matrix Elements for Neutrinoless Double-Beta Decay: A Review*, Rept. Prog. Phys. **80** (2017) 046301, arXiv:1610.06548 [nucl-th].

[31] **KamLAND-Zen** Collaboration, S. Abe et al., *Search for the Majorana Nature of Neutrinos in the Inverted Mass Ordering Region with KamLAND-Zen*, Phys. Rev. Lett. **130** (Jan, 2023) 051801.

[32] M. Berger, J. Hubbell, S. Seltzer, J. Chang, J. Coursey, R. Sukumar, D. Zucker, and K. Olsen, *XCOM: Photon Cross Section Database (version 1.5)*, 2010. http://physics.nist.gov/xcom.

[33] R. Deslattes et al., *X-ray Transition Energies (version 1.2)*, 2005. http://physics.nist.gov/XrayTrans.

[34] S. R. Elliott and P. Vogel, *DOUBLE BETA DECAY*, Ann. Rev. Nucl. Part. Sci. **52** (2002) 115–151, https://doi.org/10.1146/annurev.nucl.52.050102.090641.

[35] **KamLAND-Zen** Collaboration, A. Gando et al., *Search for Majorana Neutrinos near the Inverted Mass Hierarchy Region with KamLAND-Zen*, Phys. Rev. Lett. **117** (2016) 082503, arXiv:1605.02889 [hep-ex]. [Addendum: Phys.Rev.Lett. 117, 109903 (2016)].

[36] **GERDA** Collaboration, M. Agostini et al., *Final Results of GERDA on the Search for Neutrinoless Double-*β *Decay*, Phys. Rev. Lett. **125** (2020) 252502, arXiv:2009.06079 [nucl-ex].

[37] H. A. Koehler, L. J. Ferderber, D. L. Redhead, and P. J. Ebert, *Vacuum-ultraviolet emission from high-pressure xenon and argon excited by high-current relativistic electron beams*, Phys. Rev. A **9** (Feb, 1974) 768–781.

[38] S. P. Ahlen, *Theoretical and experimental aspects of the energy loss of relativistic heavily ionizing particles*, Rev. Mod. Phys. **52** (Jan, 1980) 121–173.

[39] D. Anderson, T. Hamilton, W. Ku, and R. Novick, *A large area, gas scintillation proportional counter*, Nucl. Instrum. Meth. **163** (1979) 125–134.

[40] **NEXT** Collaboration, J. Renner et al., *Energy calibration of the NEXT-White detector with 1% resolution near* $Q_{\beta\beta}$ *of* ^{136}Xe, JHEP **10** (2019) 230, arXiv:1905.13110 [physics.ins-det].

[41] **NEXT** Collaboration, M. Kekic et al., *Demonstration of background rejection using*

deep convolutional neural networks in the NEXT experiment, JHEP **01** (2021) 189, arXiv:2009.10783 [physics.ins-det].

[42] **NEXT** Collaboration, C. Adams et al., *Sensitivity of a tonne-scale NEXT detector for neutrinoless double beta decay searches*, JHEP **2021** (2021) 164, arXiv: 2005.06467 [physics.ins-det].

[43] **PandaX-III** Collaboration, W. Zhang, H. Lin, Y. Liu, K. Han, K. Ni, S. Wang, and W. Zhai, *Status and prospects of the PandaX-III experiment*, JINST **18** (2023) C12001, arXiv:2311.13396 [physics.ins-det].

[44] **PandaX-III** Collaboration, H. Lin, *Latest progress of PandaX-III neutrinoless double beta decay experiment*, J. Phys. Conf. Ser. **2502** (2023) 012007.

[45] T. Li, S. Wang, Y. Chen, K. Han, H. Lin, K. Ni, W. Wang, Y. Xu, and A. Zou, *Signal identification with Kalman Filter towards background-free neutrinoless double beta decay searches in gaseous detectors*, JHEP **06** (2021) 106, arXiv: 2102.08221 [physics.ins-det].

[46] M. Malinen and P. Raback, Multiscale Modelling Methods for Applications in Material Science, ch. Elmer finite element solver for multiphysics and multiscale problems. Forschungszentrum Juelich, 2013.

[47] S. Ban, Development of a high pressure xenon gas time projection chamber with a unique cellular readout structure to search for neutrinoless double beta decay. PhD thesis, Kyoto University, 2020.

[48] S. Ban et al., *Electroluminescence collection cell as a readout for a high energy resolution Xenon gas TPC*, Nucl. Instrum. Meth. A **875** (2017) 185 – 192.

[49] S. Ban et al., *Design and performance of a high-pressure xenon gas TPC as a prototype for a large-scale neutrinoless double-beta decay search*, PTEP **2020** (2020) . 033H01.

[50] K. Nakamura, Development of a large-sized high-pressure xenon gas time projection chamber for neutrinoless double beta decay search. PhD thesis, Kyoto University, 2022.

[51] *Technical note of MPPC*, 2023. https://www.hamamatsu.com/content/dam/hamamatsu-photonics/sites/documents/99_SALES_LIBRARY/ssd/mppc_kapd9008e.pdf.

[52] S. Yanagita Master's thesis, Kyoto University, 2015. in Japanese.

[53] K. Z. Nakamura, S. Ban, A. K. Ichikawa, M. Ikeno, K. D. Nakamura, T. Nakaya, S. Obara, S. Tanaka, T. Uchida, and M. Yoshida, *Front-End Electronics for the SiPM-Readout Gaseous TPC for Neutrinoless Double-Beta Decay Search*, IEEE Trans. Nucl. Sci. **67** (2020) 1772–1776.

[54] R. Honda, K. Miwa, K. Hosomi, M. Ikeno, and T. Uchida, *Development of the general purpose logic module, hadron universal logic module, for the j-parc hadron*

experiments., Meeting Abstracts of the Physical Society of Japan **71.2** (2016) 223–223.

[55] **NEXT** Collaboration, L. Serra et al., *An improved measurement of electron-ion recombination in high-pressure xenon gas*, JINST **10** (2015) P03025, arXiv: 1412.3573 [physics.ins-det].

[56] A. Bolotnikov and B. Ramsey, *The spectroscopic properties of high-pressure xenon*, Nucl. Instrum. Meth. A **396** (1997) 360–370.

[57] S. Biagi, *Magboltz - transport of electrons in gas mixtures*, 1995. http://magboltz.web.cern.ch/magboltz.

[58] L. C. Pitchford et al., *LXCat: an Open-Access, Web-Based Platform for Data Needed for Modeling Low Temperature Plasmas*, Plasma Process. Polym. **14** (2016) 1600098.

[59] D. C. Meeker, *Finite element method magnetics, version 4.2*, 2018. https://www.femm.info/wiki/HomePage.

[60] **ZEPLIN-III** Collaboration, E. Santos et al., *Single electron emission in two-phase xenon with application to the detection of coherent neutrino-nucleus scattering*, JHEP **12** (2011) 115, arXiv:1110.3056 [physics.ins-det].

[61] E. Aprile et al., *Observation and applications of single-electron charge signals in the XENON100 experiment*, J. Phys. G **41** (Feb, 2014) 035201.

[62] P. Sorensen and K. Kamdin, *Two distinct components of the delayed single electron noise in liquid xenon emission detectors*, JINST **13** (Feb, 2018) P02032.

[63] L. M. P. Fernandes, E. D. C. Freitas, M. Ball, J. J. Gomez-Cadenas, C. M. B. Monteiro, N. Yahlali, D. Nygren, and J. M. F. d. Santos, *Primary and secondary scintillation measurements in a xenon Gas Proportional Scintillation Counter*, JINST **5** (2010) P09006, arXiv:1009.2719 [astro-ph.IM]. [Erratum: JINST 5, A12001 (2010)].

[64] S. Agostinelli et al., *Geant4—a simulation toolkit*, Nucl. Instrum. Meth. A **506** (2003) 250 – 303.

[65] J. Allison et al., *Geant4 developments and applications*, IEEE Trans. Nucl. Sci. **53** (2006) 270–278.

[66] J. Allison et al., *Recent developments in Geant4*, Nucl. Instrum. Meth. A **835** (2016) 186–225.

[67] S. Tanaka, 2019. private communication.

[68] G. J. Feldman and R. D. Cousins, *Unified approach to the classical statistical analysis of small signals*, Phys. Rev. D **57** (Apr, 1998) 3873–3889.

[69] N. López Vaquero, T. R. Rodríguez, and J. L. Egido, *Shape and pairing fluctuations effects on neutrinoless double beta decay nuclear matrix elements*, Phys. Rev. Lett. **111** (2013) 142501, arXiv:1401.0650 [nucl-th].

[70] J. M. Yao, L. S. Song, K. Hagino, P. Ring, and J. Meng, *Systematic study of nuclear matrix elements in neutrinoless double-β decay with a beyond-mean-field covariant*

density functional theory, Phys. Rev. C **91** (2015) 024316, arXiv:1410.6326 [nucl-th].

[71] T. R. Rodriguez and G. Martinez-Pinedo, *Energy density functional study of nuclear matrix elements for neutrinoless $\beta\beta$ decay*, Phys. Rev. Lett. **105** (2010) 252503, arXiv:1008.5260 [nucl-th].

[72] F. F. Deppisch, L. Graf, F. Iachello, and J. Kotila, *Analysis of light neutrino exchange and short-range mechanisms in $0\nu\beta\beta$ decay*, Phys. Rev. D **102** (2020) 095016, arXiv:2009.10119 [hep-ph].

[73] J. Barea, J. Kotila, and F. Iachello, *$0\nu\beta\beta$ and $2\nu\beta\beta$ nuclear matrix elements in the interacting boson model with isospin restoration*, Phys. Rev. C **91** (2015) 034304, arXiv:1506.08530 [nucl-th].

[74] L. Coraggio, A. Gargano, N. Itaco, R. Mancino, and F. Nowacki, *Calculation of the neutrinoless double-β decay matrix element within the realistic shell model*, Phys. Rev. C **101** (2020) 044315, arXiv:2001.00890 [nucl-th].

[75] A. Neacsu and M. Horoi, *Shell model studies of the ^{130}Te neutrinoless double-beta decay*, Phys. Rev. C **91** (2015) 024309, arXiv:1411.4313 [nucl-th].

[76] J. Menendez, A. Poves, E. Caurier, and F. Nowacki, *Disassembling the Nuclear Matrix Elements of the Neutrinoless beta beta Decay*, Nucl. Phys. A **818** (2009) 139–151, arXiv:0801.3760 [nucl-th].

[77] J. Terasaki, *Strength of the isoscalar pairing interaction determined by a relation between double-charge change and double-pair transfer for double- β decay*, Phys. Rev. C **102** (2020) 044303, arXiv:2003.03542 [nucl-th].

[78] J. Hyvärinen and J. Suhonen, *Nuclear matrix elements for $0\nu\beta\beta$ decays with light or heavy Majorana-neutrino exchange*, Phys. Rev. C **91** (2015) 024613.

[79] F. Šimkovic, V. Rodin, A. Faessler, and P. Vogel, *$0\nu\beta\beta$ and $2\nu\beta\beta$ nuclear matrix elements, quasiparticle random-phase approximation, and isospin symmetry restoration*, Phys. Rev. C **87** (2013) 045501, arXiv:1302.1509 [nucl-th].

[80] M. T. Mustonen and J. Engel, *Large-scale calculations of the double-β decay of ^{76}Ge, ^{130}Te, ^{136}Xe, and ^{150}Nd in the deformed self-consistent Skyrme quasiparticle random-phase approximation*, Phys. Rev. C **87** (2013) 064302, arXiv:1301.6997 [nucl-th].

[81] D.-L. Fang, A. Faessler, and F. Simkovic, *$0\nu\beta\beta$ -decay nuclear matrix element for light and heavy neutrino mass mechanisms from deformed quasiparticle random-phase approximation calculations for ^{76}Ge, ^{82}Se, ^{130}Te, ^{136}Xe , and ^{150}Nd with isospin restoration*, Phys. Rev. C **97** (2018) 045503, arXiv:1803.09195 [nucl-th].